Pattern formation under the influence of confinement and conservation

Von der Universität Bayreuth
zur Erlangung des Grades eines
Doktors der Naturwissenschaften (Dr. rer. nat.)
genehmigte Abhandlung

von

Fabian Bergmann

aus Wasserlos

1. Gutachter: Prof. Dr. Walter Zimmermann
2. Gutachter: Prof. Dr. Markus Bär

Tag der Einreichung: 09. April 2019
Tag des Kolloquiums: 09. August 2019

Abstract

This thesis consists of two parts dealing with different so far unsolved problems in the field of pattern formation theory. The first part studies the effects of restricting pattern formation to a finite domain – a scenario that is omnipresent in nature. In the second part we identify and investigate a new phase separation phenomenon in active systems with a conservation law – the so-called active phase separation.

In a first publication we show that physical boundaries generically lead to a reflection effect for nonlinear traveling waves. This reflection forces systems that show traveling waves in large extended systems into a standing wave pattern if the system becomes sufficiently short. We also identify bands of stable standing waves with different numbers of nodes, allowing for transitions between different standing wave patterns. This generic result is especially relevant for the Min protein system that plays a crucial role in the cell division process of the bacterium *E. coli*. Thereby the Min proteins show a traveling wave pattern on large extended membranes in *in vitro* experiments, while inside a cell a standing wave-like pattern is observed.

Finite domains for patterns can also be generated without hard physical boundaries. Instead the control parameter that switches the system between a patterned state and a homogeneous state can be varied spatially in a way that it suppresses the pattern in one region and allows it in another. A possible experimental realization for this scenario are light-sensitive chemical reactions where the pattern formation process can be enhanced or inhibited using an illumination mask. We figure out that the steepness of the variation from a sub- to a supercritical control parameter influences the orientation of stripe patterns in two spatial dimensions. For steep step-like control parameter drops, the stripes favor a orientation parallel to the control parameter variation. For smooth ramp-like drops on the other hand, they favor a perpendicular orientation. This also implies that the orientation of stripes will switch from parallel to perpendicular when decreasing the steepness of the drop. This transition can be understood with the decreasing importance of local resonance effects induced by the control parameter drop.

In another way, a control parameter drop also influences traveling wave pattern in one dimension. While again local resonance effects are important, the control parameter drop there leads to four different wave patterns depending on the group velocity. For small group velocities, the traveling wave pattern thereby fills the whole supercritical domain forming a filled state. Increasing the group velocity

will confine the pattern to one side of the supercritical domain. Even higher group velocities induce a state with a time-dependent amplitude of the wave pattern – a so-called blinking state. Thereby both left- and right-traveling waves occur whose amplitudes change periodically in time. Increasing the group velocity further leads to a return of a wave state with a stationary amplitude. In the counter-propagating wave state we find a left-moving wave in the left half of the supercritical domain and a right-moving wave in the right half.

The second part of this thesis attends to a phenomenon resembling phase separation or demixing in several systems with a conserved quantity. Among them are the assembly of proteins in different halves of a polarized cell, the aggregation of cell colonies that communicate chemotactically or clustering behavior of active Brownian particles. Even if these different systems constantly consume energy locally – rendering them non-equilibrium systems– all of them show a transition from a homogenous to a state with a dense and a dilute phase similar to classical phase separation. We are able to show that this similarity is indeed not coincidental. Instead, models of systems from very different fields can be mapped onto one universal equation close to the onset of the phase separation process. This equation turns out to be the Cahn-Hilliard equation – an equation that is usually used to describe phase separation in thermal equilibrium. We demonstrate that this equation is also the universal description of what we call active phase separation. In our publications we introduce a new kind of weakly nonlinear analysis that allows to directly link the parameters of the original system to those of the Cahn-Hilliard equation. This allows to confirm the validity of our approach by comparing numerical simulations of the different original systems to the corresponding Cahn-Hilliard model. We thereby find a convincing agreement in both stationary profiles, as well as the dynamical evolution of the two. We furthermore extend the weakly nonlinear analysis to the next higher order, which is especially interesting for active Brownian systems showing so-called motility-induced phase separation. In those systems the significance of higher order contributions is highly discussed. We are again able to directly map the original system to an extended Cahn-Hilliard model, which allows to identify straightforward the relevant contributions for a given model.

Kurzdarstellung

Die vorliegende Dissertation besteht aus zwei Teilen, die bisher ungelöste Fragestellungen aus dem Gebiet der Strukturbildung behandeln. Der erste Teil widmet sich dem Einfluss von Beschränkungen der Muster auf ein endliches Gebiet – ein Szenario das in der Natur allgegenwärtig ist. Im zweiten Teil identifizieren und untersuchen wir eine neue Art der Phasentrennung in aktiven Systemen mit Erhaltung – sogenannte aktive Phasentrennung.

In einer ersten Publikation gelang es uns zu zeigen, dass physikalische Ränder generisch zu einer Reflexion nichtlinearer Wanderwellen führen. Die Reflexion zwingt Systeme, die in räumlich ausgedehnten Systemen Wanderwellen bilden, zu stehenden Wellen, wenn die Systemlänge kurz genug wird. Wir identifizieren außerdem Bänder stabiler Wanderwellen mit unterschiedlich vielen Knoten, was auch Übergänge zwischen verschiedenen Arten stehender Wellen ermöglicht. Dieses allgemeine Ergebnis ist insbesondere für das sogenannte Min-Protein System relevant, welches eine entscheidende Rolle im Zellteilungsprozess des Bakteriums *E. Coli* spielt. Die Min-Proteine formen dabei in *in vitro* Experimenten Wanderwellen auf ausgedehnten Membranen, während ihre Muster innerhalb der Zelle einer stehenden Welle ähneln.

Eine Begrenzung der Muster auf einen endlichen Bereich kann auch ohne harte physikalische Ränder erreicht werden. Stattdessen kann der Kontrollparameter, welcher zwischen einem musterbildenden und einem homogenen Zustand umschaltet, räumlich so variiert werden, dass er in einem Gebiet Musterbildung unterdrückt und in einem anderen ermöglicht. Experimentell lässt sich dieses Szenario zum Beispiel in lichtsensitiven chemischen Reaktionen realisieren, bei der die Musterbildung mit Hilfe einer Beleuchtungsmaske gesteuert werden kann. Wir zeigen, dass die Steilheit der Kontrollparameteränderung vom sub- in den superkritischen Bereich entscheidenden Einfluss auf die Orientierung von Streifen in zwei Raumdimensionen hat. Im Falle eines steilen stufenartigen Übergangs werden parallel zur Kontrollparameteränderung orientierte Streifen bevorzugt. Flache rampenartige Kontrollparametervariationen andererseits führen zu einer senkrechten Orientierung. Dieser Übergang zwischen verschiedenen Streifenorientierungen hat seinen Ursprung in der abnehmenden Bedeutung lokaler Resonanzeffekte, die der Kontrollparametervariation entspringen.

Auf andere Weise beeinflusst eine solche Kontrollparametervariation auch Wanderwellen in einer Raumdimension. Während wiederum lokale Resonanzeffekte wichtig sind, führt die Kontrollparametervariation dort zu vier verschiedene Arten von Wellenmustern, abhängig von der Gruppengeschwindigkeit. Im Fall kleiner Gruppengeschwindigkeiten füllen die Wanderwellen den gesamten superkritischen Bereich (filled state). Eine höhere Gruppengeschwindigkeit verschiebt den Bereich mit einem Wellenmuster zu einer Seite des superkritischen Bereichs. Noch höhere Gruppengeschwindigkeiten führen zu einem Wellenmuster, dessen Amplitude zeitabhängig wird – einem sogenannten blinking state. Dabei bilden sich rechts- und linkslaufende Wellen, deren Amplitude sich zeitlich periodisch ändert. Eine weitere Erhöhung der Gruppengeschwindigkeit führt zu einer Rückkehr von Wellen mit stationärer Amplitude. In diesem „counterpropagating wave state“ findet man eine links laufende Welle in der linken Hälfte des superkritischen Bereichs und eine rechts laufende Welle in der rechten Hälfte.

Der zweite Teil dieser Arbeit widmet sich einem Phasentrennungsphänomen, das in verschiedenen Systemen mit einer erhaltenen Größe auftritt. Zu diesen zählen unter anderem Zellpolarisation, bei der sich Proteine in verschiedenen Hälften der Zelle sammeln, die Agglomeration chemotaktisch kommunizierender Zellen oder das Clustern aktiver brownscher Teilchen. Selbst wenn diese unterschiedlichen Systeme fortwährend lokal Energie verbrauchen – was sie klar zu Nichtgleichgewichtssystemen macht – zeigen alle einen Übergang von einem homogenen Zustand zu einem Zustand mit einer dichteren und einer weniger dichten Phase ähnlich zu klassischer Entmischung. Wir zeigen, dass diese Ähnlichkeit in der Tat kein Zufall ist. Stattdessen können unterschiedlichste Modellsysteme nahe des Einsatzpunkts der Phasenseparation auf eine universelle Gleichung reduziert werden. Diese ist überraschenderweise die Cahn-Hilliard Gleichung – eine Gleichung die üblicherweise zur Beschreibung von Entmischung im thermischen Gleichgewicht verwendet wird. Wir zeigen nun, dass diese Gleichung ebenso die universelle Beschreibung aktiver Phasentrennung darstellt.

In unseren Publikationen führen wir eine neue Art der schwach nichtlinearen Analyse ein, die eine direkte Verbindung zwischen Parametern des ursprünglichen Systems zu denen der Cahn-Hilliard Gleichung ermöglicht. Dies erlaubt die Gültigkeit und den Geltungsbereich unseres Ansatzes durch einen direkten Vergleich numerischer Simulationen des Originalsystems und der zugehörigen Cahn-Hilliard Gleichung zu bestimmen. Wir beobachten dabei eine überzeugende Übereinstimmung sowohl bei stationären Profilen, als auch in der zeitlichen Entwicklung.

Außerdem erweitern wir die schwach nichtlineare Analyse zur nächsthöheren Ordnung, was besonders für aktive brownsche Teilchen relevant ist, die sogenannte beweglichkeitsinduzierte Phasentrennung zeigen. In diesen Systemen wird die

Bedeutung solcher Beiträge höherer Ordnung in der Literatur intensiv diskutiert. Wir sind nun erstmals in der Lage, das Ausgangssystem auf eine erweiterte Cahn-Hilliard Gleichung abzubilden. Dies ermöglicht es, direkt zu erkennen, welche dieser Beiträge für eine gegebenes System relevant sind.

Contents

Abstract I

Kurzdarstellung III

1 Extended Abstract 1

1.1 Introduction 1
1.2 Part I: Patterns in finite systems 2
1.3 Part II: Active phase separation 20
1.4 Bibliography 33

2 Publications 47

2.1 List of included publications 47
2.2 Individual contributions of the authors 48
2.3 List of talks and posters 49
2.4 Attached publications: 51
Size matters for nonlinear (protein) wave patterns 51
Pattern orientation in finite domains without boundaries 63
Reflection of nonlinear wave patterns in finite domains without boundaries 71
Active phase separation: A universal approach 81
On system-spanning demixing properties of cell polarization 89
Systematic extension of the Cahn-Hilliard model for motility-induced phase separation 123

1 Extended Abstract

1.1 Introduction

Patterns and self-organization in nature have captivated mankind since ancient times. In the Roman Empire priests called augurs tried to interpret the will of the gods by observing bird flocks [1]. Even longer ago people used beautifully patterned shells of mussels and snails as pieces of jewelery. While the esthetic appeal of skin patterns and the fascination for swarming behavior of animals, for instance, are obvious, the universal principles of patterns and self-organization also attract scientists from many different disciplines [2,3]. Many of them come with the goal to explore and understand the origin and functions pattern fulfill in nature: How does a flock of birds determine its flight direction [4], how does self-driven morphogenesis influence and enable multicellular organisms [5, 6] or how do self-organized patterns help a bacterial cell to divide at the center [7–9]?

Approaching such systems from the point of a pattern formation physicist means not trying to understand all the different mechanisms leading to the phenomena in the systems named above. Instead, pattern formation as a scientific discipline tries to identify generic properties and unifying principles of the pattern itself rather than its realizations in specific systems [10, 11]. Stripe patterns, for instance, occur as convection rolls in the sky [12, 13], as skin pattern of fish [14–17] or as a vegetation pattern in water-limited systems [18–21]. Obviously the length scales of the patterns in these examples as well as the driving mechanisms are completely different. Nevertheless, the stripe patterns themselves inherently have specific features, e.g., considering their stability towards small perturbations [22–24] or response to external forcing [10,25–27]. These features then apply to all systems forming stripe patterns be it in the skies, on fish or in drylands.

In this thesis we focus especially on questions motivated by open biological and chemical questions. However, along the lines of pattern formation theory the results are more adhered to the pattern than to the specific systems and in that sense transferable to other systems. In the first part of this work, we will thereby explore pattern formation in finite domains, i.e. the response of a pattern restricted to a certain space. Furthermore, we will identify and examine a new class of patterns named active phase separation. This demixing phenomenon with active compounds will be explained in more details in the second part of the work.

1.2 Part I: Patterns in finite systems

In nature patterns always emerge in the presence of boundaries. Experiments on Rayleigh-Bénard convection, for instance, take place in a finite convection cell [28]. Chemical reactions are restricted to a finite reactor like a petri dish or the inside of a vesicle [29] or living cell [7]. Considering spatially periodic patterns such as stripes, this means the pattern consists of a finite number of wavelengths. Constraining patterns to a 'short' domain is known to influence the pattern formation process: Convection rolls in Rayleigh-Bénard systems, for instance, orient perpendicular to side walls [10, 30–32]. Apart from orientation, boundaries can also influence the wavelength of stripe patterns, i.e. the boundaries can induce a wavelength selection [10, 33–37]. While the interplay of stripe patterns and boundaries is quite well understood, this is less the case for traveling wave patterns, especially under very strong confinement.

Such strong confinement where the system size consists of just a few wavelengths is of particular interest for reactions that take place on membranes of cells. A prominent example of such a scenario is the cell biological Min protein system [7, 38–40]. The coordinated attachment and detachment of Min proteins from the cytosol to the cell membrane is crucial for the cell division process in the rod-shaped bacterium E. coli. In a living bacterium, the Min proteins shuttle from one cell pole to the other. This dynamic resembles a standing wave pattern where the node of this wave ensures that the division site is located exactly at the cell center. However, the group of P. Schwille managed to extract the principal components of this intracellular reaction and was able to perform experiments on large artificial membranes. They thereby observed that the Min system forms traveling wave pattern on these membranes [41].

In [*pub1*] we raise the question whether these different kinds of patterns – standing wave-like patterns in *in vivo* and traveling waves in *in vitro* experiments – may be a result of restricting the reaction to a small cell. Since we are interested in generic features of patterns in the first place, we analyze this question using a generic model that forms traveling waves. We therefore use the complex Swift-Hohenberg (CSH) for the complex scalar order parameter field $u(x,t)$ in one spatial dimension [42–45]:

$$\partial_t u(x,t) = (\varepsilon + ia)u - \xi_0^2(1+ib)(q_0 + \partial_x^2)^2 u + if\partial_x^2 u - \gamma(1+ic)|u|^2 u. \qquad (1)$$

The CSH model shows traveling wave solutions in extended systems if the control parameter ε is positive. For a biological system, for instance, the total concentration of one of the proteins or a tunable binding rate may take the role of a control parameter. These waves are stable in a wide parameter range and have a preferred wavelength of $\lambda_0 = 2\pi/q_0$. The preferred wavelength also provides an intrinsic

length scale that allows us to meaningfully define 'strong confinement' as system sizes that are just a few times the intrinsic wavelength. Simulating the CSH equation with no-flux boundary conditions leads to significantly different wave solutions depending on the system length L. Figure 1 shows a traveling wave pattern in the

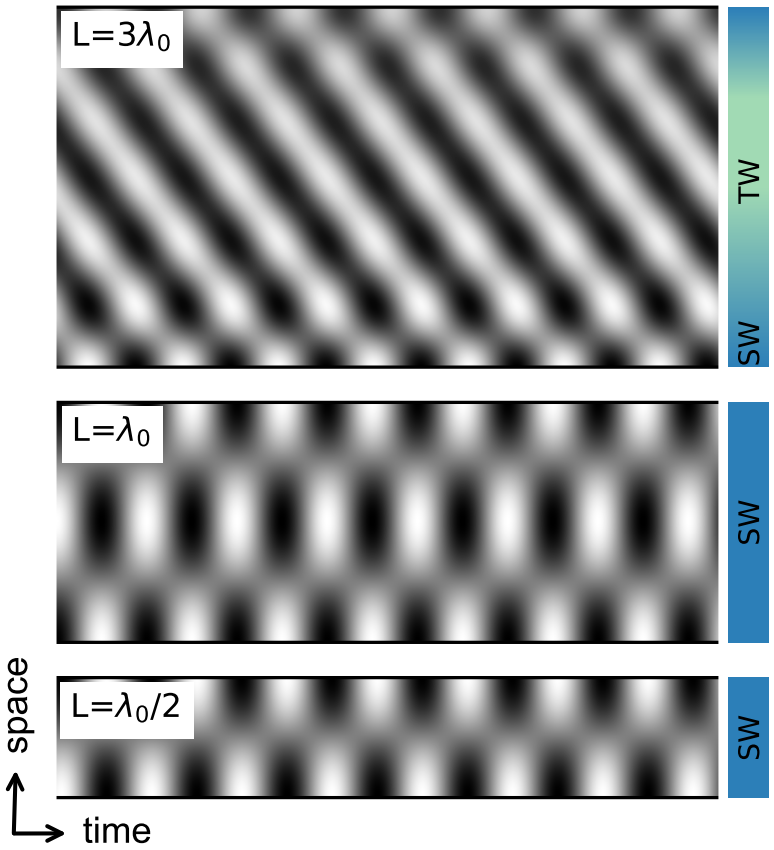

Figure 1: Confinement of traveling wave patterns leads to a significant change of the pattern. Depending on the system length, modulated waves ($L = 3\lambda_0$), two-node ($L = \lambda_0$) or one-node standing waves ($L = \lambda_0/2$) occur in simulations of the CSH equation (see Eq. (1)). The colored sidebar show the regions where to find standing waves (SW) and traveling waves (TW), indicating that the boundary always induces a (local) SW pattern.
Figure adapted from [*pub1*], published under CC-BY 3.0.

center of the system for a moderately short system size ($L = 3\lambda_0$). This pattern is very similar to the one the CSH equation would exhibit in large systems where boundaries are irrelevant. In large systems the two possible wave directions – left and right-moving – are equally likely. However, unlike linear waves like electromag-

netic waves nonlinear waves in general do not superpose. Instead the two opposing wave directions compete, i.e. one direction is spontaneously selected suppressing the other [10, 46]. In the case shown here, we find a right traveling wave in the bulk region. However, confining nonlinear traveling waves additionally leads to a reflection at the boundaries of the system. Considering the field $u(x,t)$ as a sum of left and right traveling waves u_L and u_R, the no-flux boundaries couple both wave directions at the system boundary:

$$0 = \partial_x u(x = 0, L) = \partial_x u_R(x = 0, L, t) + \partial_x u_L(x = 0, L). \tag{2}$$

The coupling via the boundaries forces the right- and left-moving wave into coexistence close to the boundaries. This leads to a forced superposition of both wave directions despite the generic competition between the two in the bulk. Figure 1 also shows the interplay between bulk competition and reflection in case of the system length $L = 3\lambda_0$. Close to the boundaries at the top and bottom the reflection effects dominate, forcing the incoming and reflected wave into a local standing wave. As mentioned before the bulk still shows just one traveling wave direction since the other is suppressed due to nonlinear interactions. Decreasing the system length brings the top and bottom boundary closer together. This means the fraction of the system with boundary-imposed superposition of the wave directions increases. Therefore a decreasing system length inevitable results in a reflection-induced standing wave. Simulations for system lengths $L = \lambda_0$ and $L = \lambda_0/2$ shown in Fig. 1 confirm these considerations: For $L = \lambda_0$ we find a standing wave with two nodes, while for $L = \lambda_0/2$ a one-node standing wave is observed. Accordingly, the system length influences the number of nodes in the standing wave regime. The discovery and exploration of this novel boundary-induced transition from traveling to standing waves by decreasing the system length is the main statement of this work.

We further analyze the transition between the standing wave states with a different number of nodes as well as the transition to traveling waves using linear stability analysis. We therefore calculate the analytical solution for a standing wave solution of Eq. (1), finding

$$u(x,t) = 2Fe^{-i\Omega t}\cos(qx), \tag{3}$$

with

$$F^2 = \frac{1}{3\gamma}[\varepsilon - \xi_0^2(q_0^2 - q^2)^2],$$
$$\Omega = [-a + \xi_0^2 b(q_0^2 - q^2)^2 + fq^2 + 3\gamma c F^2].$$

The no-flux boundary condition for systems of length L thereby only allows a wavenumber q with $q = n\pi/L$, where $n \in \mathbb{N}$ is the number of nodes of the standing

wave solution. This standing wave solution with n nodes exists if $F^2 > 0$, this means if the control parameter exceeds a certain value depending especially on the wavenumber q. The existence border for the standing wave with the lowest control parameter value is depicted as a black line in Fig. 2. Below this curve, the homogenous state $u = 0$ is stable. To determine the stability of a standing waves solution we add a small perturbation and analyze their dynamical behavior. Note that the perturbation also has to match the boundary condition, which allows us to write the perturbation u_p as

$$u_p = e^{\sigma t} \sum_{k=0}^{N} a_k \cos \frac{k\pi x}{L}. \tag{4}$$

If the real part of the growth rate σ is larger than zero, the perturbation will grow in time, rendering the standing wave solution unstable. The results are presented in Fig. 2 as colored regions in the $\varepsilon - L$ plane.

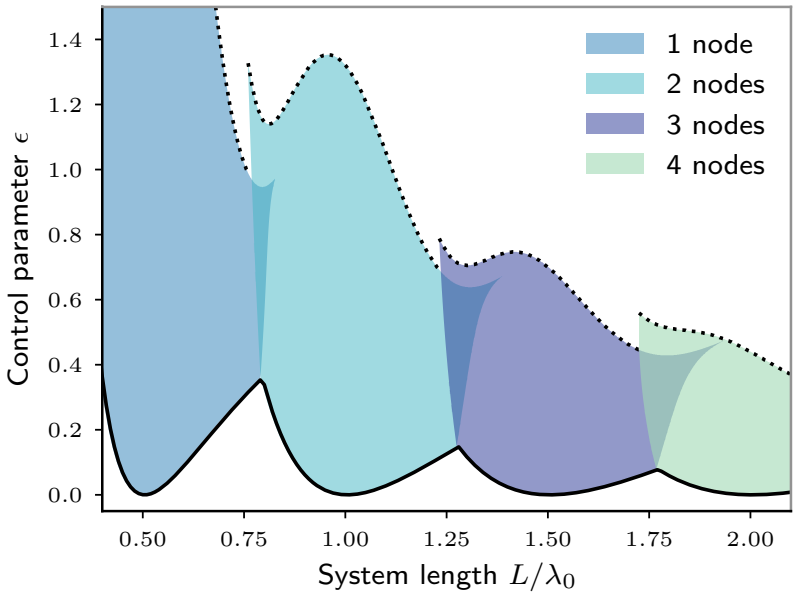

Figure 2: Regions of linear stability for standing waves with a different number of nodes indicated by color-shaded areas. Below the black solid line, the homogeneous state is stable while above the black dashed line traveling waves occur. Figure adapted from [*pub1*], published under CC-BY 3.0.

Thereby each colored region depicts the stability region or so-called Eckhaus stability band for a standing wave with a certain number of nodes. The Eckhaus stability band was originally discussed in systems forming a stripe pattern, where

it measures the width of the q-range for fixed ε where stripe patterns are stable. Comparing the ratio between the bandwidth where stripes exist (existence band) and the bandwidth where they are stable (Eckhaus band) there reveals a well known value of $1/\sqrt{3}$ in large extended systems [22, 23, 47]. Spatially extended systems forming traveling waves also show an Eckhaus stability band in a certain parameter regime [48–50]. However, in contrast to spatially unconstrained systems, the Eckhaus band widens in confined systems and fills the whole existence band. This means for small values of ε and in confined systems standing waves are stable if they exist. Moreover, Fig. 2 shows that the stability regions with n and $n+1$ nodes may overlap. This means there is a region of bistability between different standing wave patterns. Fig. 3b shows the bistable behavior: For $L = 0.79\lambda_0$ both one or two node standing waves are stable and the observed solution depends on the initial condition. Additionally, the linear stability indicates a number of different transitions between patterns. Increasing, for example, the system length can either lead to a direct transition between standing wave patterns with a different number of nodes (like in Fig. 1) or to a transition between standing waves that is intersected by a region with modulated standing waves (see Fig. 3a). Increasing the control parameter for a fixed system length causes the standing wave pattern to loose its stability and we find again modulated traveling waves.

These results are indeed not exclusive to the CSH model but can also be reproduced in for instance a chemical reaction-diffusion system [51] or a model for the Min system [52]. Especially for the latter one these results may be of great importance. The one-node standing waves of our generic CSH model (e.g. Fig. 1, bottom) show a striking resemblance to pole-to-pole oscillations in E. coli during cell division [7, 53]. Our analysis shows that these standing waves generically originate from nonlinear traveling waves via boundary reflection – provided they are confined to a sufficiently short system. In the absence of spatial confinement, the Min protein reaction forms traveling waves on extended functionalized membranes [41]. This suggests that the pole-to-pole oscillations in E. coli are a direct consequence of confining traveling waves to the cell interior. They are thus not a specific feature of the Min system but instead based on generic principles of pattern formation theory for nonlinear waves. In this context, experiments with elongated or filamentous E. coli are particularly interesting, since the further patterns we find in the CSH model also appear in these bacteria: Depending on the bacteria length, the Min proteins also form standing waves with multiple nodes [7, 53–55] or even traveling waves [55]. More importantly though, not only do living bacteria slightly differ in length, they also actively grow. To maintain accurate cell division at the cell center, the pole-to-pole oscillations need to be robust over a range of cell sizes. Indeed, we find that stability of standing waves in a range of system lengths is another generic feature of nonlinear waves. This wavelength variability enables the

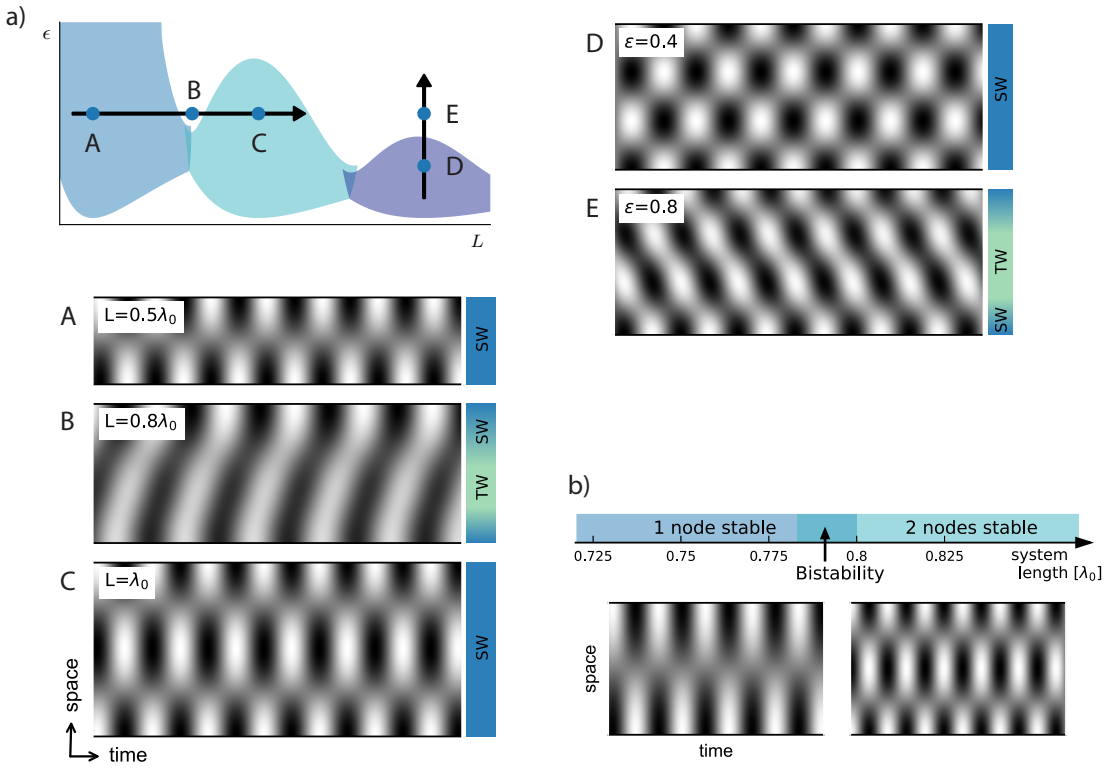

Figure 3: Scenarios for transitions between different wave pattern.
a) Scenarios upon changing system parameters: For fixed control parameter (ABC) changing the system length along the horizontal arrow leads to a transition from a one-node standing wave to a modulated traveling wave to a two-node standing wave. Varying the control parameter along the vertical arrow for a fixed length (DE) we find a transition from a 3-node standing wave to a modulated traveling wave
b) Bistability of a one- and two-node standing wave due to an overlap of the stability regions.
Figure reproduced from [*pub1*], published under CC-BY 3.0.

pole-to-pole oscillations to adapt to the cell size within this stability or Eckhaus range. In fact, E. coli maintain robust pole-to-pole oscillations even as they almost double in length before cell division. Continued cell growth to filamentous bacteria also allows for the observation of transitions between standing waves with different numbers of nodes or to traveling waves [8, 54, 55]. Pattern formation theory therefore captures the essence of the mentioned cell biological phenomena observed in experiments.

A possible extension of our work would be the analysis of strongly confined traveling waves in two spatial dimensions. In this case, in addition to the transition

between traveling and standing waves, one can also observe different directions of the traveling wave. First experiments in the Min system in confined fluidic chambers or experiments where E. coli bacteria were confined to a rectangular domain already reveal that the orientation of the Min waves strongly depends on the ratio of the two-dimensional confinement [53,56–58]. From our results it is a natural assumption that the protein wave aligns in the direction that results in a wavelength closest to its intrinsic wavelength. However, as this assumption still needs confirmation, confinement to two dimensional domains will almost surely lead to interesting and unexpected spatiotemporal behavior.

Considering experiments in the Min system on extended membranes, a different way of confining a system also becomes relevant. In reference [52], the membranes the Min proteins attach to and detach from were microstructured, preventing membrane formation via a gold coating (see also [59] for experimental details). In this way the membrane area and therefore the possibility to attach and detach is confined. In this case there are no 'hard' boundary conditions, since the proteins still diffuse in the cytosol above the gold-coated areas. This resembles a situation that prevents pattern formation in the parts of the gold coating and allows them above the membrane parts. Mimicking such a situation from a modeling perspective would require, for instance, a control parameter that enables pattern formation in a subdomain of the system and suppresses it in the rest. Therefore, the control parameter has to be above the threshold of pattern formation in one region while dropping below this threshold outside. In this way a pattern can be spatially constrained without specific boundary conditions acting on the field at the control parameter drops.

However, considering a spatially dependent control parameter is not only relevant for the Min system but can also be realized in chemical systems where the reaction can be suppressed by illumination [60, 61]. Applying the illumination only to subdomains of the system again restricts the reaction and possible pattern formation to a subdomain of the system without defining a boundary condition along the edge of the illumination mask. Studies of such control parameter drops to confine systems are related to those of parameter ramps. Smooth temperature ramps in convection experiments, for instance, lead to wavenumber selection in one-dimensional or quasi-one-dimensional systems [62–65]. Rapid parameter changes or heterogeneities on the other hand can pin a stripe or traveling wave pattern to the edge that is created by the parameter change [66, 67]. The new results we add to this field in [*pub2*] is the study of two-dimensional systems. We thereby show how the pattern orientation can be controlled by varying the width of the control parameter drop. For this study we use the Brusselator model [68–70], a reaction-diffusion system that shows a supercritical bifurcation to spatially periodic Turing patterns [5]. The Brusselator describes the dynamics of the two concentration fields $u(x, y, t)$ and

$v(x, y, t)$ that can diffuse and react with each other:

$$\partial_t u = \nabla^2 u + a - (b+1)u + u^2 v, \tag{5}$$

$$\partial_t v = D\nabla^2 v + bu - u^2 v. \tag{6}$$

Thereby b is used as a control parameter to switch between a homogenous and a patterned state, while a and D are constants. In contrast to the Swift Hohenberg model [71] –another paradigmatic model for stripe pattern – the Brusselator has a non-zero uniform basic state solution whose exact value also depends on the value of the control parameter, a fact that will become important later on. In principle, the Brusselator allows for two kinds of spatially periodic patterns – stripes and hexagons. For our work we choose the parameters in a way that stripes are preferred if the control parameter is above the threshold value $\beta = 0$, with

$$b = b_c(1 + \beta). \tag{7}$$

Since we do not want to restrict our analysis to the Brusselator model as a singular example, we additionally analyze the problem using the amplitude equation for stripe pattern. Close to the onset of the pattern, the two concentration fields u and v can be described simultaneously with just one equation for the order parameter (or amplitude) A [10, 70, 72] that is defined via

$$(u, v)^T = \mathbf{w}(\mathbf{r}, t) = \mathbf{w}_h + A\tilde{\mathbf{w}}e^{i\mathbf{q}_c\mathbf{r}} + A^\star\tilde{\mathbf{w}}e^{-i\mathbf{q}_c\mathbf{r}}, \tag{8}$$

with the homogenous basic state $\mathbf{w}_h$. Thereby $A(\mathbf{r}, t)$ represents the envelope of the stripe pattern that varies slowly in time and on a length scale much larger than the intrinsic wavelength of the stripes. The equations describing the dynamical behavior of $A(\mathbf{r}, t)$ in two spatial dimensions require information about the orientation of the stripe pattern. However, since the Brusselator model is isotropic, only the magnitude of $\mathbf{q}_c$ is fixed in extended systems but not its orientation. In principle therefore all stripes are equally likely to occur above the pattern formation threshold, typically leading to a labyrinth-like pattern. In our analysis of the amplitude equation, we focus on the two extreme cases, stripes parallel and perpendicular to the x-axis, i.e. $\mathbf{q}_c = (q_c, 0)$ and $\mathbf{q}_c = (0, q_c)$. The equations for the dynamical evolution of the amplitude of these stripes write

$$\partial_t A = \beta A + \mathcal{L}A - g|A|^2 A, \tag{9}$$

with

$$\mathcal{L} = \begin{cases} \mathcal{L}_\parallel^2 := \xi_0^2 \left(\partial_x - \frac{i}{2q_c}\partial_y^2\right)^2 & \text{for } \mathbf{q}_c = (q_c, 0), \\ \mathcal{L}_\perp^2 := \xi_0^2 \left(\partial_y - \frac{i}{2q_c}\partial_x^2\right)^2 & \text{for } \mathbf{q}_c = (0, q_c). \end{cases} \tag{10}$$

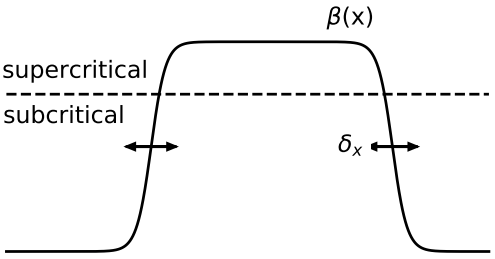

Figure 4: Sketch of the control parameter drop. The control parameter (black line) is supercritical above the dashed line and subcritical below.

The system-specific properties are reflected in the coherence length ξ_0, the critical wavenumber q_c and the nonlinear saturation coefficient g. The great advantage of the amplitude equation is its universality [10, 11, 42]. No matter which stripe-forming system we observe, as long as these stripes evolve from a supercritical bifurcation (which is the case for the Brusselator), they obey this generic amplitude equation [10, 11, 72]. This universality of course comes at the cost of a validity range that is restricted to bifurcation point, i.e. the point where the homogenous state becomes unstable towards the stripe pattern. In many systems, however, the general principles that can be deduced from the amplitude equation and that are strictly valid only close to the threshold of the pattern still prevail in the nonlinear regime. This allows us to transfer the insights from the amplitude equation directly to not only one but many systems.

To model a smooth transition from a domain suppressing patterns to a domain enabling pattern formation, we introduce a spatially dependent control parameter

$$\beta = \beta_0 + \frac{M}{2}\left[\tanh\left(\frac{x - x_l}{\delta_x}\right) - \tanh\left(\frac{x - x_r}{\delta_x}\right)\right] \tag{11}$$

that is varied along the x-direction. Thereby we assume $L := x_r - x_l \gg \lambda_c$, where $\lambda_c = 2\pi/q_c$ is the intrinsic wavelength of the stripe pattern. We then choose β_0 and M in such a way that the control parameter is above the threshold of pattern formation (supercritical) approximately along L and below (subcritical) outside of that domain (see also Fig. 4). The steepness of the control parameter drop around x_l and x_r is controlled with the drop width δ_x. If δ_x is small, the drop almost resembles a step-like control parameter change, while large values of δ_x correspond to a smooth ramp-like transition from sub- to supercritical control parameter values. The control parameter drop breaks the rotational symmetry leading to an anisotropic system. While this control parameter drop can be directly put into the Brusselator model, that is not the case for the amplitude equation. The amplitude equation describes long-scale variations which only allows slow (adiabatic) variations of the control parameter. The rapid variations near x_l and x_r would be

smoothed out on the length scale on which the envelope of the pattern changes and therefore have to be treated separately. Consequently, we separate $\beta(x, \delta_x)$ into an adiabatic and a non-adiabatic part, introducing the long-wave length scale $\delta_A = 2\xi_0/\sqrt{M+\beta_0}$. We define the adiabatic part $B_0(x)$ as

$$B_0(x) = \beta(x, \delta_A). \tag{12}$$

Considering the non-adiabatic part of the control parameter drop especially contributions in resonance with the intrinsic wavelength are crucial for the derivation of the amplitude equation. The general interplay of stripe pattern and spatially resonant forcing has been extensively investigated in the context of thermal convection [25, 26, 73–76]. There, resonance may lead for instance to a locking of the pattern into the wavelength of the external forcing or to changes in the stability regions of the pattern. However, resonant forcing also has similar effects on chemical [77–79] or environmental patterns [27]. In our work the non-adiabatic part of the control parameter takes the role of a forcing term that is in a m:1 resonance with the original pattern with wavenumber q_c. To extract the resonant contributions arising from the non-adiabatic part $\beta_{non}(x) = \beta(x, \delta_x) - B_0(x)$, we expand $\beta_{non}(x)$ in a series of sine functions:

$$\beta_{non}(x) = \frac{M}{2} \sum_m \left\{ B_m^l(x) \sin[m q_c (x - x_l)] + B_m^r(x) \sin[m q_c (x - x_r)] \right\}. \tag{13}$$

Thereby the functions $B_m^{l,r}$ can be represented via a Gaussian and are localized around x_l and x_r respectively. Due to the localization of the prefactors $B_m^{l,r}$, the resonant forcing does not apply to the whole system but only to the area around the control parameter drop. Perpendicular stripes are not affected by the non-adiabatic contributions since the control parameter drop varies in x-direction which can not resonantly couple to stripes with a wavevector in y-direction. Therefore, only the adiabatic contribution plays a role for perpendicular stripes. On the other hand the non-adiabatic contributions to the control parameter constitute a local resonant forcing for parallel stripes. Therefore, the amplitude equation for parallel stripes changes to

$$\partial_t A = B_0(x) A + \mathcal{L}_\parallel^2 A - g|A|^2 A + \sum_m \alpha_m B_m(x) (A^\star)^{m-1}. \tag{14}$$

The function $B_m(x)$ merges the non-adiabatic contributions of both edges of the control parameter drop $B_m^l(x)$ and $B_m^r(x)$. The parameters α_m are constants that depend on the specific system. The different non-adiabatic coefficients $B_m(x)$ influence the stripe pattern in a different way. Thereby the term B_1 that describes a local 1:1-resonance effect has the biggest impact. This coefficient changes the bifurcation from a perfect supercritical in the case $B_1 = 0$ to an imperfect one [26, 80].

We therefore expect a finite amplitude stripe pattern already for negative values of $\beta_m = \beta_0 + M$, i.e. for maximum values of the control parameter that are below the threshold for stripe pattern in an extended system.

This is confirmed via simulations of the Brusselator model and shown in Fig. 5. Because B_1 is finite only close to the edges of the control parameter drop, we find a localized stripe pattern in the vicinity. In the center of the system the non-adiabatic contributions vanish, i.e. the pattern is suppressed because the control parameter is subcritical. Observing the maximum value of the stripe amplitude reveals that it has indeed the form of an imperfect bifurcation (see Fig. 5d). Note that the coefficient B_1 is only present in systems where the control parameter drop influences the basic state of the pattern. While this is the case for the Brusselator model, this is not the case for other prototypic models forming stripes like the Swift-Hohenberg (SH) model where the basic state is and stays $u = u_{\text{homogeneous}} = 0$. The coefficient B_2 describes a local 2:1 resonance, i.e. the wavenumber of the forcing or resonance is twice the intrinsic one. A 2:1 resonance reduces the threshold of the pattern but leaves the form of the bifurcation unchanged [26]. The coefficient B_2 therefore promotes the pattern formation in the subcritical regime close to x_l and x_r. In contrast to the coefficient B_1 that only occurs in systems where the basic state is influenced by the control parameter drop, the coefficient B_2 appears in every system forming stripe patterns, independent of the value of the basic state. The higher contributions $B_m(x)$ with $m > 2$ have a much smaller amplitude and also do not qualitatively change the scenario.

To understand the preferred orientation of the stripe pattern with respect to the control parameter drop we exploit that the amplitude equations in Eq. (14) and Eq. (9) can be derived from a functional via $\partial_t A = -\delta F_{\parallel,\perp}/\delta A^\star$. For the respective stripes the functionals are

$$F_\parallel = \int dxdy\big[- B_0(x)|A|^2 + \frac{g}{2}|A|^4 + |\mathcal{L}_\parallel A|^2 - \sum_{m=1}^{2} \frac{\alpha_m}{m} \left(B_m(x)A^{\star m} + B_m^\star(x)A^m\right)\big] \tag{15}$$

for stripes parallel to the control parameter drop and

$$F_\perp = \int dxdy\big[- B_0(x)|A|^2 + \frac{g}{2}|A|^4 + |\mathcal{L}_\perp A|^2\big] \tag{16}$$

for stripes perpendicular to the drop.

In case of a steep control parameter drop, i.e. small δ_x, the non-adiabatic contributions $B_{1,2}$ have a significant magnitude. Nevertheless, they only appear in the functional $F_\parallel$ for parallel stripes. Because these stripes appear via an imperfect bifurcation, they have a finite amplitude below the bulk threshold $\beta_m = \beta_0 + M = 0$.

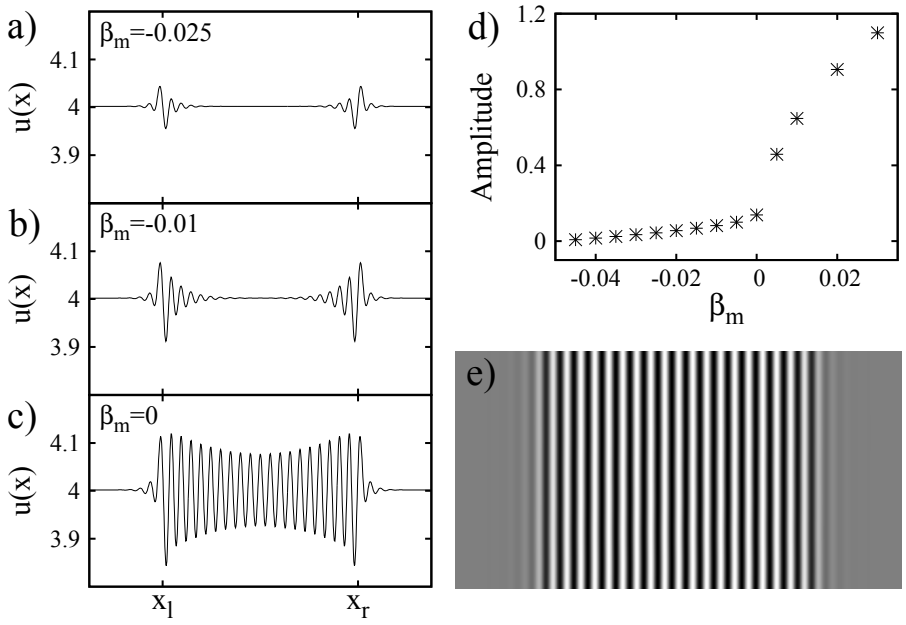

Figure 5: Simulation results for the Brusselator model with a steep control parameter drop. a)-c) show cross-sections along the x-axis for different values of the upper plateau of the control parameter. The onset of pattern formation already occurs for negative β_m close to the control parameter drop.
d) Maximum value of the amplitude of the field reveals that the bifurcation is imperfect. e) Snapshot of the 2D pattern confirming the stripe orientation parallel to the control parameter drop.
Figure adapted from [*pub2*].

For β_m smaller than the bulk threshold, parallel stripes get induced around x_l and x_r where $B_{1,2}$ is finite while perpendicular stripes remain zero. The finite amplitude for parallel stripes decreases the respective functional $F_{\parallel}$ compared to $F_{\perp}$, which remains zero because of the vanishing amplitude of perpendicular stripes. Therefore, steep control parameter drops favor stripes that align parallel to the parameter drop.

However, for a large drop width δ_x, the non-adiabatic contributions become negligible. In this case, the difference between both functionals $F_{\parallel}$ and $F_{\perp}$ is the operator $\mathcal{L}$. For the analysis we assume an envelope A that is homogenous in y-direction and only varies along x. This means both functionals only differ in the order of the spatial derivatives ∂_x, i.e. the functional $F_{\parallel}$ includes the term $|\partial_x A|^2$ while $F_{\perp}$ depends on $|\partial_x^2 A|^2$. Therefore, spatial modulations of the amplitude along the x-axis influence the respective functional in a different way. These different orders of derivatives are known to decrease the functional $F_{\perp}$ in comparison to $F_{\parallel}$ [10,81].

Altogether the considerations regarding the limits of small and large drop widths reveal a different preferred orientation in both cases. This implies a transition between parallel and perpendicular orientation for intermediate δ_x. Simulations of the Brusselator confirm these expectations, visualized in Fig. 6 where stripes orient parallel to the drop for small and perpendicular for large δ_x.

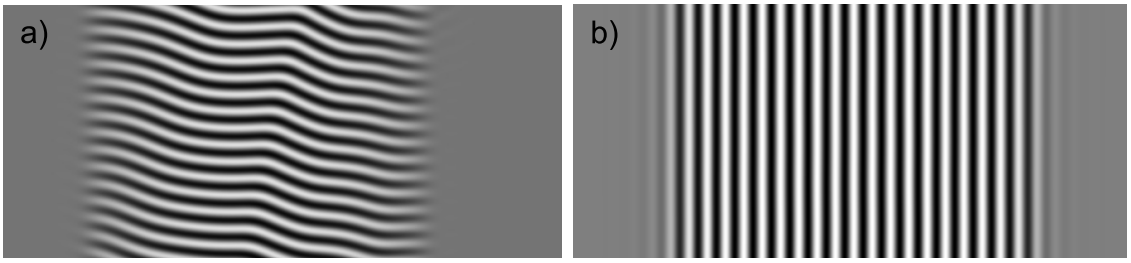

Figure 6: Simulation results for the Brusselator model with control parameter drop: Stripes orient perpendicular to shallow ramp-like drops like in a) and parallel the steep step-like drops in b).
Figure adapted from [*pub2*].

A control parameter drop can not only restrict a pattern along one axis, but also define real two-dimensional domains with a supercritical control parameter. One example are rectangles, that can be realized via

$$\beta = \beta_0 + \frac{M}{4}\left[\tanh\left(\frac{x-x_l}{\delta_x}\right) - \tanh\left(\frac{x-x_r}{\delta_x}\right)\right] \cdot \left[\tanh\left(\frac{y-y_b}{\delta_y}\right) - \tanh\left(\frac{y-y_t}{\delta_y}\right)\right]. \tag{17}$$

This control parameter drop roughly constrains the pattern forming domain to $[x_l, x_r]$x$[y_b, y_t]$. A two-dimensional domain allows for two drop widths δ_x in x-direction and δ_y in y-direction that can be used to influence the orientation of the pattern. If we choose for instance δ_x small and δ_y large, these drop widths prefer stripes that are parallel to the x-axis (via δ_x) and perpendicular to the y-axis (via δ_y) – double-preferring a parallel or vertical stripe pattern. In the same way a perpendicular or horizontal stripe pattern can be created by the exactly opposite drop widths: large δ_x and small δ_y. These combinations lead to a very regular and almost defect-free pattern orientation in two spatial dimensions (see Fig. 7). The observation and understanding of this orientational transition of stripe patterns in confined systems without a hard physical boundary condition is the main point of [*pub2*].

Experimentally, these findings could be confirmed in any light-sensitive reaction-diffusion system that forms stripe patterns. A prominent example is the chlorine

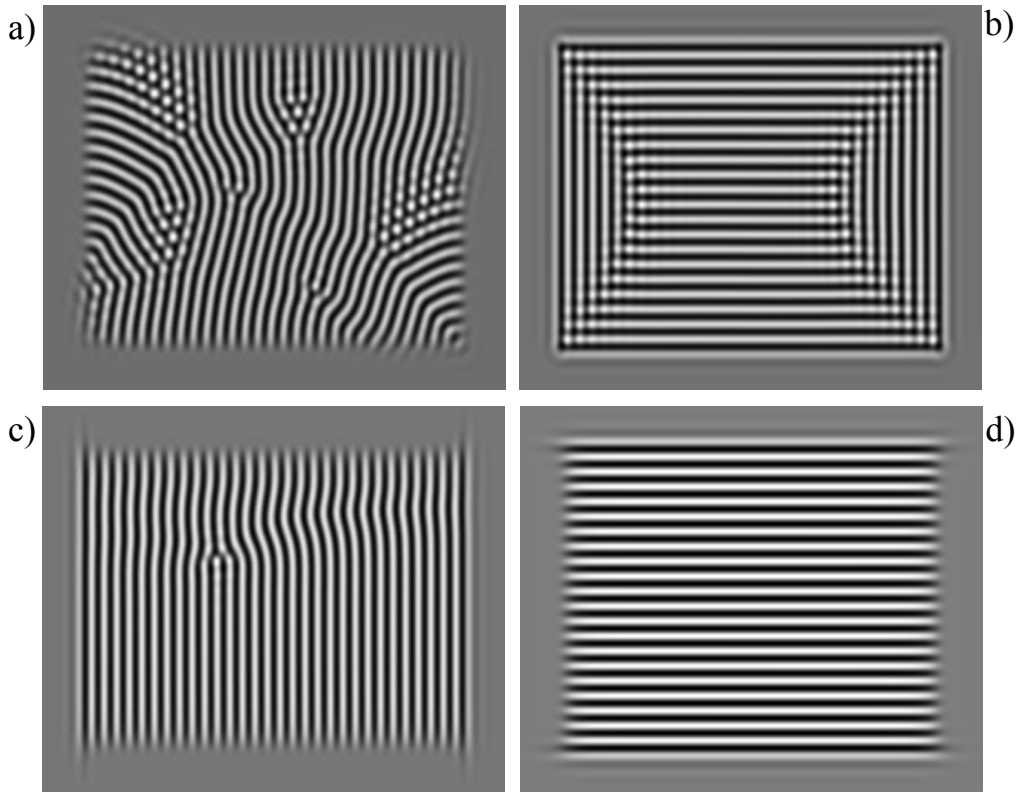

Figure 7: Stripe pattern inside a 2D domain with a supercritical control parameter with different combinations of drop widths. (a) Large drop width along the x- and y- direction favors stipes perpendicular to the domain borders. (b) Small drop widths along both directions lead to stripes parallel to the control parameter drops. (c) Steep drop along the x- and large drop along the y-direction enhances vertical stripes. Switching the drop width compared to (c) reverses the scenario and favors horizontal stripes (d).
Figure adapted from [*pub2*].

dioxide-iodine-malonic acid (CDIMA) reaction. In this reaction different aspects of photosensitive manipulation of patterns such as spatially homogenous forcing or the influence of light with two very different wavelengths are already well-established [82–84]. Applying the illumination via a mask with smooth boundaries in a way that it works like a control parameter drop should be an easy task in this system.

The concept of a control parameter drop to restrict patterns to a finite domain can be applied not only to stripe but also to wave patterns. In contrast to stripe patterns where 1:1-resonance effects play the defining role (see [*pub2*]), traveling waves can only couple to 2:1-resonant contributions of the control parameter drop. This property is explained in the following considering the complex Swift-Hohenberg

(CSH) model in Eq. (1) as an example. If we introduce a control parameter drop like in Eq. (11) instead of a constant control parameter ε, the product of, for instance, a left-moving wave u_L and the 2:1-resonant, i.e. non-adiabatic, contribution to the control parameter drop lead to

$$B_2(x)u_L = \underbrace{B_2(x)}_{\propto e^{2iq_c x}} A_L e^{i(-q_c x-\omega t)} \propto e^{(iq_c x-\omega t)}, \tag{18}$$

i.e. a right-moving wave. Other resonant contributions do not lead to a wave with opposite direction but only to the excitation of higher harmonics. This means a left-moving wave 'hitting' the control parameter drop induces a right-moving wave – the left-moving wave is 'reflected' in a special way at the drop. However, note that the reflection effect is based on the excitation of a counter-propagating wave due to a local 2:1-resonance. The reflection of nonlinear waves at real physical boundaries is known to induce interesting spatiotemporal behavior in convecting binary fluid mixtures [46, 85–89]. Note that these systems are finite but not as strongly confined as the example we studied in [*pub1*]. A similar behavior can also be expected in reaction-diffusion models that show a bifurcation to traveling waves [90]. In [*pub3*] we illuminate whether control parameter drops have a similar effect on nonlinear traveling wave patterns as physical boundary conditions such as the wall of a convection cell.

We analyze this question using again the CSH model in Eq. (1) as a generic model for traveling wave patterns. As we will see the group velocity of traveling waves is an important parameter that defines four different scenarios. In the following examples we always use a right-moving wave as initial condition and a rather steep control parameter drop, i.e. a small value of δ_x, ensuring that the local reflection coefficient $B_2(x)$ is sufficiently large. Keep in mind that in extended systems, a dominant initial right-moving wave will suppress any left-moving wave that is also a solution of Eq. (1).

For a system with a control parameter drop and small group velocities, we find the scenario shown in Fig. 8a: The traveling wave pattern fills the whole area with a supercritical control parameter $[x_l, x_r]$ (filled state). Increasing the group velocity leads to a so-called confined state – the domain of the traveling wave pattern shrinks and vanishes in a range around x_l (see Fig. 8b). The confined state arises because the local wave pattern around x_l is transported to the right with the group velocity. Since the wave pattern does not grow homogeneously but is transported away from x_l, no pattern is observed around the left border. Accordingly, this effect becomes more and more relevant with increasing group velocity. However, for both filled and confined states, the reflection effect at the boundary only plays a minor role. Even if the right-moving wave induces a left-moving wave at $x = x_r$, the reflected wave is almost immediately suppressed by the dominant right-moving wave in the

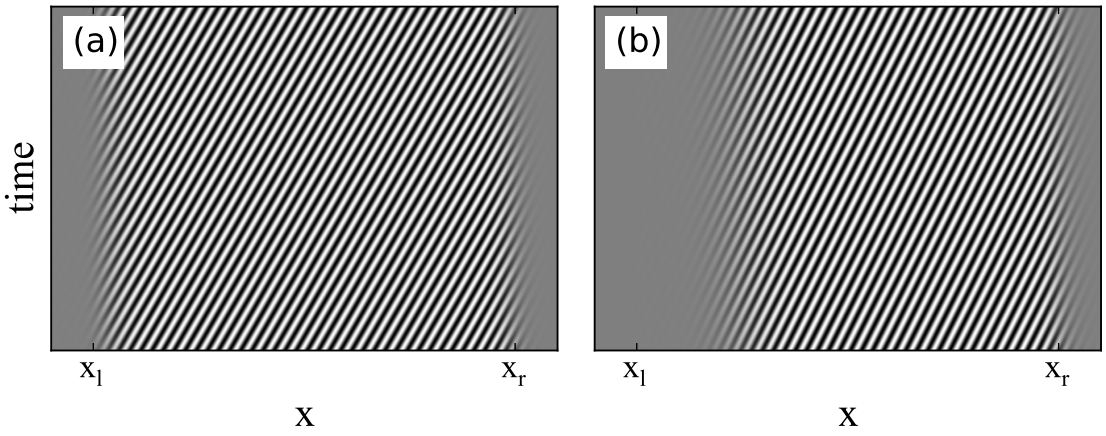

Figure 8: Space-time plots of simulation results of the complex Swift-Hohenberg with a control parameter drop in 1D. Depending on the group velocity the wave pattern spans the whole supercritical domain (a) or is shifted to the right with increasing group velocity (b).
Figure adapted from [*pub3*].

bulk.

Raising the group velocity further will lead to a point where the pattern is theoretically transported beyond $x = x_r$. In extended systems this is called convective instability [42, 91] and means that the pattern is transported faster than a perturbation can grow. Therefore the pattern only grows in the comoving frame. At a stationary point the perturbations will be transported away, seemingly leading to a stable homogeneous state. In confined systems, however, one could expect the wave pattern to vanish completely because the perturbations are transported into the domain with a subcritical control parameter that suppresses pattern formation. This is indeed the case for ramp-like control parameter drops, i.e. large drop widths.

For steeper control parameter drops, crossing the border to convective instability does surprisingly not lead to a disappearance of the pattern. Instead, we observe an interesting spatiotemporal behavior where the envelope of the wave pattern becomes time-dependent. Fig. 9 shows this so-called blinking state. Even if the right-moving wave is still dominant close to $x = x_r$, the left-moving wave now also has a considerable amplitude near the left control parameter drop. Moreover, the envelopes of both wave directions also vary in time: While the envelope or amplitude of the left-moving wave decays completely before it grows again in a periodic fashion, the tail of the right-moving wave wiggles back and forth periodically. Even higher values of the group velocity lead to a return of waves with stationary amplitude shown in Fig. 10. Here we find a dominant right-moving wave close to the

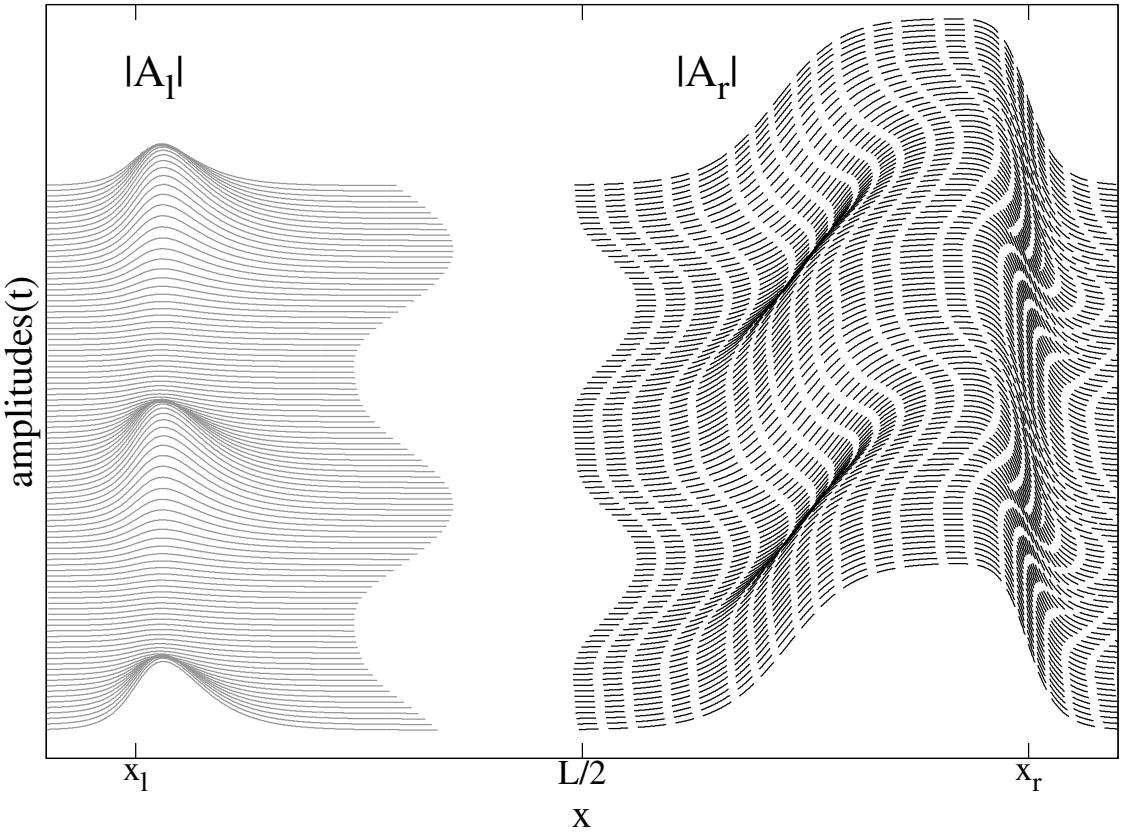

Figure 9: Time evolution of the envelopes of a left moving wave ($|A_l|$) and a right moving wave ($|A_r|$) forming a blinking state.
Figure adapted from [*pub3*].

right control parameter drop and a left-moving wave near the left one forming a counter-propagating wave state. Thereby the exact ratio of the amplitude of both wave directions depends on the group velocity. The appearance of especially the left-moving wave near the left 'boundary' can be understood as follows: Due to the high group velocity the initial right-moving wave pattern is shifted to the right half of the supercritical region $[x_l, x_r]$. If this wave comes close to the right control parameter drop, it induces a left-moving wave due to the non-adiabatic resonant contribution $B_2(x)$. The left-moving wave itself is advected with the group velocity. Since the group velocity is so large, the pattern reaches the left half of the supercritical domain without being eliminated by the competition with the right-moving wave. In this left half, the amplitude of the right-moving wave is zero so that the left-moving wave pattern can evolve without an antagonist.

The exact values of the transitions between the different scenarios for the wave patterns not only depend on the group velocity v_g but also on the strength of the resonance-induced reflection, i.e. the value of the drop width δ_x. In [*pub3*] we there-

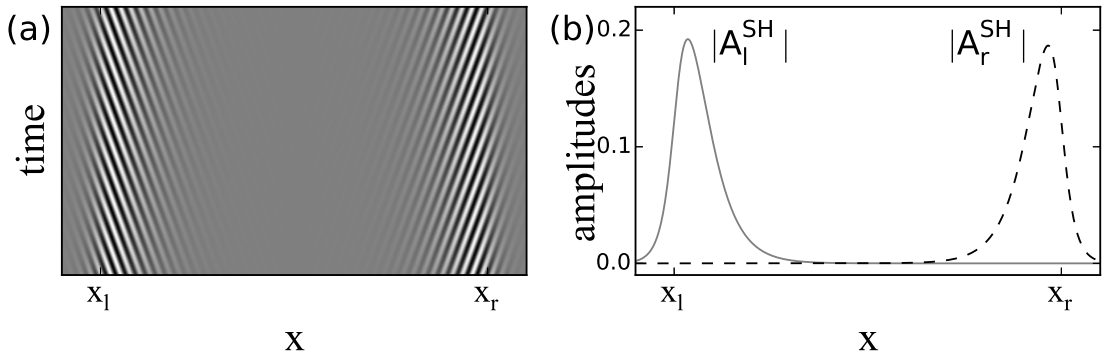

Figure 10: Space-time plot (a) and envelope (b) of a counter-propagating wave state. Close to the left control parameter drop the left moving wave is dominant while the right moving is on the opposite end of the supercritical domain. Figure adapted from [*pub3*].

fore also quantify the interplay between reflection strength and group velocity via a phase diagram in the δ_x-v_g-plane. This reveals the regions along the v_g-axis where blinking and counter-propagating waves exist shrink with increasing drop width. This renders the blinking and counter-propagating wave states a clear product of the interplay between effects of the convective instability and the resonance-induced reflection.

Moreover we complement our findings with the analysis of the amplitude equation for traveling waves. Our results are thus not restricted to any specific model but rather generic properties of nonlinear traveling waves confined to a finite domain via a control parameter drop. Therefore these findings might particularly apply to the beforementioned Min system on extended membranes, where membrane formation is controlled via gold coating [52]. In such biological systems binding rates that can be tuned with light are an imaginable way to implement a control parameter drop. A more direct application would be chemical systems that show wave patterns as in [92, 93] and are light-sensitive. For such chemical systems, applying spatially dependent illumination masks would be a great way to test our generic results.

A possible next step to [*pub2*] and [*pub3*] would be an analysis of traveling wave patterns with a control parameter drop in two spatial dimensions. In the Min system there are already experiments on narrow membrane channels created by gold coating where traveling waves orient perpendicular to the channel 'walls'. Note that the walls are not a rigid physical boundary but resemble more the concept of a control parameter drop as described before. This orientation effect could be an extension or the results for stationary patterns in [*pub2*] to traveling waves. Confining these waves not only into a channel but into an elongated rectangle might – with the results of [*pub3*] in mind – lead to interesting and complex spatiotemporal behavior.

In summary, the first part of this thesis shows that restricting patterns to a finite domain crucially influences the pattern formation process. Thereby both 'hard' physical boundaries like walls and 'soft' boundaries like a control parameter drop lead to effects that differ essentially from the behavior of the bulk pattern. Our work shows some universal aspects of this scenario that are rather independent of the system details. Regarding the Min system especially, this suggests that nature may use these universal principles of pattern formation as a building block to perform important functions in living matter.

1.3 Part II: Active phase separation

Apart from the formation of spatiotemporal patterns, demixing of multicomponent systems is another important example for self-organization in everyday life. For instance, food like ice cream [94] or also ointments [95] are emulsions of basically water and oil droplets. In this case, demixing into a water- and oil-rich phase is undesired and has to be prevented. Another example are technical applications such as solar cells [96–99] or piezoelectrics [100] that make use of demixing in their manufacturing process. This requires deep understanding and control of the spatial arrangement of the components. Another example are metallic alloys, that are often prepared at high temperature in a fluid phase and then cooled down in a specific way to ensure desired properties in the crystalline state such as hardness [101, 102].

From a physics point of view, two competing basic principles govern the behavior of phase separating systems. On the one hand, the system tries to maximize its entropy, which would lead to a perfectly mixed system. On the other hand, there may be repulsive forces between different substances for example due to the minimization of the surface energy that tends to keep substances separated. The strength of both these effects depends, for example, on the temperature. This means that, for instance, a binary mixture possesses a critical point of miscibility – a temperature below which the system tends to separate into two phases [103] (there are also exceptions where the temperature dependence is the other way around).

Spinodal decomposition is a special kind of phase separation [104–106]. During spinodal decomposition the initially homogeneous state becomes unstable towards long-wave perturbations. However, these perturbations themselves are also unstable leading to a coarsening process. The theoretical framework of spinodal decomposition is the so-called Cahn-Hilliard (CH) equation that describes the phase separation process of a binary mixture [107, 108].

While all of the previous examples of phase separation take place in or close to thermal equilibrium, similar phenomena were observed in active, non-equilibrium systems. One of those is cell polarization that plays a big role in both cell loco-

motion [109–113], where e.g. actin filaments accumulate in protrusions of the cell to enable forward motion, as well as in cell division [9, 110, 114, 115]. In the latter case, proteins assemble in distinct halves of the cell, resembling two phases in a liquid-liquid mixture. Other similar examples can be found in active matter [116], the formation of biomembranes [117, 118] as well as in chemotactically communicating cells or colloids [119–121] that may form clusters depending on the particle or cell density. Self-propelled particles with different motility [122–124] or density dependent velocity [125–127] show a similar effect. Even mussel beds [128] or ion-channel densities [129] form patterns similar to classical phase separation. All of these examples have in common that they locally consume energy to actively move or propel, clearly rendering them non-equilibrium systems. Nevertheless, the phase separation seems on first glance similar to spinodal decomposition. The second part of this thesis will reveal and explore the connection between the examples of what we call active phase separation to phase separation in or close to thermal equilibrium.

In [*pub4*] we address this question exemplarily analyzing a minimal reaction-diffusion model for cell polarization. We thereby consider a molecule or protein that exists in two conformations – representing a fast diffusing cytosolic and a slowly diffusing membrane-bound state. Even if more realistic models often involve a plethora of different molecules, minimal models can serve as a starting point to gain fundamental insights into the process of cell polarization [130–132]. On the time scale of the cell polarization, the involved proteins only switch their conformation but are not created or destroyed. Therefore the total number of proteins is conserved. This conservation constraint is another connection between different systems showing active phase separation. Mathematically a minimal model for membrane-cytosol exchange can be written as

$$\partial_t \tilde{u} = D_u \tilde{u} + f(\tilde{u}, \tilde{v}), \tag{19a}$$

$$\partial_t \tilde{v} = D_v \tilde{v} - f(\tilde{u}, \tilde{v}). \tag{19b}$$

The field $\tilde{u}$ thereby represents the concentration of the membrane-bound conformation of the protein and $\tilde{v}$ the concentration of the cytosolic conformation. The conversion between these two states is described via the symmetric reaction term

$$f(\tilde{u}, \tilde{v}) = -b\tilde{u} + (\tilde{u} + \tilde{v})^2 - (\tilde{u} + \tilde{v})^3. \tag{20}$$

The scalar parameter b defines different polarization states that will be explained later. Equation (19) has a homogeneous state u_h, v_h that may become unstable with respect to small perturbations if a chosen control parameter – we use the diffusion constant D_v here – exceeds a certain value. The dispersion relation $\sigma(q)$ of the small perturbations thereby approximately depends on the perturbation wavenumber q

like

$$\sigma(q) = G_2 q^2 - G_4 q^4, \tag{21}$$

where G_2 and G_4 are parameters that can be calculated from the original system parameters. Since $G_4 > 0$, the sign of G_2 determines the stability of the homogenous state: If G_2 is negative, the homogenous state is stable and becomes unstable if G_2 becomes positive. Importantly, in contrast to classical Turing patterns, the band of unstable wavenumbers ranges down to $q = 0$ for conserved reaction-diffusion systems. If we consider the model in Eq. (19) close to the threshold where the homogenous state becomes unstable, we can perform a weakly nonlinear analysis. To measure the distance from the onset of the instability, we introduce a small parameter ε. We then express the fields (u, v) in terms of this small parameter. Furthermore we also introduce 'slow' or long wavelength scalings for the time- and spatial scale. Inserting the scalings and the expansion of the fields into the full model in Eq. (19) allows to sort all the terms with respect to their order in ε, leading to a separation into several equations in the different orders of ε. Thereby the lowest order in ε provides an equation linear in the fields that is solved via

$$\mathbf{w}_1 = (u_1, v_1)^T = A \begin{pmatrix} \partial_v f|_{u=u_h, v=v_h} \\ -\partial_u f|_{u=u_h, v=v_h} \end{pmatrix}. \tag{22}$$

The free parameter A however is not a constant but depends on the new time- and spatial scale. The dependency of A on space and time can be determined by successively solving the equations in the higher orders of ε. The detailed calculation is described in [*pub4*], [*pub5*] and [*pub6*] especially in the supporting information to [*pub5*]. The procedure is a conceptual parallel to the derivation of the amplitude equation for systems forming stripe patterns (Ginzburg-Landau equation) [10, 72, 133, 134]. While the Ginzburg-Landau equation delivers an envelope equation for systems where this order parameter is not conserved, our result can be seen as the amplitude equation for systems with conserved order parameter. However, in contrast to the Ginzburg-Landau equation, the equations that determine the amplitude A in the conserved case appear in higher orders of ε ($\mathcal{O}(\varepsilon^{5/2})$ instead $\mathcal{O}(\varepsilon^{3/2})$). After returning to the original time and spatial scale, we identify the resulting amplitude equation for the cell polarization as the Cahn-Hilliard equation [107]:

$$\partial_t A = -\partial_x^2 [\alpha_1 \varepsilon A + \alpha_2 \partial_x^2 A - \alpha_3 A^2 - \alpha_4 A^3]. \tag{23}$$

The coefficients α_i are completely determined by the original system parameters, allowing for a direct mapping of Eq. (19) to the CH equation in a certain parameter range. Note that the quadratic term that usually does not appear in the CH

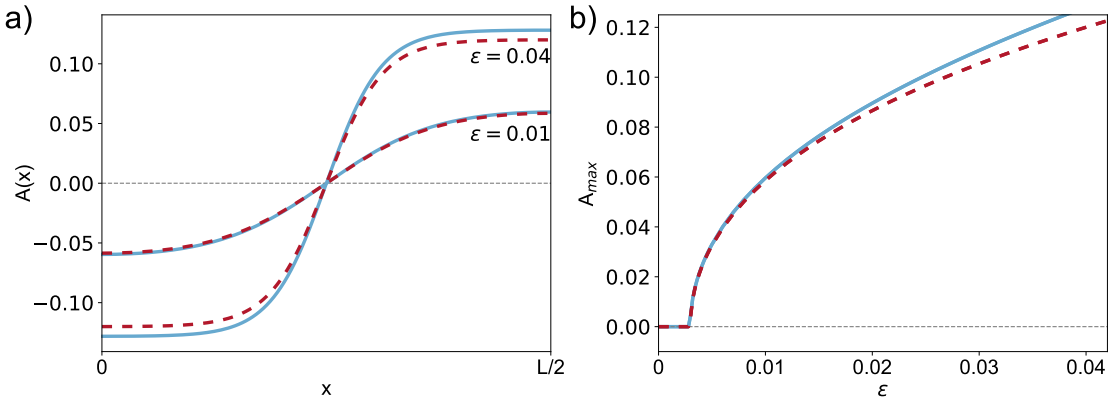

Figure 11: a): Steady state profiles of the basic cell polarization model in Eqs. (19),(20) (blue solid line) and the corresponding CH equation (see Eq. (23)) (red dashed line) in the symmetric case for different values of the control parameter.
b): Comparison of the upper plateau values (maximum of $A(x)$) of the stationary polarized states as a function of the control parameter in the symmetric case. The polarization model is again shown as solid blue line while the CH model is shown in dashed red. The polarized state occurs via a supercritical bifurcation. Figure adapted from [*pub4*], ©2018 American Physical Society

equation can be removed via a transformation $A \to \tilde{A} - \alpha_3/(3\alpha_4)$ and an appropriate redefinition of the prefactors α_i. The CH equation was originally introduced to describe phase separation in equilibrium systems [107, 108]. Our new reduction method shows that it also captures the essence of active phase separation in a simple cell polarization model. The existence of this common underlying order parameter equation therefore proofs the fundamental connection between phase separation in and outside of thermal equilibrium.

To determine the validity range of our approach, we compare numerical simulations of the conserved reaction-diffusion model in Eq. (19) to the CH equation (see Eq. (23)) with the corresponding coefficients α_i. Focusing on stationary solutions, we find the following behavior: For a parameter choice where the coefficient $\alpha_3 = 0$ ($b = 2$), the phase-separated or polarized state is perfectly $\pm$-symmetric (at least close to $\varepsilon = 0$), i.e. the plateau values of the profiles have the same absolute value (see Fig. 11a). Due to the conservation condition the areas with increased and decreased concentration also have to be of equal size and each occupies half the system. The CH equation reflects this behavior perfectly for small values of the control parameter. Increasing the control parameter leads to increasing deviations between the universal CH equation and the full polarization model. This means with increasing distance from the onset of cell polarization, the system-specific

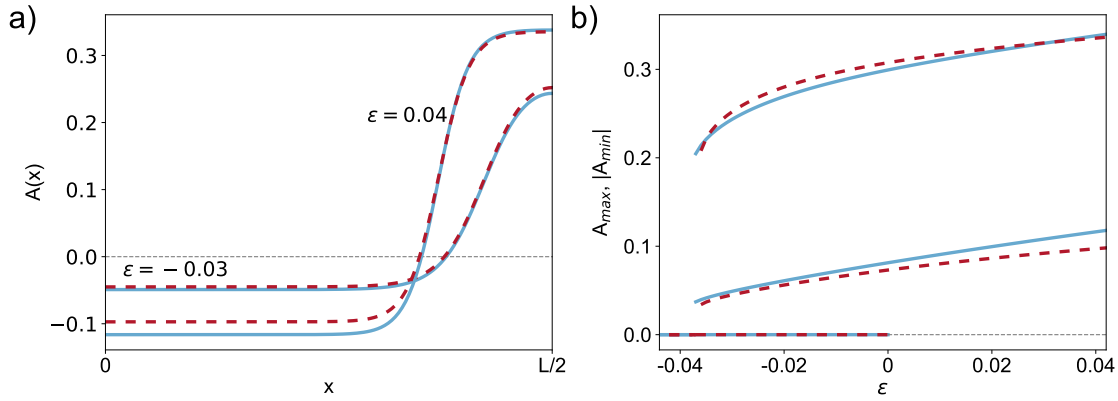

Figure 12: a): Steady state profiles of the basic cell polarization model in Eqs. (19),(20) (solid blue line) and the corresponding CH equation (see Eq. (23)) (dashed red line) in the asymmetric case for different values of the control parameter.
b): Comparison of the upper (maximum of $A(x)$ and lower plateau values (minimum of $A(x)$) of the stationary polarized states in the asymmetric case as a function of the control parameter. The polarized state occurs via a subcritical bifurcation.
Figure adapted from [*pub4*], ©2018 American Physical Society

properties become more and more influential. Figure 11b illustrates this behavior and additionally shows that in the case $\alpha_3 = 0$ the bifurcation to the polarized state is supercritical. In case of a finite value of α_3 ($b \neq 0$) the scenario slightly changes. The profiles in Fig. 12a show that the broken $\pm$-symmetry in the CH equation leads to an asymmetrically polarized state. The area of decreased concentration is now larger than the area of increased concentration compared to the mean value. Nevertheless, the CH model is again a good representation of the full model close to the onset of polarization. Comparing the plateau values as a function of ε in Fig. 12b also reveals that the bifurcation is no longer smooth. Instead, we find a jump from $A_{max} = 0$ to finite plateau values, rendering the bifurcation subcritical. Moreover, the polarized state now already may occur for $\varepsilon < 0$ which leads to a region where the polarized and the homogenous state (that is stable for $\varepsilon < 0$) coexist. We therefore observe a hysteretic behavior when increasing the control parameter: If we start in the homogeneous state with $\varepsilon < 0$ and slowly increase the control parameter, the system stays in the homogeneous state until this state becomes unstable at $\varepsilon = 0$. However, starting in the polarized state with $\varepsilon > 0$ and decreasing the control parameter, the polarized state will prevail even in a range where $\varepsilon < 0$.

These findings are not restricted to the minimal toy model for cell polarization

in Eq. (19). In [*pub5*] we confirmed this for a more realistic polarization model by Otsuji et al. [113, 135] using,

$$f(\tilde{u}, \tilde{v}) = a_1 \left(\tilde{v} - \frac{\tilde{u} + \tilde{v}}{(a_2(\tilde{u} + \tilde{v} + 1)^2} \right). \tag{24}$$

This conceptual model is designed to capture the behaviour of the Rho-GTPases, a regulator molecule for cell polarity. During cell migration Rho-GTPases stimulate molecular motors like actin or myosin to spatially control the contractility, allowing the cell to move [136, 137]. In the same publication we also showed that in principle any mass-conserved reaction diffusion system that has the form of Eq. (19) falls into the class of active phase separation.

In the context of cell polarization the dynamical evolution of the polarization is important as well. The CH model is well-known to show coarsening behavior in large systems [108]. During the coarsening the average length scale L of the pattern or phase separated areas grows with a power-law $L \propto t^{1/3}$ in two spatial dimensions [138]. In Fig. 13 we confirm that the polarization model in Eq. (19) and Eq. (24) exhibits the same dynamics: At the beginning, the homogenous basic state becomes unstable to perturbations with a certain wavenumber q_{max} that corresponds to the maximum of the dispersion relation in Eq. (21). Since the system length is much larger than the length scale of this perturbation, a labyrinth-like state with areas of high and low concentration evolves. However, these small-scale phase separated areas are themselves unstable towards long-wave perturbations. This leads to coarsening, i.e. to larger and larger areas with the same concentration, finally reaching a completely polar state.

But undergoing a coarsening process to reach a polar state might be too slow for the biological purposes of a polarizing cells. For instance, if a cell wants to move into a certain direction to escape a predator, it has to polarize quickly and can not afford to undergo a coarsening process. Instead cells 'need' a direct transition from a homogenous to a polar state. This is not only important for the mentioned predator-prey scenario but also for tasks like cell division (in exactly two daughter cells). Our analysis and the knowledge about the coarsening process allows to identify suitable parameter regions where one can expect such a direct transition: A direct transition takes place if the wavenumber of the maximum of the dispersion relation or rather the corresponding wavelength is in the order of the system length. In this case the most unstable wavelength already is the largest possible wavelength that fits into the system. Therefore in such systems no coarsening occurs.

On the other hand, the principle of coarsening also has an important upside. As mentioned, a cell usually wants to reach a polar state. If for some reason the system would evolve towards a state with two polar zones, it tends to coarsen to a state with just one polar zone – the system has a built-in safety net, which is crucial

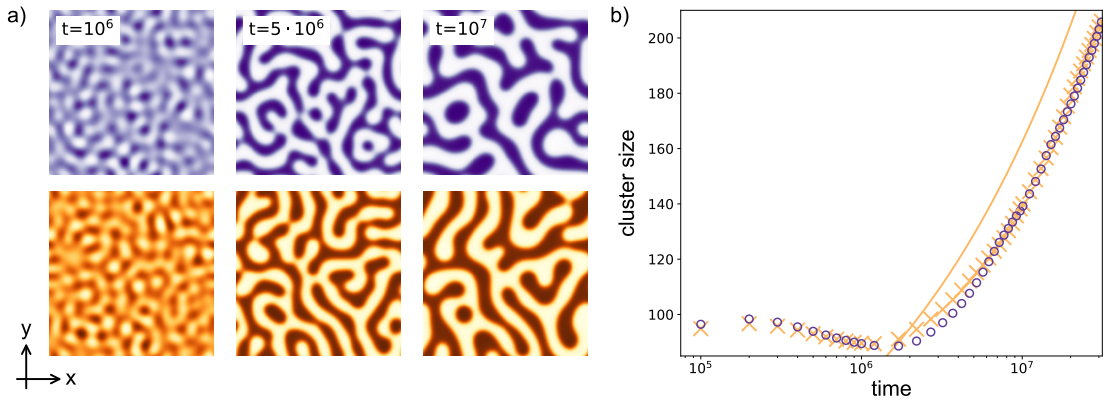

Figure 13: a): 2D snapshots of the dynamics of the polarization model in Eqs. (19),(24) (violet) and the corresponding CH equation (see Eq. (23)) (orange) for different times. As time progresses the patterns coarsen to larger and larger pattern.
b): Average cluster size or dominant length scale of the pattern on the left side as a function of time. The violet circles show the dynamics of the full polarization model, while the orange crosses depict the temporal evolution of the length scale in the CH model. The solid line corresponds to the analytical value of $L \propto t^{1/3}$. Figure adapted from [*pub5*]. Published under CC-BY 4.0

regarding the importance of the polarization process. Additionally, the fact that the system tends to settle into the largest possible wavelength allows for length adaptability of the polar zones, allowing cells of slightly different size to polarize correctly as well. Length adaptability is not the only feature that appears in many models and systems showing cell polarization. The ability to spontaneously polarize or to maintain a polar state even if the external stimulus is no longer present are features that can be observed in various systems (see [130] and references therein). Since the CH equation also shows these features, multiple similarities between cell polarization models can be explained as follows: Presumably, many polarization models can be mapped onto the CH equation close to the bifurcation to the polarized state. They therefore all share the features such as length adaptability or spontaneous polarization the CH equation shows as an underlying order parameter equation.

Apart from cell polarization, the reduction scheme is also applicable to systems describing the clustering of cells that communicate chemotactically. The social amoeba Dictyostelium discoideum is one prominent example for such a system. This slime mold spends most of its life as unicellular organism in the forest soil. However, if the living conditions become dire, the mold emits a chemical signal leading to an aggregation of many amoeba to form a so-called fruiting body – a

multicellular slug that allows some of them to survive harsh conditions [139–141].

Mathematically, such chemotactically communicating cells can be described by two mean-fields – one representing the cell density ρ and one representing the concentration of the signal molecule for the chemotaxis c – the ability to detect and move along a chemical gradient [142]. An extended Keller-Segel model is one possibility to describe the interactions between those two fields [119, 143–145]:

$$\partial_t \rho = \partial_x^2 \rho - s\partial_x \left(\frac{\rho}{1+\beta\rho} \partial_x c \right), \tag{25}$$

$$\partial_t c = D_c \partial_x^2 c + \rho - c. \tag{26}$$

Thereby the parameter s describes the chemotactic sensitivity of the cells that serves as a control parameter to trigger the clustering. Note that in this model only the number of cells is conserved while the signaling molecule concentration is not. This molecule is produced by the cells and degraded in time. Nevertheless, as we show in [*pub4*], this model can again be reduced to a CH equation (see Eq. (23)), despite the fact that it has completely different transport mechanisms than the conserved reaction-diffusion model discussed before. A more detailed analysis of Keller-Segel models as an example for active phase separation can be found in the thesis of Lisa Rapp [146].

A further example that falls into the class of active phase separation is the so called motility-induced phase separation (MIPS) [147–150] (see [*pub6*]). MIPS unites systems of self-propelled particles whose swimming speed depends on the particle density of their surrounding. If the swimming speed decreases sufficiently with the local particle density, these systems undergo a phase transition from a homogenous state to a state with two phases of different densities. This two-phase state thereby consists of a dilute gas-like state that spatially coexists with a dense liquid-like state. Experimental examples are bacteria that perform quorum sensing, i.e. 'measure' the density of their surroundings and reduce their motility if the local cell density is high [151, 152]. The phenomenon also appears in artificial swimmers like Janus particles [153]. Examples are gold colloids where one hemisphere is coated with platinum or polymer spheres with an embedded hematite cube. Putting these particles in a solution containing hydrogen peroxide leads to a self-propulsion of the particles consuming H_2O_2 [125, 126]. Another propulsion mechanism involves, e.g., carbon-coated Janus particles in a near-critical solution of water and lutidine. Heating these particles with a widened laser beam leads to heat absorption especially by the carbon hemisphere, pushing the temperature of the surrounding binary fluid above the critical point. The local demixing of the surrounding fluid then leads to phoretic forces allowing the particles to propel [127]. These particle-based approaches can be coarse-grained into a mean-field model that

we analyze in [*pub6*] [154–156]. This model describes the particle motion using a density field ρ and a polarization or orientation field p. The density field thereby evolves via

$$\partial_t \rho = -\partial_x \left[v(\rho) p - D_e \partial_x \rho \right]. \tag{27}$$

D_e describes the effective diffusion coefficient of the active particles while $v(\rho)$ is the density dependent propulsion speed of the particles:

$$v(\rho) = v_0 - \zeta \rho + \lambda^2 \partial_x^2 \rho, \tag{28}$$

where v_0 is the speed of a singular particle. The contribution $\zeta\rho$ reflects the decrease in the particle speed with increasing density. The last term includes that particles possibly sample their neighborhood on a length λ that is larger than the extend of the particle, i.e. including non-local effects of the swimming speed [156, 157]. The density ρ is coupled to the polarization field p via

$$\partial_t p = -\partial_x P(\rho) + D_e \partial_x^2 p - p. \tag{29}$$

involving a 'pressure' term

$$P(\rho) = \frac{1}{2} v(\rho) \rho \tag{30}$$

due to the directed motion of the particles, diffusion and the loss of orientation due to rotational diffusion. Since our analysis shows that the polarization field p follows the density field ρ adiabatically, we focus our further analysis on ρ instead of the coupled field $\mathbf{w} = (\rho, p)$. As for cell polarization and chemotaxis, we managed to show that despite completely different microscopic mechanisms the continuum model for MIPS in Eqs. (27),(29) can again be mapped onto the CH equation. The CH equation is therefore also a leading order description for MIPS. However, in the context of MIPS, the importance of higher order nonlinearities has recently been excessively discussed [158, 159]. These may be able to explain a discrepancy between the behavior of the CH equation and observations in colloidal systems showing MIPS: While the CH equation, as mentioned before, coarsens and forms larger and larger areas of the same density, the growth of clusters in colloidal systems often stops from a certain point on and the cluster size remains finite. Our approach now poses the possibility to quantitatively derive these higher order contributions directly from the original model without relying on phenomenological arguments. [*pub6*] shows that extending the weakly nonlinear analysis to the next higher order leads to

$$\begin{aligned} \partial_t \rho = \partial_x^2 \big[&(\alpha_1 + \beta_1)\rho + (\alpha_2 + \beta_2)\partial_x^2 \rho + (\alpha_3 + \beta_3)\rho^2 \\ &-\alpha_4 \rho^3 + \beta_5 (\partial_x \rho)^2 + \beta_6 \partial_x^2 (\rho^2) \big]. \end{aligned} \tag{31}$$

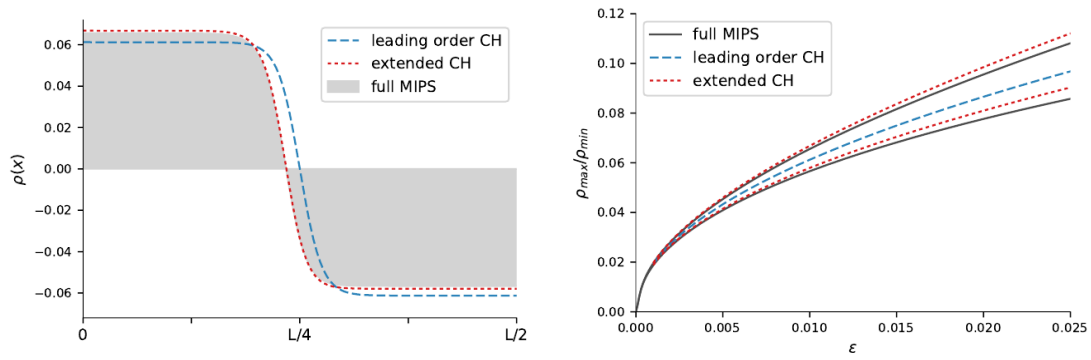

Figure 14: (a) Comparison of steady state profiles of the particle density for the continuum model for MIPS in Eqs. (27),(29) (shaded grey) and the corresponding first and second order approximations by the CH (dashed blue) i.e. extended CH model (red dotted).
(b) Plateau values in the phase separated state for MIPS (black solid), CH (dashed blue) and the extended CH model (red dotted). The extended CH model is able to reproduce the broken $\pm\rho$-symmetry of the full model.
Figure adapted from [*pub6*]. Reprinted with kind permission of The European Physical Society (EPJ) ©EDP Sciences

Thereby the coefficients α_i represent the leading order description, i.e. the CH equation. Close to the onset of MIPS, only these contributions play a role since the coefficients β_i vanish near the threshold. Further away from the threshold the coefficients β_i can be separated into two groups. β_1, β_2 and β_3 are higher order corrections to terms that already exist at the leading order (with prefactors α_1, α_2 and α_3). Thereby the term β_3 captures the fact that the phase separation becomes asymmetric with increasing distance from the onset even in the case $\alpha_3 = 0$. Remember that in the case $\alpha_3 = 0$ the phase separation is symmetric at the onset. The β_5- and β_6-term, however, constitute new nonlinearities that may also qualitatively change the behavior of the system. Note that theoretically also a nonlinearity $\propto \partial_x^2\rho^4$ would be of the same order as the contributions $\beta_5\partial_x^2(\partial_x A)^2$ and $\beta_6\partial_x^4 A^2$. For the specific continuum model for MIPS we use (see Eqs. (27),(29)) the prefactor of such a contribution vanishes. Yet since the extension to higher order nonlinearities is not restricted to MIPS but universal for systems showing active phase separation, the contribution $\propto \partial_x^2\rho^4$ should also be taken into account in a generic analysis. Perhaps the most instructive way to show the relevance of the higher order contributions for MIPS is to compare stationary solutions of the basic model in Eqs. (27),(29) to both the first order CH equation ($\beta_i = 0$) and the extended CH equation (see Eq. (31)). Comparing the profiles in Fig. 14a clearly shows that including the higher order contributions to the CH equation

leads to a much better and in fact almost perfect representation of the full model. Comparing the plateau values in Fig. 14b as a function of ε confirms this impression. Additionally this figure clearly shows that the effect of an increasing asymmetry of the phase separated profile with increasing distance from the threshold is captured by the extended CH model. In [*pub6*] we also compare to which extent the CH and the extended CH model represent the dispersion relation and the critical values of the original model for MIPS.

Furthermore, we compare our results to different phenomenological models for MIPS that are based on symmetry considerations [158–160]. Since our analysis delivers the values of the parameters β_i as a function of the original system parameters, we are able to determine the relevance of different nonlinearities compared to others. For instance in the case of MIPS, the coefficient β_5 is always much larger than β_6 for small values of λ – a condition that is necessary to find MIPS at all.

Altogether our work sheds light on the existence of a universal phase separation phenomenon in active systems. We showed the wide range of systems that fall into the category of active phase separation. Our generic approach allows to directly map the original models onto one universal equation. This equation turns out to be the CH equation that was introduced as a model for phase separation in equilibrium systems. Being described by the same universal order parameter equation reveals that the similarities between phase separation in equilibrium and active phase separation are not coincidental.

Exploring the effects of higher order contributions to the extended CH equation, especially regarding their influence on the dynamics, might be a route for future work. Also regarding these higher order contributions explicitely in 2D is still rather unexplored territory: While in one dimension, for instance, a term $\partial_x A \partial_x^2 A$ is equal to $1/2\partial_x(\partial_x A)^2$, that is not the case for $\nabla(\nabla A)^2$ and $1/2(\nabla^2 A)(\nabla A)$ in two dimensions . This incentivizes discovering presumably complex and rich scenarios in two dimensions. In one dimension extending our approach to even higher orders will prove interesting. In the order $\varepsilon^{7/2}$, a new linear term $\propto \partial_x^6 A$ will appear in the CH equation. This term has the possibility to drastically change the dispersion relation from describing a long-wave instability to a dispersion relation that allows for a finite wavelength instability. This would open a whole new field that in principle also allows a finite wavelength pattern instead of a coarsening process further above the threshold. Such finite wavelength patterns in phase-separating systems are known from block copolymers where the phase separation is arrested in so-called microphase separation [161,162]. However, this example again takes place in or close to thermal equilibrium. Our approach would open the route to observing a non-equilibrium counterpart of microphase separation. This might be especially relevant to understand phenomena like bubbly phase separation or the reversal of

Ostwald ripening that is observed in simulations of MIPS [159, 163]. Additionally transitions from active phase separation to active microphase separation may occur, that can be described and understood on the basis of our work.

1.4 Bibliography

[1] M. T. Cicero. *Über die Wahrsagung/De divinatione*. De Gruyter Akademie Forschung, Berlin, 2013.

[2] D. W. Thompson. *On growth and form*. Cambridge University Press, Cambridge, 1917.

[3] P. Ball. *The Self-Made Tapestry: Pattern Formation in Nature*. Oxford Univ. Press, Oxford, 1998.

[4] T. Vicsek and A. Zafeiris. Collective motion. *Phys. Rep.*, 517:71, 2012.

[5] A. Turing. The chemical basis of morphogenesis. *Philos. Trans. R. Soc. Lond., B, Biol. Sci.*, 237:37, 1952.

[6] S. Kondo and T. Miura. Reaction-diffusion model as a framework for unterstanding biological pattern formation. *Science*, 329:1616, 2010.

[7] D. M. Raskin and P. A. J. de Boer. Rapid pole-to-pole oscillation of a protein required for directing division to the middle of Escherichia coli. *Proc. Natl. Acad. Sci. USA*, 96:4971, 1999.

[8] M. Loose, K. Kruse, and P. Schwille. Protein self-organization: Lessons from the Min system. *Annu. Rev. Biophys.*, 40:315, 2011.

[9] N. W. Goehring, P. K. Trong, J. S. Bois, D. Chowdhury, E. M. Nicola, A. A. Hyman, and S. W. Grill. Polarization of PAR proteins by advective triggering of a pattern-forming system. *Science*, 334:1137, 2011.

[10] M. C. Cross and P. C. Hohenberg. Pattern formation outside of equilibrium. *Rev. Mod. Phys.*, 65:851, 1993.

[11] M. C. Cross and H. Greenside. *Pattern Formation and Dynamics in Nonequilibrium Systems*. Cambridge Univ. Press, Cambridge, 2009.

[12] R. A. Brown. Longitudinal instabilities and secondary flows in the planetary boundary layer: A review. *Rev. Geophys. Space Phys.*, 18:683, 1980.

[13] D. Etling and R. A. Brown. Roll vortices in the planetary boundary layer: A review. *Bound.-Layer Meteorol.*, 65:215, 1993.

[14] S. Kondo and R. Asai. A reaction-diffusion wave on the skin of the marine angelfish *Pomacanthus*. *Nature*, 376:765, 1995.

[15] M. Yamaguchi, E. Yoshimoto, and S. Kondo. Pattern regulation in the stripe of zebrafish suggests an underlying dynamic and autonomous mechanism. *Proc. Natl. Acad. Sci. USA*, 104:4790, 2007.

[16] S. Kondo, M. Iwashita, and M. Yamaguchi. How animals get their skin pattern: Fish pigment pattern as a live Turing wave. *Int. J. Dev. Biol.*, 53:851, 2009.

[17] A. P. Singh and C. Nüsslein-Volhard. Zebrafish stripes as a model for vertebrate colour pattern formation. *Curr. Biol.*, 25:R81, 2015.

[18] C. A. Klausmeier. Regular and irregular patterns in semiarid vegetation. *Science*, 284:1826, 1999.

[19] E. Meron. *Nonlinear Physics of Ecosystems*. CRC Press, Boca Raton, Florida, 2015.

[20] J. von Hardenberg, E. Meron, M. Shachak, and Y. Zarmi. Diversity of vegetation patterns and desertification. *Phys. Rev. Lett.*, 87:198101, 2001.

[21] Y. R. Zelnik, E. Meron, and G. Bel. Gradual regime shifts in fairy circles. *Proc. Natl. Acad. Sci. USA*, 112:12327, 2015.

[22] W. Eckhaus. *Studies in Non-Linear Stability Theory*. Springer, Berlin, 1965.

[23] M. Lowe and J. P. Gollub. Pattern selection near the onset of convection: The Eckhaus instability. *Phys. Rev. Lett.*, 55:2575, 1985.

[24] L. Kramer and W. Zimmermann. On the Eckhaus instability for spatially periodic patterns. *Physica D*, 16:221, 1985.

[25] M. Lowe, J. P. Gollub, and T. Lubensky. Commensurate and incommensurate structures in a nonequilibrium system. *Phys. Rev. Lett.*, 51:786, 1983.

[26] P. Coullet. Commensurate-incommensurate transition in nonequilibrium systems. *Phys. Rev. Lett.*, 56:724, 1986.

[27] R. Manor, A. Hagberg, and E. Meron. Wavenumber locking and pattern formation in spatially forced systems. *New J. Phys.*, 11:063016, 2009.

[28] M. Lappa. *Thermal Convection: Patterns, Evolution and Stability*. Wiley, Chichester, 2009.

[29] O. Steinbock and S.C. Müller. Radius-dependent inhibition and activation of chemical oscillations in small droplets. *J. Phys. Chem. A*, 102:6485, 1998.

[30] H. S. Greenside, W. M. Coughran Jr., and N. L. Schryer. Nonlinear pattern formation near the onset of Rayleigh-Bénard convection. *Phys. Rev. Lett.*, 49:726, 1982.

[31] J. P. Gollub, A. R. McCarriar, and J. F. Steinman. Convective pattern evolution and secondary instabilities. *J. Fluid. Mech.*, 125:259, 1982.

[32] H. S. Greenside and W. M. Coughran Jr. Nonlinear pattern formation near the onset of Rayleigh-Bénard convection. *Phys. Rev. A*, 30:398, 1984.

[33] M. C. Cross, P. G. Daniels, P. C. Hohenberg, and E. D. Siggia. Phase-winding solutions in a finite container above the convective threshold. *J. Fluid Mech.*, 127:155, 1983.

[34] Y. Pomeau and P. Manneville. Wavelength selection in cellular flows. *Phys. Lett. A*, 75:296, 1980.

[35] L. Kramer and P. C. Hohenberg. Effects of boundary conditions on spatially periodic states. *Physica D*, 13:357, 1984.

[36] L. Kramer and H. Riecke. Wavelength selection in Rayleigh–Bénard convection. *Z. Physik B*, 59:245, 1985.

[37] V. Steinberg, G. Ahlers, and D. S. Cannell. Pattern formation and wavenumber selection by Rayleigh-Bénard convection in a cylindrical container. *Phys. Scr*, 32:534, 1985.

[38] J. Lutkenhaus. Assembly dynamics of the bacterial MinCDE system and spatial regulation of the Z ring. *Annu. Rev. Biochem.*, 76:539, 2007.

[39] V. W. Rowlett and W. Margolin. The bacterial Min system. *Curr. Biol.*, 23:R553, 2013.

[40] L. Wettmann and K. Kruse. The Min-protein oscillations in Escherichia coli: an example of self-organized cellular protein waves. *Phil. Trans. R. Soc. B*, 373:20170111, 2018.

[41] M. Loose, E. Fischer-Friedrich, J. Ries, K. Kruse, and P. Schwille. Spatial regulators for bacterial cell division self-organize into surface waves in vitro. *Science*, 320:789, 2008.

[42] I. Aranson and L. Kramer. The world of the complex Ginzburg–Landau equation. *Rev. Mod. Phys.*, 74:99, 2002.

[43] B. A. Malomed. Nonlinear waves in nonequlibrium systems of the oscillatory type, part I. *Z. Physik B*, 55:241, 1984.

[44] I. Aranson and L. Tsimring. Domain walls in wave patterns. *Phys. Rev. Lett.*, 75:3273, 1995.

[45] L. Gelens and E. Knobloch. Traveling waves and defects in the complex Swift-Hohenberg equation. *Phys. Rev. E*, 84:056203, 2011.

[46] M. C. Cross. Structure of nonlinear traveling-wave states in finite geometries. *Phys. Rev. A*, 38:3593, 1988.

[47] M. A. Dominguez-Lerma, D. S. Cannell, and G. Ahlers. Eckhaus boundary and wave-number selection in rotating Couette-Taylor flow. *Phys. Rev. A*, 34:4956, 1986.

[48] B. Janiaud, A. Pumir, D. Bensimon, V. Croquette, H. Richter, and L. Kramer. The Eckhaus instability for traveling waves. *Physica D*, 55:269, 1992.

[49] P. Kolodner. Extended states of nonlinear traveling-wave convection. I. The Eckhaus instability. *Phys. Rev. A*, 46:6431, 1992.

[50] Y. Liu and R. E. Ecke. Eckhaus-Benjamin-Feir instability of rotating convection. *Phys. Rev. Lett.*, 78:4391, 1997.

[51] L. Yang, M. Dolnik, A. M. Zhabotinsky, and I. R. Epstein. Pattern formation arising from interactions between Turing and wave instabilities. *J. Chem. Phys.*, 117:7259, 2002.

[52] J. Schweizer, M. Loose, M. Bonny, K. Kruse, I. Mönch, and P. Schwille. Geometry sensing by self-organized protein patterns. *Proc. Natl. Acad. Sci. USA*, 109:15283, 2012.

[53] K. Zieske and P. Schwille. Reconstitution of pole-to-pole oscillations of Min proteins in microengineered Polydimethylsiloxane compartments. *Angew. Chem. Int. Ed.*, 52:459, 2013.

[54] E. Fischer-Friedrich, G. Meacci, J. Lutkenhaus, H. Chaté, and K. Kruse. Intra- and intercellular fluctuations in Min-protein dynamics decrease with cell length. *Proc. Natl. Acad. Sci. USA*, 107:6134, 2010.

[55] M. Bonny, E. Fischer-Friedrich, M. Loose, P. Schwille, and K. Kruse. Membrane binding of MinE allows for a comprehensive description of Min-protein pattern formation. *PLoS Comput. Biol.*, 9:e1003347, 2013.

[56] F. Wu, B. G. C. van Schie, J. E. Keymer, and C. Dekker. Symmetry and scale orient Min protein patterns in shaped bacterial sculptures. *Nat. Nanotechnol.*, 10:719, 2015.

[57] Y. Caspi and C. Dekker. Mapping out Min protein patterns in fully confined fluidic chambers . *eLife*, 5:e19271, 2016.

[58] F. Wu, J. Halatek, M. Reiter, E. Kingma, E. Frey, and C. Dekker. Multistability and dynamic transitions of intracellular Min protein patterns. *Mol. Syst. Biol.*, 12:873, 2016.

[59] J. T. Groves, N. Ulman, and S. G. Boxer. Micropatterning fluid lipid bilayers on solid supports. *Science*, 275:651, 1997.

[60] A .P. Muñuzuri, M. Dolnik, A. M. Zhabotinsky, and I. R. Epstein. Control of the Chlorine Dioxide-Iodine-Malonic acid oscillating reaction by illumination. *J. Am. Chem. Soc.*, 121:8065, 1999.

[61] A. K. Horváth, M. Dolnik, A .P. Muñuzuri, A. M. Zhabotinsky, and I. R. Epstein. Control of Turing structures by periodic illumination. *Phys. Rev. Lett.*, 83:2950, 1999.

[62] L. Kramer, E. Ben-Jacob, H. Brand, and M. C. Cross. Wavelength selection in systems far from equilibrium. *Phys. Rev. Lett.*, 49:1891, 1982.

[63] D. S. Cannell, M. A. Dominguez-Lerma, and G. Ahlers. Experiments on wave number selection in rotating Couette-Taylor flow. *Phys. Rev. Lett.*, 50:1365, 1983.

[64] M. C. Cross. Wave-number selection by soft boundaries near threshold. *Phys. Rev. A*, 29:391, 1984.

[65] P. C. Hohenberg, L. Kramer, and H. Riecke. Effects of boundaries on one-dimensional reaction-diffusion equations near threshold. *Physica D*, 15:402, 1985.

[66] H. Riecke. Pattern selection by weakly pinning ramps. *EPL*, 2:1, 1986.

[67] H. Ke, Z. Zhang, and O. Steinbock. Scroll waves pinned to moving heterogeneities. *Phys. Rev. E*, 91:032930, 2015.

[68] I. Prigogine and R. Lefever. Symmetry breaking instabilities in dissipative systems II. *J. Chem. Phys.*, 48:1695, 1968.

[69] D. Walgraef. *Spatio-Temporal Pattern Formation.* Springer, New York, 1997.

[70] B. Peña and C. Pérez-García. Stability of Turing patterns in the Brusselator model. *Phys. Rev. E*, 64:056213, 2001.

[71] J. Swift and P. C. Hohenberg. Hydrodynamic fluctuations at the convective instability. *Phys. Rev. A*, 15:319, 1977.

[72] A. C. Newell and J. A. Whitehead. Finite bandwidth, finite amplitude convection. *J. Fluid Mech.*, 38:279, 1969.

[73] R. E. Kelly and D. Pal. Thermal convection with spatially periodic boundary conditions: Resonant wavelength excitation. *J. Fluid Mech.*, 86:433, 1978.

[74] P. Coullet and D. Repaux. Strong resonances of periodic patterns. *EPL*, 3:573, 1987.

[75] S. Weiss, G. Seiden, and E. Bodenschatz. Pattern formation in spatially forced thermal convection. *New. J. Phys.*, 14:053010, 2012.

[76] S. Weiss, G. Seiden, and E. Bodenschatz. Resonance patterns in spatially forced Rayleigh-Bénard convection. *J. Fluid Mech.*, 756:293, 2014.

[77] V. Petrov, Q. Ouyang, and H. L. Swinney. Resonant pattern formation in a chemical system. *Nature*, 388:655, 1997.

[78] M. Dolnik, I. Berenstein, A. M. Zhabotinsky, and I. R. Epstein. Spatial periodic forcing of Turing structures. *Phys. Rev. Lett.*, 87:238301, 2001.

[79] S. Rüdiger, D. G. Míguez, A. P. Muñuzuri, F. Sagués, and J. Casademunt. Dynamics of Turing patterns under spatiotemporal forcing. *Phys. Rev. Lett.*, 90:128301, 2003.

[80] R. Peter, M. Hilt, F. Ziebert, J. Bammert, C. Erlenkämper, N. Lorscheid, C. Weitenberg, A. Winter, M. Hammele, and W. Zimmermann. Stripe-hexagon competition in forced pattern-forming systems with broken up-down symmetry. *Phys. Rev. E*, 71:046212, 2005.

[81] B. A. Malomed and A. A. Nepomnyashchy. Two-dimensional stability of convection rolls in the presence of a ramp. *EPL*, 21:195, 1993.

[82] M. Kærn, R. Satnoianu, A. P. Muñuzuri, and M. Menzinger. Controlled pattern formation in the CDIMA reaction with a moving boundary of illumination. *Phys. Chem. Chem. Phys.*, 4:1315, 2002.

[83] L. Haim, A. Hagberg, R. Nagao, A. P. Steinberg, M. Dolnik, I. R. Epstein, and E. Meron. Fronts and patterns in a spatially forced CDIMA reaction. *Phys. Chem. Chem. Phys.*, 16:26137, 2014.

[84] R. Nagao, R. C. C. de Miranda, I. R. Epstein, and M. Dolnik. Modulation of Turing patterns in the CDIMA reaction by ultraviolet and visible light. *J. Phys. Chem. A*, 123:992, 2019.

[85] M. C. Cross. Traveling and standing waves in binary-fluid convection in finite geometries. *Phys. Rev. Lett.*, 57:2935, 1986.

[86] E. Moses, J. Fineberg, and V. Steinberg. Multistability and confined traveling-wave patterns in a convecting binary mixture. *Phys. Rev. A*, 35:2757, 1987.

[87] J. Fineberg, E. Moses, and V. Steinberg. Spatially and temporaly modulated traveling-wave pattern in convecting binary mixtures. *Phys. Rev. Lett.*, 61:838, 1988.

[88] P. Kolodner and C. M. Surko. Weakly nonlinear traveling-wave convection. *Phys. Rev. Lett.*, 61:842, 1988.

[89] N. Garnier, A. Chiffaudel, and F. Daviaud. Nonlinear dynamics of waves and modulated waves in 1D thermocapillary flows. II. Convective/absolute transitions. *Physica D*, 174:30, 2003.

[90] A. B. Rovinsky, A. M. Zhabotinsky, and I. R. Epstein. Target patterns arising from short-wave instability in near-critical regimes of reaction-diffusion systems. *Phys. Rev. E*, 56:2412, 1997.

[91] I. S. Aranson, L. Aranson, L. Kramer, and A. Weber. Stability limits of spirals and traveling waves in nonequilibrium media. *Phys. Rev. A*, 46:R2992, 1992.

[92] A. M. Zhabotinsky, M. Dolnik, and I. R. Epstein. Pattern formation arising from wave instability in a simple reaction-diffusion systems. *J. Chem. Phys.*, 103:10306, 1995.

[93] M. Dolnik, A. M. Zhabotinsky, A. B. Rovinsky, and I. R. Epstein. Spatiotemporal pattern in a reaction-diffusion system with wave instability. *Chem. Eng. Sci.*, 55:223, 2000.

[94] C. Clarke. *The Science of Ice Cream*. Royal Society of Chemistry, Cambridge, 2004.

[95] M. E. Aulton and K. M. G. Taylor. *Aulton's Pharmaceutics*. Elsevier, Edinburgh, 2017.

[96] C.-W. Chu, H. Yang, W.-J. Hou, J. Huang, G. Li, and Y. Yang. Control of the nanoscale crystallinity and phase separation in polymer solar cells . *Appl. Phys. Lett.*, 92:103306, 2008.

[97] N. D. Treat and M. L. Chabinyc. Phase separation in bulk heterojunctions of semiconducting polymers and fullerenes for photovoltaics. *Annu. Rev. Phys. Chem.*, 65:59, 2014.

[98] L. Zhang, X. Xing, L. Zheng, Z. Chen, L. Xiao, B. Qu, and Q. Gong. Vertical phase separation in bulk heterojunction solar cells formed by in situ polymerization of fulleride. *Sci. Rep.*, 4:5071, 2014.

[99] N. Li, J. D. Perea, T. Kassar, M. Richter, T. Heumueller, G. J. Matt, Y. Hou, N. S. Güldal, H. Chen, S. Chen, S. Langner, M. Berlinghof, T. Unruh, and C. J. Crabec. Abnormal strong burn-in degradation of highly efficient polymer solar cells caused by spinodal donor-acceptor demixing. *Nat. Commun.*, 8:14541, 2017.

[100] T. Huang, S. Yang, P. He, J. Sun, S. Zhang, D. Li, Y. Meng, J. Zhou, H. Tang, J. Liang, G. Ding, and X. Xie. Phase-separation-induced PVDF/graphene coating on fabrics towards flexible piezoelectric sensors. *Appl. Mater. Interfaces*, 10:30732, 2018.

[101] J. S. Langer. Theory of spinodal decomposition in alloys. *Ann. Phys.*, 65:53, 1971.

[102] A. Mazoni, H. Daoud, R. Völkl, U. Glatzel, and N. Wanderka. Phase separation in equiatomic AlCoCrFeNi high-entropy alloy. *Ultramicroscopy*, 132:212, 2013.

[103] P. M. Chaikin and T. C. Lubensky. *Principles of condensed matter physics*. Cambridge Univ. Press, Cambridge, 1995.

[104] J. W. Cahn. On spinodal decomposition. *Acta Metall.*, 9:795, 1961.

[105] P. G. de Gennes. Dynamics of fluctuations and spinodal decomposition in polymer blends. *J. Chem. Phys.*, 72:4756, 1980.

[106] J. D. Gunton, M. San Miguel, and P. S. Sahni. The dynamics of first order phase transitions. *Ph. Transitions Crit. Phenom.*, 8:269, 1983.

[107] J. W. Cahn and J. E. Hilliard. Free energy of a nonuniform system: I. interfacial free energy. *J. Chem. Phys.*, 28:258, 1958.

[108] A. J. Bray. Theory of phase-ordering kinetics. *Adv. Phys.*, 43:357, 1994.

[109] L. P. Cramer T. J. Mitchison. Actin-based cell motility and cell locomotion. *Cell*, 84:371, 1996.

[110] B. Alberts, A. Johnson, J. Lewis, M. Raff, K. Roberts, and P. Walter. *Molecular Biology of the Cell*. Garland Science, New York, 2002.

[111] A. J. Ridley, M. A. Schwartz, K. Burridge, R. A. Firtel, M. H. Ginsberg, G. Borisy, J. T. Parsons, and A. R. Horwitz. Cell migration: Integrating signals from front to back. *Science*, 302:1704, 2003.

[112] A. Jilkine and A. F. Marée and L. Edelstein-Keshet. Mathematical model for spatial segregation of the Rho-family GTPases based on inhibitory crosstalk. *Bull. Math. Biol.*, 69:1943, 2007.

[113] M. Otsuji, S. Ishihara, C. Co, K. Kaibuchi, A. Mochizuki, and S. Kuroda. A mass conserved reaction-diffusion system captures properties of cell polarity. *PLoS Comp. Biol.*, 3:e108, 2007.

[114] D. St Johnston and J. Ahringer. Cell polarity in eggs and epithelia: parallels and diversity. *Cell*, 141:757, 2010.

[115] B. J. Thompson. Cell polarity: models and mechanisms from yeast, worms and flies. *Development*, 140:13, 2013.

[116] J. S. Bois, F. Jülicher, and S. W. Grill. Pattern formation in active fluids. *Phys. Rev. Lett.*, 106:028103, 2011.

[117] S. Alonso and M. Bär. Phase separation and bistability in a three-dimensional model for protein domain formation at biomembranes. *Phys. Biol.*, 7:046012, 2010.

[118] E. L. Elson, E. Fried, J. E. Dolbow, and G. M. Genin. Phase separation in biological membranes: integration of theory and experimen. *Annu. Rev. Biophys.*, 39:207, 2010.

[119] M. J. Tindall, P. K. Maini, S. L. Porter, and J. P. Armitage. Overview of mathematical approaches used to model bacterial chemotaxis II: Bacterial populations. *Bull. Math. Biol.*, 70:1570, 2008.

[120] M. Meyer, L. Schimansky-Geier, and P. Romanczuk. Active Brownian agents with concentration-dependent chemotactic sensitivity. *Phys. Rev. E*, 89:022711, 2014.

[121] B. Liebchen, D. Marenduzzo, I. Pagonabarraga, and M. E. Cates. Clustering and pattern formation in chemorepulsive active colloids. *Phys. Rev. Lett.*, 115:258301, 2015.

[122] J. Stenhammar, R. Wittkowski, D. Marenduzzo, and M. E. Cates. Activity-induced phase separation of self-assembly in mixtures of active and passive particles. *Phys. Rev. Lett.*, 114:018301, 2015.

[123] A. Y. Grosberg and J.-F. Joanny. Nonequilibrium statistical mechanics of mixtures of particles in contact with different thermostats. *Phys. Rev. E*, 92:032118, 2015.

[124] J. Smrek and K. Kremer. Small activity differences drive phase separation in active-passive polymer mixtures. *Phys. Rev. Lett.*, 118:098002, 2017.

[125] I. Theurkauff, C. Cottin-Bizonne, J. Palacci, C. Ybert, and L. Bocquet. Dynamic clustering in active colloidal suspensions with chemical signaling. *Phys. Rev. Lett.*, 108:268303, 2012.

[126] J. Palacci, S. Sacanna, A. P. Steinberg, D. J. Pine, and P. M. Chaikin. Living crystals of light-activated colloidal surfers. *Science*, 339:936, 2013.

[127] I. Buttinoni, J. Bialké, F. Kümmel, H. Löwen, C. Bechinger, and T. Speck. Dynamical clustering and phase separation in suspensions of self-propelled colloidal particles. *Phys. Rev. Lett.*, 110:238301, 2013.

[128] Q.-X. Liu, A. Doelman, V. Rottschäfer, M. de Jager, P. M. Herman, M. Rietkerk, and J. van de Koppel. Phase separation explains a new class of self-organized spatial patterns in ecological systems. *Proc. Natl. Acad. Sci. USA*, 110:11905, 2013.

[129] P. Fromherz and B. Kaiser. Stationary patterns in membranes by nonlinear diffusion of ion channels. *EPL*, 15:313, 1991.

[130] A. Jilkine and L. Edelstein-Keshet. A comparison of mathematical models for polarization of single eukaryotic cells in response to guided cues. *PLoS Comput. Biol.*, 7:e1001121, 2011.

[131] A. Mogilner, J. Allard, and R. Wollman. Cell polarity: Quantitative modeling as a tool in cell biology. *Science*, 336:175, 2012.

[132] P. K. Trong, E. M. Nicola, N. W. Goehring, K. V. Kumar, and S. W. Grill. Parameter-space topology of models for cell polarity. *New J. Phys.*, 16:065009, 2014.

[133] V. L. Ginzburg and L. D. Landau. On the theory of superconductivity. *JETP*, 20:1064, 1950.

[134] L. A. Segel. Distant side-walls cause slow amplitude modulation of cellular convection. *J. Fluid Mech.*, 38:203, 1969.

[135] B. Rubinstein, B. D. Slaughter, and R. Li. Weakly nonlinear analysis of symmetry breaking in cell polarity models. *Phys. Biol.*, 9:045006, 2012.

[136] S. Etienne-Manneville and A. Hall. Rho GTPases in cell biology. *Nature*, 420:629, 2002.

[137] R. Meili and R. A. Firtel. Two poles and a compass. *Cell*, 114:153, 2003.

[138] E. D. Siggia. Late stages of spinodal decomposition in binary mixtures. *Phys. Rev. A*, 20:595, 1979.

[139] J. D. Gross. Developmental decisions in Dictyostelium discoideum. *Microbiol. Rev.*, 58:330, 1994.

[140] L. Wolpert. *Principles of Development*. Oxford Univ. Press, Oxford, 2002.

[141] P. Schaap. Evolutionary crossroads in developmental biology: Dictyostelium discoideum. *Development*, 138:387, 2011.

[142] M. Eisenbach. *Chemotaxis*. Imperial College Press, London, 2004.

[143] E. F. Keller and L. A. Segel. Initiation of slime mold aggregation viewed as an instability. *J. Theor. Biol.*, 26:399, 1970.

[144] E. F. Keller and L. A. Segel. Model for chemotaxis. *J. Theor. Biol.*, 30:225, 1971.

[145] T. Hillen and K. J. Painter. A user's guide to PDE models for chemotaxis. *J. Math. Biol.*, 58:183, 2009.

[146] L. Rapp. *Effects of confinement and conservation in nature's toolbox of pattern formation*. PhD thesis, Universität Bayreuth, 2019.

[147] Y. Fily and M. C. Marchetti. Athermal phase separation of self-propelled particles with no alignment. *Phys. Rev. Lett.*, 108:235702, 2012.

[148] F. D. C. Farrell, M. C. Marchetti, D. Marenduzzo, and J. Tailleur. Pattern formation in self-propelled particles with density-dependent motility. *Phys. Rev. Lett.*, 108:248101, 2012.

[149] G. S. Redner, M. F. Hagan, and A. Baskaran. Structure and dynamics of a phase-separating active colloidal fluid. *Phys. Rev. Lett.*, 110:055701, 2013.

[150] M. E. Cates and J. Tailleur. Motility-induced phase separation. *Annu. Rev. Condens. Matter Phys.*, 6:219, 2015.

[151] C. Liu, X. Fu, L. Liu, X. Ren, C. K. L. Chau, S. Li, L. Xiang, H. Zeng, G. Chen, L.-H. Tang, P. Lenz, X. Cui, W. Huang, T. Hwa, and J.-D. Huang. Sequential estabishment of stripe patterns in an expanding cell population. *Science*, 334:238, 2011.

[152] X. Fu, L.-H. Tang, C. Liu, J.-D. Huang, T. Hwa, and P. Lenz. Stripe formation in bacterial systems with density-suppressed motility. *Phys. Rev. Lett.*, 108:198102, 2012.

[153] A. Walther and A. H. E. Müller. Janus particles: Synthesis, self-assembly, physical properties, and applications. *Chem. Rev.*, 113:5194, 2013.

[154] J. Bialké, H. Löwen, and T. Speck. Microscopic theory for phase separation of self-propelled repulsive disks. *EPL*, 103:30008, 2013.

[155] T. Speck, J. Bialké, A. M. Menzel, and H. Löwen. Effective Cahn-Hilliard equation for the phase separation of active Brownian particles. *Phys. Rev. Lett.*, 112:218304, 2014.

[156] T. Speck, A. M. Menzel, J. Bialké, and H. Löwen. Dynamical mean-field theory and weakly non-linear analysis for the phase separation of active Brownian particles. *J. Chem. Phys.*, 142:224109, 2015.

[157] J. Stenhammar, A. Tiribocchi, R. J. Allen, D. Marenduzzo, and M. E. Cates. Continuum theory of phase separation kinetics for active Brownian particles. *Phys. Rev. Lett.*, 111:145702, 2013.

[158] R. Wittkowski, A. Tiribocchi, J. Stenhammar, R.J. Allen, D. Marenduzzo, and M. E. Cates. Scalar ϕ^4 field theory for active-particle phase separation. *Nat. Commun.*, 5:4351, 2014.

[159] E. Tjhung, C. Nardini, and M. E. Cates. Cluster phases and bubbly phase separation in active fluids: Reversal of the Ostwald process. *Phys. Rev. X*, 8:031080, 2018.

[160] A. P. Solon, J. Stenhammar, M. E. Cates, Y. Kafri, and J. Tailleur. Generalized thermodynamics of phase equilibria in scalar active matter. *Phys. Rev. E*, 97:020602(R), 2018.

[161] J. Moacanin, G. Holden, and N. W. Tschoegl, editors. *Block copolymers*, volume 26 of *Polymer symposia*. J. Poly. Sci., Part C, 1969.

[162] L. Leibler. Theory of microphase separation in block copolymers. *Macromolecules*, 13:1602, 1980.

[163] J. Stenhammar, D. Marenduzzo, R.J. Allen, and M. E. Cates. Phase behaviour of active Brownian particles: the role of dimensionality. *Soft Matter*, 10:1489, 2014.

2 Publications

2.1 List of included publications

[*pub1*] *Size matters for nonlinear (protein) wave patterns*
F. Bergmann, L. Rapp, and W. Zimmermann,
New. J. Phys. **20**, 072001 (2018)

[*pub2*] *Pattern orientation in finite domains without boundaries*
L. Rapp, F. Bergmann, and W. Zimmermann,
EPL **113**, 28006 (2016)

[*pub3*] *Reflection of nonlinear wave patterns in finite domains without boundaries*
F. Bergmann and W. Zimmermann,
submitted to PRE (06/2019)

[*pub4*] *Active phase separation: A universal approach*
F. Bergmann, L. Rapp, and W. Zimmermann,
Phys. Rev. E **98**, 020603(R) (2018)

[*pub5*] *On system-spanning demixing properties of cell polarization*
F. Bergmann and W. Zimmermann,
PLoS ONE 14(6): e0218328 (2019)

[*pub6*] *Systematic extension of the Cahn-Hilliard model for motility-induced phase separation*
L. Rapp, F. Bergmann, and W. Zimmermann,
Eur. Phys. J. E **42**: 57 (2019)

2.2 Individual contributions of the authors

The following overview breaks down the contributions of the individual authors to the publications listed in Sec. 2.1. The following abbreviations are used:
FB = Fabian Bergmann, LR = Lisa Rapp, WZ = Walter Zimmermann.

- Contributions to [*pub1*]:
  FB performed numerical simulations of the complex Swift-Hohenberg model, the extended Brusselator and the Min Protein model. FB developed concepts for the analytical calculations. LR performed the linear stability analysis. All authors designed the project, contributed to the discussion and interpretation of the results and co-wrote the manuscript.

- Contributions to [*pub2*]:
  FB developed and implemented the expansion of the control parameter drop. LR performed numerical simulations of the Brusselator model All authors designed the project, contributed to the discussion and interpretation of the results and co-wrote the manuscript.

- Contributions to [*pub3*]:
  FB developed and implemented the expansion of the control parameter drop. FB performed numerical simulations of the complex Swift-Hohenberg model. FB did most of the interpretation of the results and the writing of the manuscript. WZ supervised the research project, contributed to the interpretation of the results and the writing of the manuscript.

- Contributions to [*pub4*]:
  All authors designed the project, authors contributed to the development of the perturbative scheme and interpretations of the results. FB performed analytical calculations and numerical simulations for the cell polarization model. LR performed analytical calculations and numerical simulations for the model of chemotactically communicating cells. All authors designed the project, contributed to the discussion and interpretation of the results and co-wrote the manuscript.

- Contributions to [*pub5*]:
  FB performed the analytical calculation and the numerical simulations of the polarization model. Both authors contributed to the discussion and interpretation of the results and co-wrote the manuscript.

- Contributions to [*pub6*]:
  All authors contributed to the extension of the perturbative scheme and interpretations of the results. LR and FB both performed analytical calculations.

LR performed numerical simulations. LR wrote most of the manuscript, FB and WZ participated in the writing process.

2.3 List of talks and posters

During my doctorate i presented the results and findings of this thesis at the following conferences, workshops and summer schools:

- WEH Physics School: "Model systems for understanding biological processes", Febuary 22-27, 2015 in Bad Honnef;
  Poster: "Traveling waves: Orientation and reflection effects induced by sudden control parameter changes"

- DPG Spring Meeting, March 15-20, 2015 in Berlin;
  Poster: "Traveling waves: Orientational and reflection effects induced by sudden control parameter changes"

- DPG Spring Meeting, March 06-11, 2016 in Regensburg;
  Talk: "Reflection of Nonlinear Traveling Waves in Finite Domains without Boundaries"

- WEH Seminar "Patterns in Nature – Functions, Variations and Control" October 17-21, 2016 in Bayreuth;
  Poster: "Reflection of nonlinear traveling waves without boundaries"

- DPG Spring Meeting, March 19-24, 2017 in Dresden;
  Talk: "Size matters for Nonlinear Waves and Min Protein Patterns"

- DPG Spring Meeting, March 11-16, 2018 in Berlin;
  Talk: "Active phase separation – a universal approach"

- Conference: "Self-Organization in Active Matter: From Colloids to Cells" October 01-06, 2018 in Erice;
  Talk: "Active phase separation – a universal approach"

- Workshop: "Advances in Pattern Formation: New Questions Motivated by Applications" Febuary 18-21, 2019 in Sde Boquer;
  Poster: "Systematic extension of the Cahn-Hilliard model for MIPS"

- DPG Spring Meeting, March 31- April 05, 2019 in Regensburg;
  Talk: "Systematic extension of the Cahn-Hilliard model for MIPS"

Publication 1

Size matters for nonlinear (protein) wave patterns

F. Bergmann, L. Rapp, and W. Zimmermann

New J. Phys. **20**, 072001 (2018)
(DOI: 10.1088/1367-2630/aad457)

Reprinted without changes under CC-BY 3.0

New Journal of Physics
The open access journal at the forefront of physics

Deutsche Physikalische Gesellschaft DPG
IOP Institute of Physics

Published in partnership with: Deutsche Physikalische Gesellschaft and the Institute of Physics

OPEN ACCESS

RECEIVED
19 June 2018

REVISED
5 July 2018

ACCEPTED FOR PUBLICATION
18 July 2018

PUBLISHED
27 July 2018

Original content from this work may be used under the terms of the Creative Commons Attribution 3.0 licence.

Any further distribution of this work must maintain attribution to the author(s) and the title of the work, journal citation and DOI.

FAST TRACK COMMUNICATION

Size matters for nonlinear (protein) wave patterns

Fabian Bergmann[1], **Lisa Rapp**[1] **and Walter Zimmermann**

Theoretische Physik I, Universität Bayreuth, D-95440 Bayreuth, Germany

[1] Contributed equally to this work.

E-mail: walter.zimmermann@uni-bayreuth.de

Keywords: pattern formation, biological physics, reaction–diffusion, nonlinear waves

Supplementary material for this article is available online

Abstract

Pattern formation and selection are fundamental, omnipresent principles in nature—from small cells up to geological scales. In *E. coli* bacteria, for example, self-organized pole-to-pole oscillations of Min proteins—resembling a short standing wave—ensure correct positioning of the cell division site. The same biochemical reaction leads to traveling protein waves on extended membranes in *in vitro* experiments. Are these seemingly contradictory observations of system-spanning importance? We show that a transition of nonlinear traveling wave patterns to reflection-induced standing waves in short systems is a generic and robust phenomenon. It results from a competition between two basic phenomena in pattern formation theory. We confirm the generic findings for the cell-biological Min reaction and for a chemical reaction–diffusion system. These standing waves show bistability and adapt to varying system lengths similar as pole-to-pole oscillations in growing *E. coli*. Our generic results highlight key functions of universal principles for pattern formation in nature.

1. Introduction

A variety of fascinating patterns emerges spontaneously in a wealth of living or inanimate driven systems [1–13]. The esthetic appeal of these patterns is immediately apparent to all observers [1]. But universal principles of patterns and their importance in nature also attract researchers from many disciplines. They explore, for instance, the important functions patterns fulfill: self-organized patterns in biology guide size sensing [6], positioning of protein clusters [7], self-driven morphogenesis [8] and communication between species [10]. They furthermore enhance heat transport in fluid systems [3, 11] and are the basis of successful survival strategies for vegetation in water-limited systems [12–14].

Patterns include both stationary spatial structures such as stripes or hexagons, and dynamic structures like traveling waves [1–4]. Traveling waves occur in such different and prominent systems as thermally driven fluid convection [3, 15–18], electroconvection in nematic liquid crystals [19, 20] or the biochemical Min protein reaction on extended membranes [21, 22]. As these examples show, patterns emerge in diverse systems and are driven by very different mechanisms. Nevertheless, once stripes, hexagons or traveling waves have evolved, they often have certain universal properties described by pattern formation theory [2–4, 12].

In nature, patterns often evolve in the presence of domain boundaries—be it the walls of a convection cell, the finite size of a petri dish or the membrane enclosing the cytosol of a biological cell. These boundaries have a strong influence on the process of pattern formation. Stripe patterns, e.g., respond to system boundaries by adjusting their stripe orientation or selecting specific wavelengths [3, 23–25]. System boundaries in general break symmetries. Spatially varying parameters break them, too, and thus have similar effects [26–28]. The response of stationary periodic patterns to such symmetry breaking effects is broadly similiar in different systems, i.e. independent of system details [3, 23, 25]. Traveling waves near boundaries show similar fascinating spatio-temporal behavior [15, 16, 29, 30]. However, the effects of strong confinement on nonlinear wave patterns have not yet been thoroughly examined.

© 2018 The Author(s). Published by IOP Publishing Ltd on behalf of Deutsche Physikalische Gesellschaft

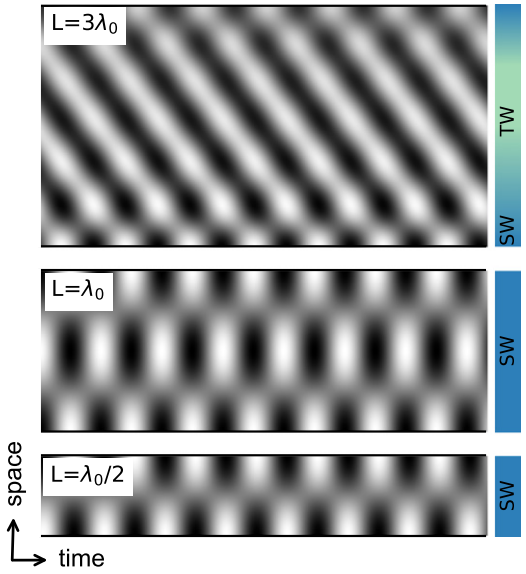

Figure 1. Strong confinement leads to significantly different wave solutions depending on the system length. (Top) Modulated traveling wave (TW) for $L = 3\lambda_0$, (Middle) two-node standing wave (SW) for $L = \lambda_0$, (Bottom) one-node standing wave for $L = \lambda_0/2$. Simulations of equation (1) with no-flux boundaries, represented in space-time plots. Shown is the real part of the complex field $u(x, t)$ for the parameters $\varepsilon = 0.5, a = -0.8, \xi_0 = 1, b = 0, q_0 = 1, f = 0.5, \gamma = 1, c = 0.5$.

In this work, we show that nonlinear traveling waves inevitably change into reflection-induced standing waves in sufficiently short, confined systems. Since this generic phenomenon relies on basic universal principles of pattern formation, we explore it at first within a minimal model for nonlinear traveling waves. The resulting system-spanning properties can then be transferred to related phenomena in nature: in the Min system, e.g., traveling waves form by coordinated attachment and detachment of Min proteins from the membrane. This protein system originates from *E. coli* bacteria where it plays an important role in the cell division process [31–33]: inside the rod-shaped *E. coli* bacteria, oscillating proteins shuttle between the two cell poles. Thereby, they ensure the positioning of the cell division site at the cell center. In *in vitro* experiments on the other hand, the same biochemical reaction leads to traveling waves on large extended membranes [21, 22]. A deeper understanding of generic properties of nonlinear waves in confinement will help to reconcile these seemingly contradictory observations.

2. Transition to reflection-induced standing waves in short systems

We first analyze the transition from nonlinear traveling waves in extended systems to reflection-induced standing waves in strongly confined systems using a generic model. 'Strong confinement' refers to short system lengths in the order of the preferred wavelength of the traveling wave. The model we use is the complex Swift–Hohenberg (CSH) model [4, 34–36],

$$\partial_t u(x, t) = (\varepsilon + \mathrm{i}a)u - \xi_0^2(1 + \mathrm{i}b)(q_0^2 + \partial_x^2)^2 u + \mathrm{i}f\partial_x^2 u - \gamma(1 + \mathrm{i}c)|u|^2 u, \tag{1}$$

for the complex scalar field $u(x, t)$ in one spatial dimension. In extended systems and for $\varepsilon > 0$, this model shows traveling waves with a preferred wavelength $\lambda_0 = 2\pi/q_0$ over a wide range of parameters. We measure the system length L in units of λ_0 since it represents an intrinsic length scale of the problem.

Simulations of equation (1) with no-flux boundary conditions (see appendix A for details) for three different system lengths lead to the results shown in figure 1: depending on the system length, we get three significantly different wave solutions.

In moderately short systems ($L = 3\lambda_0$, top), we find a traveling wave pattern in the center (bulk) of the system. This resembles the traveling wave patterns that occur for the CSH model in large, quasi-unconfined systems. Two traveling wave directions, described by $u_R(x - \omega t)$ (traveling to the right) and $u_L(x + \omega t)$ (traveling to the left), are equally likely in extended pattern forming systems. In contrast to, e.g., light or sound waves, however, traveling waves in pattern forming systems are nonlinear. While light or sound waves are thus superimposable, two counter-propagating nonlinear waves compete with each other: one of the traveling wave directions is spontaneously selected, while the other is suppressed [3, 29]. But their confinement in finite systems introduces an additional effect: traveling waves are reflected at the boundaries of a finite system. The boundary conditions apply to the whole field $u(x, t)$ in equation (1), i.e. the incoming and reflected waves together.

Therefore, the sum $u_R + u_L$, has to match them at the system borders. This boundary coupling forces the incoming and reflected waves into coexistence in a finite neighborhood of the boundary. The resulting superposition of both wave directions leads to standing wave patterns. Further away in the bulk the nonlinear competition between both wave directions dominates and the reflected wave is damped by the predominant incoming traveling wave. The largest system in figure 1 (top) shows the interplay between both bulk and boundary effects. Reflection effects dominate very close to the top and bottom boundaries of the system. There, the incoming and reflected wave form a local standing wave. The extent of this standing wave depends on the distance ε from threshold and increases by decreasing ε. In the bulk region, however, wave competition prevails —the pattern resembles a traveling wave. By decreasing the system length L, the boundaries move closer together, i.e. the fraction of the system with significant superposition of incoming and reflected waves increases. Therefore, the boundary-induced reflection becomes more and more important. For sufficiently short systems —shorter than a critical length L_c—the reflection effect predominates the nonlinear competition in the whole system. As a result, standing waves become inevitable. Note that these standing waves are reflection-induced. In principle, standing wave solutions can be inherently stable. However, this is not the case here: in the CSH model, standing waves in extended systems are always unstable. Thus, the standing waves we find here are a direct consequence of the confinement. While this novel, reflection-induced transition from traveling to standing waves is generic, the critical length L_c depends on the chosen parameters and is specific to each system. The middle and bottom panel in figure 1 show simulations for $L = \lambda_0$ and $L = \lambda_0/2$, respectively. Both system lengths are below L_c leading to standing wave patterns. In the standing wave regime, the system length influences the number of standing wave nodes. For $L = \lambda_0$ (figure 1, middle) and similar lengths, we find a two-node standing wave. If only about half of the preferred wavelength fits into the system (e.g. $L = \lambda_0/2$, figure 1 bottom), the standing wave has a single node in the system center.

3. Length adaptability and bistability of nonlinear standing waves

The discovered reflection-induced standing waves in strongly confined systems are further characterized by exploring their linear stability. For stationary stripe patterns it is well known that they are stable for different wavenumbers in a finite band width. The basis of this multistability is the so-called Eckhaus stability band [37, 38]. Both fluid experiments [39, 40] and numerical analysis of different systems [27, 41] confirmed multistability for stationary patterns (e.g. stripes) in extended systems. The Eckhaus stability band also exists for traveling waves in unconfined systems [4, 17, 42, 43]. Do the standing waves we find in strongly confined systems also show multistable behavior? Does the confinement influence the stability band compared to spatially extended systems?

An analytical approximation of a standing wave solution of equation (1) is given by

$$u(x,\, t) = F\mathrm{e}^{-\mathrm{i}\Omega t}[\mathrm{e}^{\mathrm{i}qx} + \mathrm{e}^{-\mathrm{i}qx}] = 2F\mathrm{e}^{-\mathrm{i}\Omega t}\cos(qx), \tag{2}$$

with amplitude F and frequency Ω,

$$F^2 = \frac{1}{3\gamma}[\varepsilon - \xi_0^2(q_0^2 - q^2)^2], \tag{3}$$

$$\Omega = \frac{1}{\tau_0}[-a + \xi_0^2 b(q_0^2 - q^2)^2 + fq^2 + 3\gamma c F^2]. \tag{4}$$

Due to the no-flux boundaries, the wavenumber q is connected to the system length L via $q = n\pi/L$, where $n = 1, 2, 3 \ldots$ is the number of nodes. This standing wave solution in equation (2) theoretically exists for $F^2 > 0$, i.e. for $\varepsilon > \xi_0^2(q_0^2 - q^2)^2$. In nature, e.g. in (bio)chemical reactions, the control parameter value, corresponding to ε in our model, is often fixed above the threshold of pattern formation. Then, standing waves only fulfill the aforementioned existence condition within a finite range of system lengths. Therefore standing waves with n nodes only exist in a certain length regime (existence band), located around $L = n\lambda_0/2$. In addition, existence ranges of standing waves with different numbers of nodes may overlap. Thus, for certain system lengths, multiple standing wave solutions (with different numbers of nodes) exist simultaneously. However, parameter ranges where patterns theoretically exist are not equivalent to the parameter ranges where they are stable. In fact, patterns are usually not stable throughout their whole existence range [3, 17, 27, 39–42]. By also analyzing the stability of standing waves, we thus identify the range in which to expect these solutions, especially in experiments (see SM is available online at stacks.iop.org/NJP/20/072001/mmedia for more details on the linear stability analysis).

Figure 2(a) shows the stability regions of standing wave solutions as a function of both system length L and the control parameter ε. For a given system length, standing waves with n nodes only exist for sufficiently large $\varepsilon > \xi_0^2(q_0^2 - (n\pi/L)^2)^2$. Below this threshold (black line in figure 2(a)) , the homogeneous solution $u = 0$ is stable and no pattern occurs. The stability range of standing waves with n nodes is located around $L = n\lambda_0/2$ at

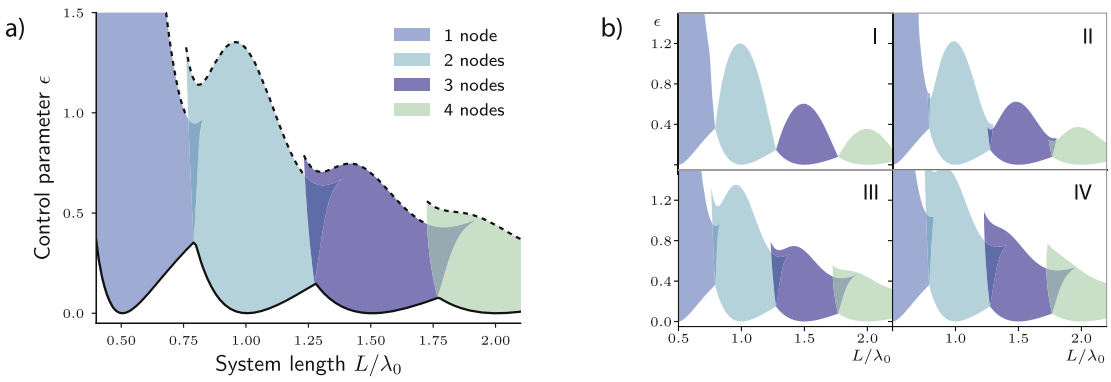

Figure 2. Stability and length adaptability of standing waves. (a) Stability regions of standing waves as a function of system length L and control parameter ε. Shaded regions indicate stable standing waves with $n = 1, 2, 3, 4$ nodes. Homogeneous solution is stable below solid black line and traveling wave patterns in the bulk above dashed lines. Parameters in equation (1): $a = 0, \xi_0 = 1, b = 0, q_0 = 1$, $f = 0.5, \gamma = 1, c = 0.5$. (b) Influence of the group velocity parameter f on the stability of standing waves solution in the CSH system. Parameters: $f = 0.0$ (I), 0.2 (II), 0.5 (III), 0.7 (IV), other parameters as in (a).

moderate values of ε. For $L = n\lambda_0/2$, the wavelength of the standing wave corresponds to the preferred wavelength λ_0 of the CSH model. For these 'optimal' system lengths, standing waves are stable over a large range of control parameter values. Nevertheless, we can deviate from these optimal lengths while still maintaining stable standing waves. This creates regions of stability in the ε-L-plane. These stability regions constitute the Eckhaus stability band for different number of nodes. We can now compare the width of the Eckhaus band to the width of the existence band for the standing waves. In extended systems, the waves are only stable in a subrange of their existence band. In contrast, in our confined systems close to the onset of pattern formation, the Eckhaus band spans the whole existence range (see figure 1 in SI). Additionally, adjacent stability regions may be large enough to overlap. In these cases, standing waves with both n and $n + 1$ nodes are stable. These overlapping stability regions therefore constitute areas of multistability. For large values of ε (above the dashed line in figure 2(a)), standing waves eventually lose stability. Simulations then show a transition to traveling wave patterns such as in figure 1 (top). The details of the stability regions also depend on the other parameters of the CSH model. Parameter f, e.g., which is connected to the group velocity of the waves, qualitatively changes the exact shape of the stability regions (figure 2(b)). As a result, the overlap between adjacent stability regions increases with increasing f. Other system parameters such as b or c only marginally change the stability of standing waves (figures S2 and S3) in confined systems. Importantly, however, the generic principle of a transition from traveling to standing waves in short systems remains qualitatively independent from system details.

Note that due to the shape of the stability regions, different scenarios are possible upon observing systems with increasing length: if we choose ε such that stability regions overlap, we expect direct transitions between standing waves with an increasing number of nodes (as seen in figure 1). Inside the overlap, there is bistability of standing waves with different numbers of nodes. Therefore, both types of standing waves are possible and the resulting pattern depends on initial conditions (see figure 3(a)). Notably, this provides the possibility for hysteresis. The transition from one to two nodes in a growing system, e.g., takes place at a different system length than the reverse transition in a shrinking system. For other values of ε, the different standing wave solutions are intersected by either the homogeneous solution (for small ε) or by traveling wave patterns (for larger ε, figures 3(b), (A)–(C)). In all cases, standing waves eventually lose stability for sufficiently large systems (after crossing the dashed line in figure 2(a)). For a fixed system length L, standing waves also loose their stability for sufficiently large ε (figures 3(b), (D)–(E)). These transitions to modulated traveling waves—both as a function of L and ε—take place in the form of supercritical (continuous) bifurcations (figure 3(c), see SM for details on how this was calculated).

4. Reflection-induced standing waves in models for a chemical reaction and the Min protein system

Minimal models such as the CSH model we study here for traveling waves are powerful tools to study system-spanning properties of self-organized patterns. System-specific models describing traveling waves are usually more complex than the CSH model. They are, e.g., often composed of several coupled nonlinear equations and/or include higher order nonlinearities (see e.g. [3, 21, 22, 44–49]). Moreover, traveling waves can occur far from the onset of pattern formation. Possible intricacies in these cases include secondary instabilities or anharmonic

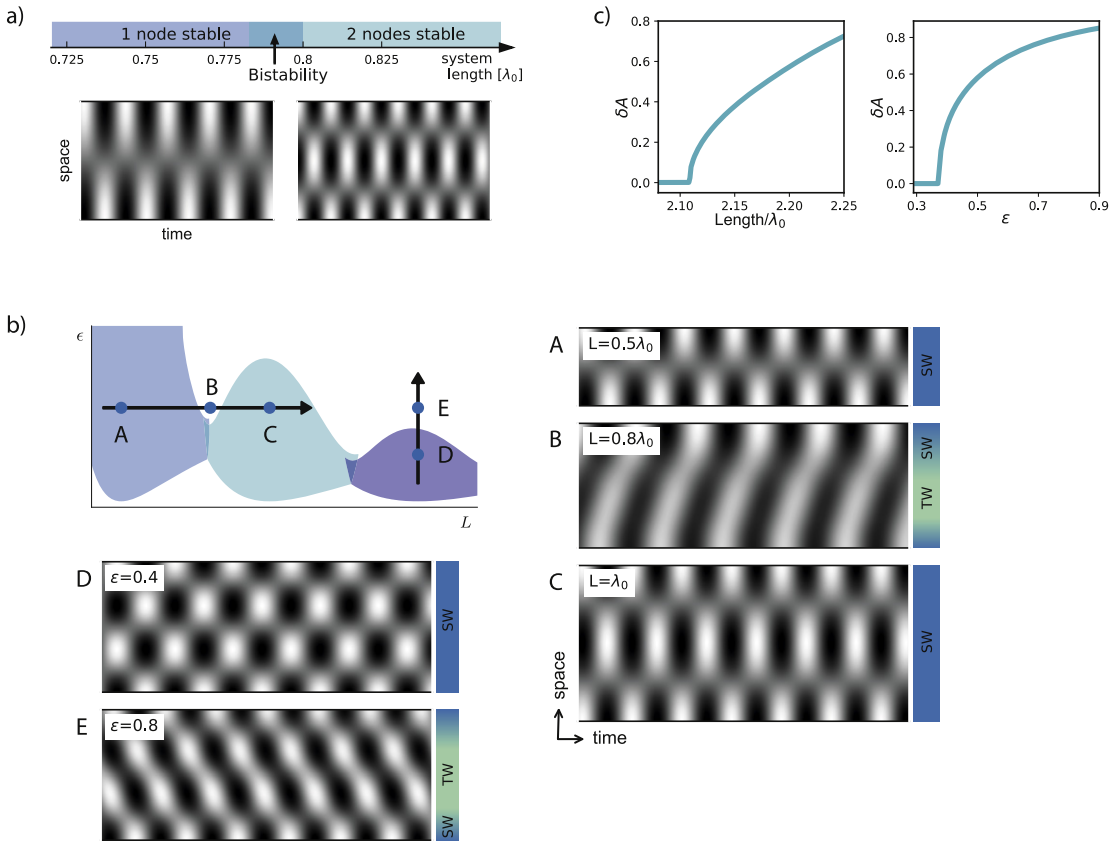

Figure 3. Scenarios for transitions between standing and traveling wave patterns. (a) Bistability of standing waves with 1 and 2 nodes due to overlapping stability regions. Depending on initial conditions, both a standing wave with one node (left) or two nodes (right) is possible for $L = 0.79\lambda_0$ and $\varepsilon = 0.55$. (b) Different scenarios are possible upon changing system parameters. For fixed $\varepsilon = 0.8$, we get 3 different solutions upon increasing the system length L: from a standing wave with one node (A, $L = 0.5\lambda_0$) to modulated traveling waves (B, $L = 0.8\lambda_0$) to 2-node standing wave (C, $L = \lambda_0$). For a fixed system length $L = 1.5\lambda_0$, there is a transition from a 3-node standing wave (D, $\varepsilon = 0.4$) to a modulated traveling wave (E, $\varepsilon = 0.8$). (c) Transitions from standing waves to modulated traveling waves are supercritical bifurcations as both a function of the system length L (left) and the control parameter ε: the amplitude of traveling waves increases continuously above the critical length L_c or the critical control parameter ε_c, respectively (see SM for more details). Additional system parameters for all simulations in this panel: $f = 0.2$, rest as given in figure 1.

wave profiles. Such effects can potentially overshadow the generic behavior of traveling waves under constraints discussed so far. Apart from these exceptions, however, even more complex scenarios often qualitatively follow generic principles extracted from minimal models. Thus, our results obtained from the generic CSH model help us to understand wave patterns in more complex systems.

We support this view by investigating the behavior of nonlinear traveling waves under confinement in two specific systems far from equilibrium. The first model describes the aforementioned Min protein oscillations in *E. coli* bacteria [21]. The second example is an extended Brusselator—a chemical reaction–diffusion model that forms traveling waves [49] (see appendices B and C for details on both models). As figures 4(a) and (b) show, the qualitative behavior of nonlinear waves in both of these models is very similar to the generic CSH model: in sufficiently strong confinement, traveling wave patterns inevitably change into reflection-induced standing waves. Depending on the system length, we also find standing wave patterns with different numbers of nodes. Note that both sets of simulations take place far beyond threshold. In this highly nonlinear regime the spatial dependence of the waves cannot be described by a single harmonic as in equation (2). Instead, they include higher harmonics—as seen in the Fourier spectra in figures 4(c) and (d).

Both models have a similar growth dispersion relation for perturbations of the homogeneous basic state as the CSH model—with a maximum at a finite wavenumber, while other modes are damped. Furthermore, the extended Brusselator shows a continuous bifurcation from the homogeneous state to traveling wave patterns—again, similar to the CSH model. On the basis of these common properties, the similar behavior of nonlinear waves in strong confinement were to be expected. Traveling waves in the Min model in figure 4(b) are even further from threshold and thus in the strongly nonlinear regime. Nevertheless, we find the same scenarios for the Min reaction as for the CSH model and the Brusselator. This further supports the generic nature of our predictions on reflection-induced standing waves.

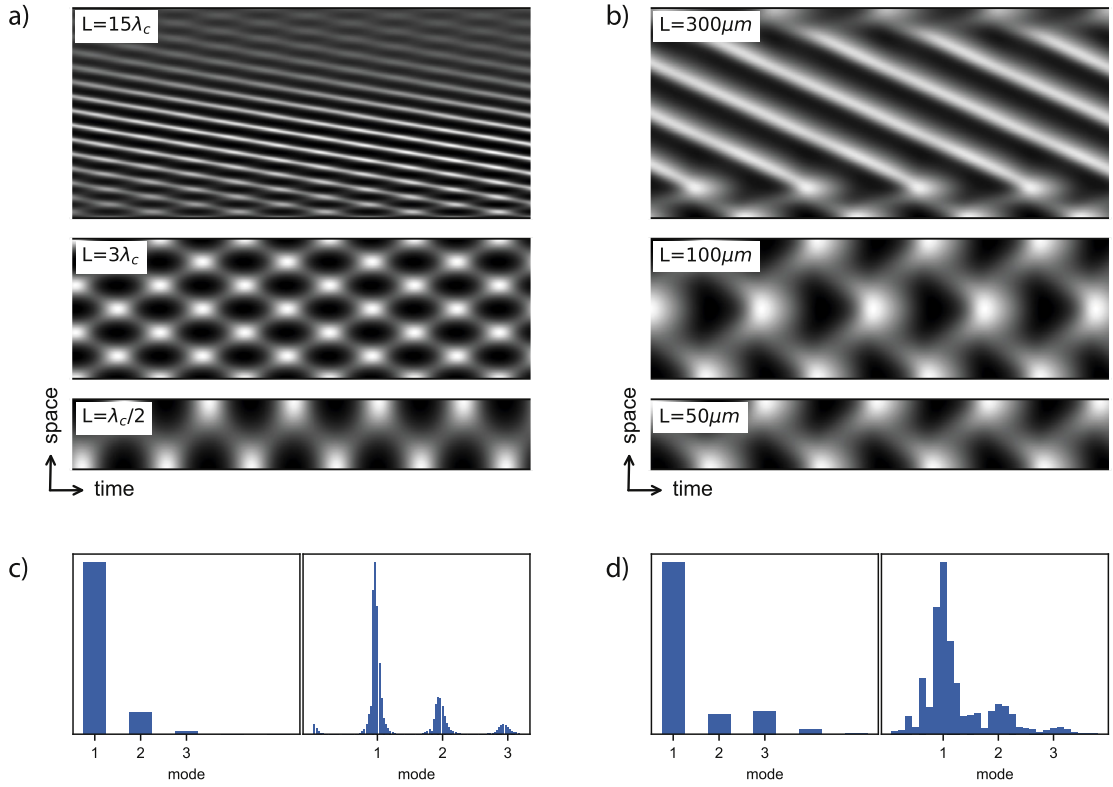

Figure 4. Waves in confinement in a Brusselator and Min model. (a) Effects of strong confinement on wave patterns in an extended Brusselator model, equations (2.1*a*)–(2.1*c*): (Top) modulated traveling wave for $L = 15\lambda_c$, (Middle) six-node standing wave for $L = 3\lambda_c$, (Bottom) one-node standing wave for $L = \lambda_c/2$. (Shown are space-time plots of the concentration field $u(x, t)$.) (b) Effects of strong confinement on wave patterns in simulations of the Min model, equations (3.1*a*)–(3.1*d*): (Top) Modulated traveling wave for $L = 300$ μm, (Middle) two-node standing wave for $L = 100$ μm, (Bottom) one-node standing wave for $L = 50$ μm. (Shown are space-time plots of the total MinD concentration.) (c) Power spectra for the simulations of the Brusselator model shown in (a) for $L = \lambda_c/2$ (left) and $L = 15\lambda_c$ (right). The mode $n = 1$ corresponds to the dominant mode in the Fourier spectrum, $n = 2, 3$ to multiples of the dominant mode. (d) Power spectra for the simulations of the Min model shown in (b) for $L = 50$ μm (left) and $L = 300$ μm (right).

Furthermore, our findings are not limited to no-flux boundary conditions. The reflection-induced transition to standing waves prevails for different boundary conditions such as fixed boundaries ($u_{|x=0} = u_{|x=L} = 0$). The only qualitative difference is the position of the standing wave nodes: they are shifted to the boundaries due to the vanishing fields at these points (see figure S4).

Nonlinear traveling waves in extended systems may be convectively unstable directly beyond threshold. This is also known as Benjamin–Feir instability [3, 4]. For the CSH model, this is the case in the parameter range $(b + f/4\xi_0^2 q_0^2)c > -1$. In this Benjamin–Feir unstable regime, spatio-temporally chaotic solutions are possible (above the transition to absolute instability). System size matters for spatio-temporal chaos as well: strong confinement and the related boundary-induced reflection can reestablish ordered standing waves (see figure S5).

5. Discussion

In our work we identified generic properties of nonlinear waves in very short systems, i.e. under strong spatial confinement. We found a universal and robust reflection-induced transition from traveling wave patterns in extended systems to standing waves in sufficiently short systems. Stability analysis shows that these standing waves can adapt to different system lengths. This corresponds to stability within a finite wavenumber band—a feature they share with stationary spatially periodic patterns or traveling waves [3, 17, 38–42]. They can also react to larger length variations by changing their number of nodes. We also find multistability of standing waves with different numbers of nodes in a system of the same length.

Our results obtained in terms of basic pattern formation theory show striking similarities to oscillating Min protein patterns. We hypothesize that basic generic properties of nonlinear wave patterns have a key function in the Min system. They may provide the missing link between pole-to-pole Min oscillations in short systems [31, 50–52] and traveling protein waves on extended membranes [21, 22]: the pole-to-pole oscillations in *E. coli* behave like standing waves originating from traveling waves confined to short systems. We also suggest that generic features of the reflection-induced standing waves such as length adaptability further contribute to the

regulation of cell division. This view is supported by experimental observations in the Min system: depending on bacteria length, the Min proteins also form standing waves with multiple nodes [31, 47, 53] or even traveling waves [47]. More importantly though, not only do living bacteria slightly differ in length, they also actively grow. To maintain accurate cell division at the cell center, the pole-to-pole oscillations must be robust over a range of cell sizes. The generic length adaptability of reflection-induced standing waves enables pole-to-pole oscillations in the Min system to adapt to the growing cell. In fact, *E. coli* maintain robust pole-to-pole oscillations even as they almost double in length prior to cell division. Continued cell growth to filamentous bacteria also allows for transitions between standing waves with different numbers of nodes or to traveling waves [33, 47, 53]. Even multistability of different wave patterns has recently been found in living *E. coli* [51].

Due to their generic nature, we expect our findings to be independent of system details. Our simulations of a Min protein model and an extended Brusselator substantiate this claim. While we analyzed one-dimensional systems in this work, we believe the basic principles also apply to two or three spatial dimensions: in sufficiently small multidimensional systems the boundary reflection of traveling waves along the long axis will likely overrule the bulk competition between counter-propagating traveling waves. Thus, system borders force them into reflection-induced standing waves—with slight system-specific modifications. Fluid experiments [17, 30] or oscillating chemical reactions guided by recent models as in [48, 49] are further suitable candidates to verify our results. Pattern formation theory applied to stationary 2d patterns recently provided important insights into pattern orientation with respect to spatial inhomogeneities or confinement [28, 54]. A combination of these approaches with our analysis of nonlinear traveling waves in confined systems is very promising. It may reveal further generic properties of nonlinear traveling waves and, e.g., provide additional guidance for experiments in 2d Min systems [50, 52]. This is particularly interesting for designing bottom-up approaches in synthetic biology to reconstitute cells [52]. In this context, our robust rules about nonlinear (protein) waves may present another puzzle piece to understand how nature controls crucial steps of life.

Acknowledgments

Support by the Elite Study Program Biological Physics is gratefully acknowledged.

Appendix A. Simulation methods

We solve the CSH model as well as the models for the Min oscillations and the chemical reactions below numerically by using a pseudo-spectral method with a semi-implicit time step (implicit Euler for the linear part of the equation, explicit Euler for the nonlinearities) (66). We calculate all spatial derivatives by transformation to a suitable function space depending on the boundary conditions. We use Fourier representations of the fields for periodic boundaries (i.e. in case of the CSH model $u|_{x=0} = u|_{x=L}$), a cosine transform for no-flux boundaries ($\partial_x u|_{x=0,L} = 0$) and a sine transform for vanishing fields at the boundary ($u|_{x=0,L} = 0$), where L is the system length.

Appendix B. Oscillating chemical reaction

As a model for a pattern forming chemical reaction, we use an extended Brusselator model as proposed by Yang *et al* [49]. The Brusselator is a well-known prototype for reaction–diffusion systems. Typically, this system is a two-component activator-inhibitor model with a bifurcation to Turing patterns or homogenous Hopf oscillations. The model by Yang *et al* extends the Brusselator by a third component. The dynamics of the three concentration fields u, v and w are given by:

$$\partial_t u = D_u \partial_x^2 u + a - (b+1)u + u^2 v - cu + dw, \tag{2.1a}$$

$$\partial_t v = D_v \partial_x^2 v + bu - u^2 v, \tag{2.1b}$$

$$\partial_t w = D_w \partial_x^2 w + cu - dw. \tag{2.1c}$$

We choose $a = 0.8, c = 2, d = 1, D_u = 0.01, D_v = 0$ and $D_w = 1$. We consider b the control parameter of the system. The homogeneous solution ($u_h = a, v_h = b/a, w_h = ac/d$) becomes unstable towards traveling waves at the critical value $b_c = 3.076$. The intrinsic wavelength of the traveling wave pattern above threshold is $\lambda_c \approx 9.5$. We perform our simulations close to pattern onset, for $b = b_c(1+\varepsilon)$ where $\varepsilon = 0.005$. The onset of the Turing instability (i.e. of stationary periodic patterns) tends to infinity for $D_v \to 0$. By choosing $D_v = 0$, we thereby eliminate any competition between traveling waves and Turing structures.

Appendix C. Min oscillation model

As a representative model for the Min oscillations shown in figure 4, we consider the model given by equations (3.1*a*)–(3.1*d*) as proposed by Loose *et al* [22] (see also equations [1]–[4] in their supplementary information). This model describes the dynamics of both MinD and MinE in the cytosol (c_D and c_E, respectively), the MinD concentration on the membrane c_d and the concentration of MinD/MinE complexes on the membrane c_{de}:

$$\partial_t c_D = D_D \partial_x^2 c_D + \omega_{de} c_{de} - c_D(\omega_D + \omega_{dD} c_d), \tag{3.1a}$$

$$\partial_t c_E = D_E \partial_x^2 c_E + \omega_{de} c_{de} - c_E c_d(\omega_E + \omega_{eE} c_{de}^2), \tag{3.1b}$$

$$\partial_t c_d = D_d \partial_x^2 c_d + c_D(\omega_D + \omega_{dD} c_d) - c_E c_d(\omega_E + \omega_{eE} c_{de}^2), \tag{3.1c}$$

$$\partial_t c_{de} = D_{de} \partial_x^2 c_{de} + c_E c_d(\omega_E + \omega_{eE} c_{de}^2) - \omega_{de} c_{de}. \tag{3.1d}$$

For the simulation shown in figure 4 we choose the parameters as suggested in [22]: $D_D = D_E = 60\ \mu\text{m}^2\ \text{s}^{-1}$, $D_d = 1.2\ \mu\text{m}^2\ \text{s}^{-1}$, $D_{de} = 0.4\ \mu\text{m}^2\ \text{s}^{-1}$, $\omega_{de} = 0.029\ \text{s}^{-1}$, $\omega_D = 2.9 \cdot 10^{-4}\text{s}^{-1}$, $\omega_{dD} = 4.8 \cdot 10^{-8}\mu\text{m}^2\ \text{s}^{-1}$, $\omega_E = 1.9 \cdot 10^{-9}\mu\text{m}^2\ \text{s}^{-1}$, $\omega_{eE} = 2.1 \cdot 10^{-20}\mu\text{m}^6\ \text{s}^{-1}$. We choose a total MinD concentration of $c_{D,\text{tot}} = c_D + c_d + c_{de} = 3.6 \cdot 10^6 \mu\text{m}^{-2}$, and a total MinE concentration of $c_{E,\text{tot}} = c_E + c_e + c_{de} = 5.8 \cdot 10^6 \mu\text{m}^{-2}$. In large, quasi-unconfined systems this leads to traveling waves with a typical wavelength $\lambda_{\text{min}} \approx 71\ \mu\text{m}$.

References

[1] Ball P 1998 *The Self-Made Tapestry: Pattern Formation in Nature* (Oxford: Oxford University Press)
[2] Cross M C and Greenside H 2009 *Pattern Formation and Dynamics in Nonequilibrium Systems* (Cambridge: Cambridge University Press)
[3] Cross M C and Hohenberg P C 1993 Pattern formation outside of equilibrium *Rev. Mod. Phys.* **65** 851
[4] Aranson I and Kramer L 2002 The world of the complex Ginzburg–Landau equation *Rev. Mod. Phys.* **74** 99
[5] Kondo S and Miura T 2010 Reaction–diffusion model as a framework for unterstanding biological pattern formation *Science* **329** 1616
[6] Lander A D 2011 Pattern, growth, and control *Cell* **144** 955
[7] Murray S M and Sourjik V 2017 Self-organization and positioning of bacterial protein clusters *Nat. Phys.* **13** 1006
[8] Sasai Y 2013 Cytosystems dynamics in self-organization of tissue architecture *Nature* **493** 318
[9] Kondo S and Asal R 1995 A reaction–diffusion wave on the skin of the marine angelfish Pomacanthus *Nature* **376** 786
[10] Singh A P and Nüsslein-Volhard C 2015 Zebrafish stripes as a model for vertebrate colour pattern formation *Curr. Biol.* **25** R81
[11] Lappa M 2009 *Thermal Convection: Patterns, Evolution and Stability* (New York: Wiley)
[12] Meron E 2015 *Nonlinear Physics of Ecosystems* (Boca Raton, FL: CRC Press)
[13] Meron E 2012 Pattern-formation approach to modelling spatially extended ecosystems *Ecol. Modelling* **234** 70
[14] Getzin S, Yizhaq H, Bell B, Erickson T E, Postle A, Katra I, Tzuk O, Zelnik Y R, Wiegand K and Meron E 2016 Discovery of fairy circles in australia supports self-organization theory *Proc. Natl Acad. Sci. USA* **113** 3551
[15] Moses E, Fineberg J and Steinberg V 1987 Multistability and confined traveling-wave patterns in a convecting binary mixture *Phys. Rev.* A **35** 2757
[16] Heinrichs R, Ahlers G and Cannell D S 1987 Traveling waves and spatial variation in the convection of a binary mixture *Phys. Rev.* A **35** 2761
[17] Kolodner P 1992 Extended states of nonlinear traveling-wave convection. I. The Eckhaus instability *Phys. Rev.* A **46** 6431
[18] Schöpf W and Zimmermann W 1993 Convection in binary fluids: amplitude equations, codimension-2 bifurcation, and thermal fluctuations *Phys. Rev.* E **47** 1739
[19] Rehberg I, Rasenat S, Fineberg J, de la Torre Juárez M and Steinberg V 1988 Temporal modulation of traveling waves *Phys. Rev. Lett.* **61** 2449
[20] Kramer L and Pesch W 1995 Convection instabilities in nematic liquid crystals *Annu. Rev. Fluid Mech.* **27** 515
[21] Loose M, Fischer-Friedrich E, Ries J, Kruse K and Schwille P 2008 Spatial regulators for bacterial cell division self-organize into surface waves *in vitro Science* **320** 789
[22] Schweizer J, Loose M, Bonny M, Kruse K, Mönch I and Schwille P 2012 Geometry sensing by self-organized protein patterns *Proc. Natl Acad. Sci. USA* **109** 15283
[23] Cross M C 1982 Boundary conditions on the envelope function of convective rolls close to onset *Phys. Fluids* **25** 936
[24] Kramer L and Hohenberg P C 1984 Effects of boundaries on periodic structures *Physica* D **13** 352
[25] Greenside H S and Coughran W M 1984 Nonlinear pattern formation near the onset of Rayleigh-Bénard convection *Phys. Rev.* A **30** 398
[26] Kramer L, Ben-Jacob E, Brand H and Cross M C 1982 Wavelength selection in systems far from equilibrium *Phys. Rev. Lett.* **49** 1891
[27] Riecke H and Paap H G 1986 Stability and wave-vector restriction of axisymmetric Taylor vortex flow *Phys. Rev.* A **33** 547
[28] Rapp L, Bergmann F and Zimmermann W 2016 Pattern orientation in finite domains without boundaries *Europhys. Lett.* **113** 28006
[29] Cross M C 1988 Structure of nonlinear traveling-wave states in finite geometries *Phys. Rev.* A **38** 3593
[30] Garnier N, Chiffaudel A and Daviaud F 2003 Nonlinear dynamics of waves and modulated waves in 1d thermocapillary flows. II. convective/absolute transitions *Physica* D **174** 30
[31] Raskin D M and de Boer P A J 1999 Rapid pole-to-pole oscillation of a protein required for directing division to the middle of Escherichia coli *Proc. Natl Acad. Sci. USA* **96** 4971
[32] Lutkenhaus J 2007 Assembly dynamics of the bacterial MinCDE system and spatial regulation of the Z ring *Annu. Rev. Biochem.* **76** 539
[33] Loose M, Kruse K and Schwille P 2011 Protein self-organization: lessons from the min system *Annu. Rev. Biophys.* **40** 315
[34] Malomed B A 1984 Nonlinear waves in nonequlibrium systems of the oscillatory type, part I *Physik* B **55** 241
[35] Aranson I and Tsimring L 1995 Domain walls in wave patterns *Phys. Rev. Lett.* **75** 3273

[36] Gelens L and Knobloch E 2011 Traveling waves and defects in the complex Swift–Hohenberg equation *Phys. Rev.* E **84** 056203
[37] Eckhaus V 1965 *Studies in Nonlinear Stability Theory* (Berlin: Springer)
[38] Kramer L and Zimmermann W 1985 On the Eckhaus instability for spatially periodic patterns *Physica* D **16** 221
[39] Lowe M and Gollub J P 1985 Pattern selection near the onset of convection: the Eckhaus instability *Phys. Rev. Lett.* **55** 2575
[40] Dominguez-Lerma M A, Cannell D S and Ahlers G 1986 Eckhaus boundary and wave-number selection in rotating Couette–Taylor flow *Phys. Rev.* A **34** 4956
[41] Zimmermann W and Kramer L 1985 Wavenumber restriction in the buckling instability of a rectangluar plate *J. Phys.* **46** 343
[42] Janiaud B, Pumir A, Bensimon D, Croquette V, Richter H and Kramer L 1992 The Eckhaus instability for traveling waves *Physica* D **55** 269
[43] Liu Y and Ecke R E 1997 Eckhaus-Benjamin-Feir instability of rotating convection *Phys. Rev. Lett.* **78** 4391
[44] Howard M, Rutenberg A D and de Vet S 2001 Dynamic compartmentalization of bacteria: accurate division in *E. coli Phys. Rev. Lett.* **87** 278102
[45] Meinhardt H and de Boer P A J 2001 Pattern formation in Escherichia coli: a model for the pole-to-pole oscillations of Min proteins and the localization of the division site *Proc. Natl Acad. Sci. USA* **98** 14202
[46] Halatek J and Frey E 2012 Highly canalized MinD transfer and MinE sequestration explain the origin of robust MinCDE-protein dynamics *Cell Reports* **1** 741
[47] Bonny M, Fischer-Friedrich E, Loose M, Schwille P and Kruse K 2013 Membrane binding of MinE allows for a comprehensive description of min-protein pattern formation *PLoS Comput. Biol.* **9** e1003347
[48] Bánsági T, Vanag V K and Epstein I R 2012 Two- and three-dimensional standing waves in a reaction–diffusion system *Phys. Rev.* E **86** 045202
[49] Yang L, Dolnik M, Zhabotinsky A M and Epstein I R 2002 Pattern formation arising from interactions between turing and wave instabilities *J. Chem. Phys.* **117** 7259
[50] Wu F, van Schie B G C, Keymer J E and Dekker C 2015 Symmetry and scale orient Min protein patterns in shaped bacterial sculptures *Nat. Nanotechnol.* **10** 719
[51] Wu F, Halatek J, Reiter M, Kingma E, Frey E and Dekker C 2016 Multistability and dynamic transitions of intracellular protein patterns *Mol. Syst. Biol.* **12** 873
[52] Zieske K and Schwille P 2014 Reconstitution of self-organized protein gradients as spatial cues in cell-free systems *eLife* **3** e03949
[53] Fischer-Friederich E, Meacci G, Lutkenhaus J, Chaté H and Kruse K 2010 Intra- and intercellular fluctuations in Min-protein dynamics decrease with cell length *Proc. Natl Acad. Sci. USA* **107** 6134
[54] Hiscock T W and Megason S G 2015 Orientation of turing-like patterns by Morphogen gradients tissue anisotropies *Cell Syst.* **1** 408

Publication 2

Pattern orientation in finite domains without boundaries

L. Rapp, F. Bergmann, and W. Zimmermann

EPL **113**, 28006 (2016)
(DOI: 10.1209/0295-5075/113/28006)

Reprinted with permission from the EPL Association

A Letters Journal Exploring the Frontiers of Physics

January 2016

EPL, **113** (2016) 28006
doi: 10.1209/0295-5075/113/28006

www.epljournal.org

Pattern orientation in finite domains without boundaries

Lisa Rapp, Fabian Bergmann and Walter Zimmermann

Theoretische Physik I, Universität Bayreuth - 95440 Bayreuth, Germany

received 24 October 2015; accepted in final form 4 February 2016
published online 18 February 2016

PACS 89.75.Kd – Patterns
PACS 87.18.-h – Biological complexity
PACS 47.20.-k – Fluid instabilities

Abstract – We investigate the orientation of nonlinear stripe patterns in finite domains. Motivated by recent experiments, we introduce a control parameter drop from supercritical inside a domain to subcritical outside without boundary conditions at the domain border. As a result, stripes align perpendicularly to shallow control parameter drops. For steeper drops, non-adiabatic effects lead to a surprising orientational transition to parallel stripes with respect to the borders. We demonstrate this effect in terms of the Brusselator model and generic amplitude equations.

editor's choice Copyright © EPLA, 2016

Introduction. – Pattern formation is central to the wealth of fascinating phenomena in nature. It occurs in a great variety of physical, chemical and living systems [1,2]. Examples include patterns in isotropic and anisotropic convection systems [3–7], chemical reactions [8,9] and biological systems [10–12], or environmental patterns [13].

In real systems, patterns emerge in finite areas or volumes. Consequently, spatially periodic patterns only contain a finite number of wavelengths. Along the system borders, the relevant fields have to obey boundary conditions that influence the pattern in different ways [3,14–25]. In isotropic systems, stationary patterns may be oriented perpendicularly to the boundaries [3,15]. In thermal convection, convection rolls align perpendicularly to side walls due to boundary conditions for the flow fields [17–19]. Boundary conditions at the side walls may also restrict the range of possible stable wave numbers of periodic patterns [20]. Traveling waves of finite wave number may be reflected at the boundaries leading to a number of interesting and complex phenomena [21–25].

However, finite systems can also be achieved when the fluxes and forces driving a pattern, the so-called control parameters, are sufficiently strong (supercritical) only in a subdomain of the system. In this case, no specific boundary conditions act on the fields at *control parameter drops* to subcritical values. Related to this are studies of ramps in quasi–one-dimensional systems [26], whereby smooth ramps may lead to wave number selection [26,27] and rapid parameter changes to pinning effects for spatially periodic patterns [28]. But the effects of restricting two dimensional patterns to a finite domain by control parameter drops have not been systematically investigated so far. Examples of pattern orientations resulting from different widths of the control parameter drops are shown in fig. 1 and explained in this work.

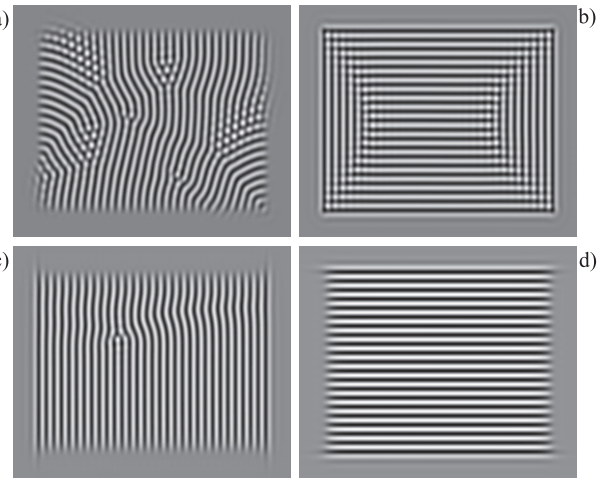

Fig. 1: Stripe patterns inside supercritical subdomains in the Brusselator model. The control parameter drops on different length scales $\delta_{x,y}$ along x and y from $\beta_m = 0.05$ to subcritical values in a wide vicinity: (a) $\delta_x = \delta_y = \lambda_c$, (b) $\delta_x = \delta_y = 0.32\lambda_c$, (c) $\delta_x = 0.32\lambda_c$, $\delta_y = 1.5\lambda_c$, (d) $\delta_x = 1.5\lambda_c$, $\delta_y = 0.32\lambda_c$.

Recent experiments where pattern forming protein reactions take place in finite subdomains of substrates [29] belong to this class. Control parameter drops can also be designed in light-sensitive chemical reactions where illumination of the reaction cell suppresses pattern

formation [30,31]. If the illumination is only applied to a subdomain of the system, again no boundary conditions for the concentration fields are defined along the edge of the illumination mask.

We investigate how control parameter drops along the borders of a supercritical subdomain affect the orientation of stationary spatially periodic patterns when no boundary conditions for the fields are specified. We choose the Brusselator as a representative model system to study the influence of the control parameter drop width. This is complemented by studies of the so-called amplitude equations for supercritical bifurcations to spatially periodic patterns [3]. As a general description for this class of patterns, the conclusions drawn from the amplitude equations emphasize the universality of our results.

For large drop widths, we find that stripes align perpendicularly to the borders of the supercritical control parameter domain. By decreasing the length scale for the control parameter drop, we find a surprising orientational transition to stripes in parallel alignment. The analysis of the amplitude equations reveals additional non-adiabatic, resonance-like effects favouring parallel stripes.

Model systems and control parameter drop. –

Brusselator. The Brusselator is a common model for reaction-diffusion systems [32–35]. We use it as a prototype system for supercritical bifurcations to spatially periodic patterns (Turing patterns). It describes the nonlinear behaviour of the concentration fields $u(x,y,t)$ and $v(x,y,t)$:

$$\partial_t u = \nabla^2 u + a - (b+1)u + u^2 v\,, \tag{1a}$$
$$\partial_t v = D\nabla^2 v + bu - u^2 v, \tag{1b}$$

with the *control parameter* b and constant parameters a, D. These equations have the homogeneous fixed point solution

$$u_h = a\,, \qquad v_h = b/a. \tag{2}$$

Turing patterns with the critical wave number q_c bifurcate from this basic state for control parameter values beyond its critical one b_c [34], where

$$b_c = (1+a\eta)^2\,, \qquad q_c = \sqrt{a\eta}, \tag{3}$$

and $\eta := \sqrt{1/D}$. The relative distance β of the control parameter from its critical value b_c is given by

$$b = b_c(1+\beta), \tag{4}$$

i.e. $\beta_c = 0$. Hexagons are typical for the Brusselator near the onset of Turing patterns. But in this work, we consider the special case $D = a^2$ where stripes are preferred at the onset [35]. In this case, the critical wavelength of the stripes according to eq. (3) is $\lambda_c := 2\pi/q_c = 2\pi$. We choose $a = 4$ throughout this work.

Amplitude equations. The two concentration fields u and v may be combined to the vector field $\mathbf{w}(\mathbf{r},t) = (u(\mathbf{r},t), v(\mathbf{r},t))$. We write spatially periodic stripes with the wave vector $\mathbf{q}_c$ in the form [3,34]

$$\mathbf{w}(\mathbf{r},t) = \mathbf{w}_h + A\tilde{\mathbf{w}}\mathrm{e}^{\mathrm{i}(\mathbf{q}_c\cdot\mathbf{r})} + A^*\tilde{\mathbf{w}}^*\mathrm{e}^{-\mathrm{i}(\mathbf{q}_c\cdot\mathbf{r})}, \tag{5}$$

where $\mathbf{w}_h = (u_h, v_h)$. Slow variations (compared to the wavelength λ_c) of the envelope $A(\mathbf{r},t)$ can be described by a dynamical amplitude equation [3,36].

The Brusselator model is isotropic. Hence, in extended systems only the magnitude q_c of the critical wave vector $\mathbf{q}_c$ for Turing stripes is fixed, but not its direction. Thus, all stripe orientations are equally likely at pattern onset. We consider the amplitude equations in two limits of stripe orientations: $\mathbf{q}_c = (q_c, 0)$ and $\mathbf{q}_c = (0, q_c)$, called parallel and perpendicular hereafter. The reduction method to amplitude equations, the so-called multiple scale analysis, is well established for supercritical bifurcations [3,36]. The generic amplitude equations for the two stripe orientations in the case of a small and constant control parameter β are

$$\partial_t A = \beta A + \mathcal{L}A - g|A|^2 A, \tag{6}$$

with

$$\mathcal{L} = \mathcal{L}_\parallel^2 := \xi_0^2\left(\partial_x - \frac{\mathrm{i}}{2q_c}\partial_y^2\right)^2, \quad \text{for} \quad \mathbf{q}_c = (q_c, 0), \tag{7a}$$

$$\mathcal{L} = \mathcal{L}_\perp^2 := \xi_0^2\left(\partial_y - \frac{\mathrm{i}}{2q_c}\partial_x^2\right)^2, \quad \text{for} \quad \mathbf{q}_c = (0, q_c). \tag{7b}$$

The coherence length ξ_0 and the nonlinear coefficient g for the Brusselator in the special case of $D = a^2$ are $\xi_0^2 = 1$ and $g = 3/(2a^2)$ [35].

Control parameter drop. We introduce the control parameter drop by assuming the spatially dependent control parameter $\beta(x, \delta_x)$:

$$\beta = \beta_0 + \frac{M}{2}\left[\tanh\left(\frac{x - x_l}{\delta_x}\right) - \tanh\left(\frac{x - x_r}{\delta_x}\right)\right]. \tag{8}$$

We assume $L := x_r - x_l \gg \lambda_c$ and $\beta_0 < 0$. M and β_0 are chosen such that the maximum value $\beta_m = \beta_0 + M$ is small and positive. Then $\beta(x, \delta_x)$ is supercritical in the subdomain $\bar{x}_l < x < \bar{x}_r$, where

$$\bar{x}_{l,r} = x_{l,r} \pm \frac{\delta_x}{2}\,\ln\left(\frac{-\beta_0}{M + \beta_0}\right), \tag{9}$$

and drops down to the subcritical value β_0 outside this domain. The steepness of the control parameter drop around $\bar{x}_{l,r}$ increases with decreasing values of the drop width δ_x.

For small values of δ_x, the control parameter $\beta(x, \delta_x)$ varies rapidly in a narrow range around $\bar{x}_{l,r}$. However, only the slowly (adiabatically) varying contributions to $\beta(x, \delta_x)$ affect the solutions of amplitude equations. The rapidly (non-adiabatically) varying part is smoothed out and must be treated separately. We therefore decompose

$\beta(x,\delta_x)$ into an adiabatic and non-adiabatic part. For this purpose, we introduce the slow length scale $\delta_A := 2\xi_0/\sqrt{\beta_m} > \delta_x$ and choose $\beta_0 = -\varepsilon$, $M = 2\varepsilon$ (where ε is positive and small). We then express the slowly varying contribution $B_0(x)$ via eq. (8) by choosing $\delta_x = \delta_A$:

$$B_0(x) = \beta(x,\delta_A). \tag{10}$$

The difference between $\beta(x,\delta_x)$ and $B_0(x)$ becomes small in the centre of $[x_l, x_r]$ and takes its largest values around $x_{l,r}$. We expand the rapidly varying difference $\beta(x,\delta_x) - B_0(x)$ into a series to obtain

$$\beta(x,\delta_x) = B_0(x) + \frac{M}{2}\sum_m \Big\{ B_m^l(x)\sin\left[mq_c(x-x_l)\right] + B_m^r(x)\sin\left[mq_c(x-x_r)\right]\Big\}, \tag{11}$$

where $m = n/N_L$, $n \in N$ and $N_L = L/\lambda_c$. The functions $B_m^{l,r}(x)$ are localised around $x_{l,r}$ and we choose a Gaussian for their representation:

$$B_m^{l,r}(x) = \hat{B}_m^{l,r}\,\exp\left[-\frac{(x-x_{l,r})^2}{\delta_{G,m}^2}\right]. \tag{12}$$

The Gaussian amplitudes $\hat{B}_m^{l,r}$ and their widths $\delta_{G,m}$ are determined via a correlation analysis. We calculate the correlation function between the rapidly varying part

$$\Delta\tilde{\beta}(x,\delta) = \tanh(x/\delta) - \tanh(x/\delta_A) \tag{13}$$

and the test function

$$f_m(x,\delta_{\rm test}) = \frac{1}{\sqrt{\pi}\delta_{\rm test}}\,\mathrm{e}^{-x^2/\delta_{\rm test}^2}\sin(mq_cx). \tag{14}$$

We then choose the Gaussian width $\delta_{G,m}$ to be the value of $\delta_{\rm test}$ that maximises the correlation function. The amplitudes $\hat{B}_m^{l,r}$ are calculated via the overlap integral between $f_m(x,\delta_{G,m})$ and $\Delta\tilde{\beta}$. Figure 2(a) shows the contributions $\bar{B}_m^l := \varepsilon B_m^l(x)\sin(mq_cx)$ for $m = 1,2$ in comparison to the full shape of $\beta(x,\delta_x)$. Both functions are localised around $x_l = 0$ and approach zero within a short range ($\ll \delta_A$) around the control parameter drop. The Gaussian amplitudes $\hat{B}_1^{l,r}$ and $\hat{B}_2^{l,r}$ decrease as a function of the drop width δ_x (fig. 2(b)). These non-adiabatic contributions vanish for $\delta_x > \delta_A$. The amplitude $\hat{B}_1^{l,r}$ is usually larger than $\hat{B}_2^{l,r}$, except in the limit of very small drop widths.

The patterns in fig. 1 are obtained for a rectangular supercritical subdomain of the control parameter in the form

$$\beta = \beta_0 + \frac{M}{4}\left[\tanh\left(\frac{x-x_l}{\delta_x}\right) - \tanh\left(\frac{x-x_r}{\delta_x}\right)\right] \times \left[\tanh\left(\frac{y-y_b}{\delta_y}\right) - \tanh\left(\frac{y-y_t}{\delta_y}\right)\right]. \tag{15}$$

Here, we introduced a second drop width δ_y to describe the additional spatial dependence of β in the y-direction. $\beta(x,y,\delta_x,\delta_y)$ is supercritical in the two-dimensional area $[\bar{x}_l,\bar{x}_r]\times[\bar{y}_b,\bar{y}_t]$.

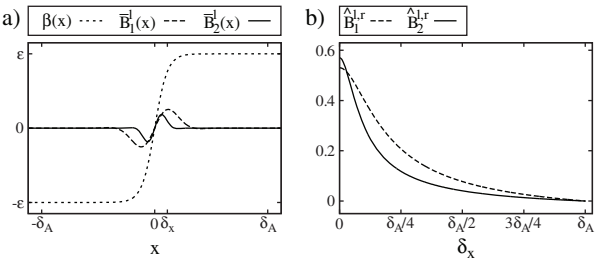

Fig. 2: (a) Contributions $\bar{B}_1^l(x)$ and $\bar{B}_2^l(x)$ to the control parameter drop $\beta(x,\delta_x)$ for $\delta_x = 0.11\delta_A$. (b) Gaussian amplitudes $\hat{B}_1^{l,r}$ and $\hat{B}_2^{l,r}$ of the localised amplitudes as a function of the drop width δ_x for $\varepsilon = 0.05$.

Non-adiabatic effects cause an orientational transition. – We now include the control parameter drop into the amplitude equation using the decomposition given in eq. (11). The control parameter β in eq. (6) is replaced by the slowly (adiabatically) varying part $B_0(x)$ as given by eq. (10). The short-wavelength contributions $\propto B_m^{l,r}(x)\exp(\mathrm{i}mq_cx)$ with $m = 1,2,3,4$ in eq. (11) cause additional (non-adiabatic) terms in the amplitude equation for parallel stripes [37]. It then takes the form

$$\partial_t A = B_0(x)A + \mathcal{L}_\parallel^2 A - g|A|^2A + \sum_{m=1}^{4}\alpha_m B_m(x)\left(A^*\right)^{m-1}. \tag{16}$$

Here, α_m are constant parameters depending on the respective system. The complex localised contributions $B_m(x)$ due to the control parameter drop are given by

$$B_m(x) = \mathrm{i}\frac{M}{4}\left[B_m^l(x)\mathrm{e}^{-\mathrm{i}mq_cx_l} - B_m^r(x)\mathrm{e}^{-\mathrm{i}mq_cx_r}\right]. \tag{17}$$

The magnitudes of $B_1(x)$ and $B_2(x)$ are similar, as shown in fig. 2. The coefficient $B_2(x)$ reduces the threshold of the pattern onset [37]. $B_1(x)$ changes the supercritical bifurcation (in the case $B_1 = 0$) into an imperfect one [37,38] and, therefore, has a stronger impact than $B_2(x)$. The effects caused by $B_{3,4}(x)$ are restricted to the post-threshold regime and are much smaller than $B_{1,2}(x)$. Hence, they are neglected henceforth. Equation (16) can be derived from the functional

$$F_\parallel = \int \mathrm{d}x\mathrm{d}y\Big[-B_0(x)|A|^2 + \frac{g}{2}|A|^4 + \left|\mathcal{L}_\parallel A\right|^2 - \sum_{m=1}^{2}\frac{\alpha_m}{m}\left(B_m(x)A^{*^m} + B_m^*(x)A^m\right)\Big] \tag{18}$$

via $\partial_t A = -\delta F_\parallel/\delta A^*$. For the Brusselator in the case $D = a^2$, we find $\alpha_1 = 2a$ and $\alpha_2 = 5/3$.

The amplitude equation for perpendicular stripes with $\mathbf{q}_c = (0,q_c)$ is not affected by resonance contributions $\propto B_m$. It is described by eq. (6) with $\mathcal{L} = \mathcal{L}_\perp^2$ as given in eq. (7b) and the slowly varying control parameter

$\beta = B_0(x)$, cf. eq. (10). The related functional is

$$F_\perp = \int \mathrm{d}x\mathrm{d}y \left[-B_0(x)|A|^2 + \frac{g}{2}|A|^4 + |\mathcal{L}_\perp A|^2 \right]. \quad (19)$$

For small values of δ_x, the coefficients $B_{1,2}$ have considerable magnitude (fig. 2(b)). However, the related non-adiabatic effects only affect the amplitude equation for parallel stripes, cf. eq. (16). Due to the imperfect bifurcation, parallel stripes already have a finite amplitude below the bulk threshold $\beta_m = 0$, especially around $x_{l,r}$, where $B_{1,2}$ take the largest values. This finite amplitude A decreases the functional $F_\parallel$ for parallel stripes with respect to $F_\perp$. Thus, for small values of δ_x, parallel stripes are preferred compared to perpendicular stripes.

For large values of δ_x, the non-adiabatic contributions $B_{1,2}$ become small and can be neglected (fig. 2(b)). In this case, the amplitude equations and the functionals for the two different stripe orientations only differ in the linear operator. These include different orders of derivatives in the x-direction: $|\partial_x A|^2$ in the functional for parallel stripes, eq. (18), and $|\partial_x^2 A|^2$ for perpendicular stripes, eq. (19). Thus, spatial variations of the amplitude $A(\mathbf{r}, t)$ affect the two functionals differently. The slow spatial variation of the control parameter $B_0(x)$ in the x-direction is reflected in a spatial variation of the amplitude $A(\mathbf{r}, t)$. This increases both functionals. However, due to the different orders of x-derivatives, the functional for perpendicular stripes has a lower value [3,39]. Therefore, perpendicular stripes will be preferred for large δ_x.

According to this reasoning, we predict stripes aligned perpendicular to the supercritical border for a large drop width δ_x and parallel for small δ_x. Therefore, we expect an orientational transition for medium values of δ_x. Note, for these considerations only the contributions B_0, B_1 and B_2 to the decomposition in eq. (11) are taken into account. However, the predicted orientational transition of stripes is rather insensitive to these approximations as confirmed by simulations of the Brusselator in the next section.

Numerical results for the Brusselator. – In the previous part we found an orientational transition of stripe patterns by changing the width of control parameter drops. This prediction is based on a reasoning including approximations. Therefore, the effect is verified by simulations of the Brusselator model, cf. eqs. (1), with supercritical subdomains of width $L = 20\lambda_c$, embedded in larger subcritical domains with overall system sizes $l_{x,y}$. The model is solved using a common pseudospectral method with periodic boundary conditions [40] and $N_{x,y}$ modes, respectively. We choose $\beta_0 = -0.05$ and perturb the basic solution by small amplitude random noise.

For large widths δ_x of control parameter drops, *i.e.* slow variations of the control parameter, the preferred orientation of a stripe pattern is nearly perpendicular to the borders of the supercritical domain, *i.e.* $\mathbf{q} \sim (0, q_c)$, as shown in fig. 3 for $\delta_x = 5\lambda_c$. This confirms the prediction in terms of the amplitude equations in the previous section

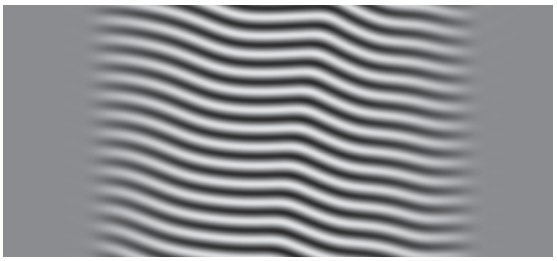

Fig. 3: Stripes favour a perpendicular orientation with respect to shallow control parameter drops ($\delta_x = 5\lambda_c$). Simulation of the Brusselator started at $\beta_m = 0.001$ and was slowly increased to $\beta_m = 0.05$. Parameters: $l_x = l_y = 50\lambda_c$, $N_x = N_y = 1024$. Note: only a cutout of the simulation is shown.

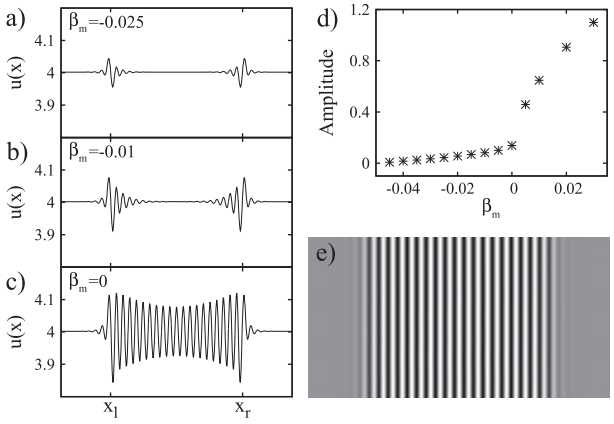

Fig. 4: Simulations of the Brusselator model with a narrow control parameter drop ($\delta_x = 0.5\lambda_c$). Cross-sections of the two-dimensional stripe pattern for (a) $\beta_m = -0.025$, (b) $\beta_m = -0.01$, (c) $\beta_m = 0$. (d) The stripe amplitude as a function of β_m implies an imperfect bifurcation. (e) Snapshot of the parallel stripes for $\beta_m = 0.02$. Simulation parameters: $l_x = 50\lambda_c$, $l_y = 25\lambda_c$, $N_x = 1024$, $N_y = 512$.

(for similar results for periodic modulations in extended systems see ref. [41]). Similar orientations are obtained for drop widths down to about $\delta_x \simeq \lambda_c$.

For small δ_x, *e.g.* $\delta_x = 0.5\lambda_c$, the stripes align parallelly to the borders of the supercritical range, *i.e.* $\mathbf{q}_c \sim (q_c, 0)$, as in fig. 4(e) for $\beta_m = 0.02$. Moreover, localised Turing stripe patterns of finite amplitude occur around the borders at $x_{l,r}$ already at subcritical values of β_m (see cross-sections in fig. 4(a) and (b)). For increasing β_m, they expand into the whole supercritical domain. At the bulk threshold $\beta_m = 0$ (fig. 4(c)) the stripes already have a finite amplitude throughout the range $[x_l, x_r]$. The maximum stripe amplitude of the stationary solution as a function of β_m is shown in the bifurcation diagram in fig. 4(d). The form of the bifurcation is imperfect, as expected from the analysis on the basis of the amplitude equations in the previous section.

The two different preferred stripe orientations for large $\delta_x = 5\lambda_c$ in fig. 3 and small $\delta_x = 0.5\lambda_c$ in fig. 4 clearly confirm an orientational transition of stripes in the

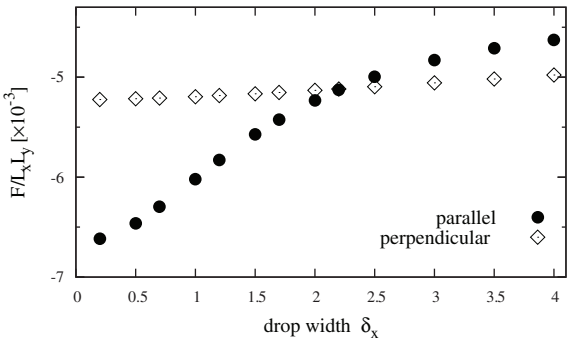

Fig. 5: Comparison of the functional for stripes as a function of the drop width δ_x with the stripe wave vector $\mathbf{q}_c = (0, q_c)$ (filled circles) and $\mathbf{q}_c = (q_c, 0)$ (open diamonds). Parameters: $\beta_0 = -0.05$, $M = 0.1$.

supercritical domain depending on the width of the control parameter drop along its border.

We can further restrict the domain size by varying the control parameter simultaneously along the x- and y-direction, cf. eq. (15). In these rectangular domains[1], one can combine different drop widths δ_x and δ_y to trigger different stripe orientations as shown by four examples in fig. 1. Combining, *e.g.*, large drop widths at the long side of the rectangle with small drop widths at the short side creates a remarkably uniform stripe pattern, cf. fig. 1(d). Using different combinations of $\delta_{x,y}$ may be a promising tool for designing Turing patterns in localised light-sensitive chemical reactions [42].

Orientational transition regime. – The orientational transition of stripes is deduced in terms of amplitude equations and confirmed by numerical simulations of the Brusselator model. The amplitude equations can be derived from the functionals, eqs. (18) and (19). Calculating these functionals as a function of the drop width allows to determine the preferred orientation for this δ_x. In the range where $F_\perp < F_\parallel$, a perpendicular stripe orientation is expected and vice versa. For this purpose, we perform simulations of the amplitude equations for the two stripe orientations using the aforementioned pseudospectral algorithm (simulation parameters: $l_x = l_y = 50\lambda_c$, $N_x = N_y = 1024$, $L = 20\lambda_c$, $\beta_0 = -0.05$, $\beta_m = 0.05$). When the solutions reach the stationary state, the functionals displayed in fig. 5 are calculated.

The functional corresponding to perpendicular stripes in eq. (19) does not contain the non-adiabatic contributions B_1 and B_2 to the control parameter drop. Regardless of the assumptions made for the justification of eq. (19) and the related amplitude equation, one may use $\beta(x, \delta_x)$ instead of $B_0(x)$. The functional then deviates only slightly from its constant value in the case of $B_0(x)$. In addition, fig. 5 shows that the functional with $\beta(x, \delta_x)$ is nearly independent of δ_x, *i.e.* stripes perpendicular to the border of the supercritical range are rather insensitive to the width δ_x.

For parallel stripes, $\mathbf{q} = (q_c, 0)$, the resonance effects covered by B_1 (and B_2) are relevant and the associated functional is given in eq. (18). The two functionals for the two different stripe orientations are shown as a function of the drop width δ_x in fig. 5. For narrow control parameter drops, *i.e.* δ_x small, the functional for parallel stripes is significantly lower. Thus, the parallel orientation is preferred. However, the functional for parallel stripes strongly increases as a function of the drop width. The orientational transition takes place at the intersection of the two functionals. For larger δ_x, the perpendicular orientation of the stripes is preferred.

Summary and conclusions. – In this work, we identified and investigated a new class of finite pattern forming systems confined by control parameter drops from super- to subcritical values. These orient stripe patterns even without boundary conditions for the relevant fields. The stripe orientation depends on the width of the control parameter drops. We found a novel *orientational transition of stripe patterns* with respect to the borders as a function of the width of control parameter drops.

In light-sensitive chemical reaction-diffusion systems showing Turing patterns [30,31] the transition length between the patterns (supercritical) and the homogeneous state (subcritical) may be varied by the length of a smooth transition between illuminated and dark areas.

The Swift-Hohenberg (SH) model [43] is, besides the Brusselator a further paradigmatic model for studying the formation of spatially periodic patterns [2,3]. It behaves differently with respect to control parameter drops along the border of a supercritical domain. The basic state of the Brusselator is a function of the control parameter b, cf. eq. (2). Therefore, control parameter drops change the basic state of the bifurcation to Turing patterns. In the case of steep control parameter drops, the bifurcation to parallel stripes becomes imperfect, causing a different orientation than for smooth control parameter variations. In contrast, the basic state $u_h = 0$ of the SH model remains unchanged for spatially varying control parameters. The onset of periodic patterns is reduced but the bifurcation remains perfect. The local 1:2 resonance occurring in the case of a steep control parameter drop is not sufficient to change the stripe orientation like for the Brusselator. The same applies to the mean-field model for block copolymers (see, *i.e.*, [44]). Therefore, we do not find the aforementioned orientational transition of stripe patterns in the SH or the block copolymer model. However, in common systems where the basic state is also changed by control parameter variations, orientational transitions of stripe patterns are very likely.

Our results for stationary patterns may also be important for traveling waves that occur, for instance, in the cell biological MinE/MinD protein reaction on flat substrates [12,29]. To mimic the effects of cell confinement

[1]Simulation parameters: $\beta_0 = -0.1$, $\beta_m = 0.05$, $L_x = 30\lambda_c$, $L_y = 20\lambda_c$, $l_x = 60\lambda_c$, $l_y = 50\lambda_c$, $N_x = N_y = 1024$.

in such extended experiments, reactive membranes were created in subdomains of the substrate [29,45]. In this way, the traveling waves are restricted to the range above the functionalised parts of the membrane. These may be interpreted as subdomains with a supercritical control parameter. In this experiment the traveling waves align perpendicularly to the borders of the functionalised area [29]. It is very likely that this orientational behaviour is again governed by generic principles similar to those discussed in this work and specific molecular reaction schemes or three-dimensional effects provide quantitative modifications [29,46,47]. Is the complex behavior of MinE/MinD oscillations in further restricted domains, as investigated recently in ref. [48], determined by the specific properties of the kinetic reaction models? Or do again generic principles of pattern formation play a leading role as described in this work?

* * *

Enlightening discussions with M. Hilt and M. Weiß are gratefully acknowledged.

REFERENCES

[1] Ball P., *The Self-Made Tapestry: Pattern Formation in Nature* (Oxford University Press, Oxford) 1998.
[2] Cross M. C. and Greenside H., *Pattern Formation and Dynamics in Nonequilibrium Systems* (Cambridge University Press, Cambridge) 2009.
[3] Cross M. C. and Hohenberg P. C., *Rev. Mod. Phys.*, **65** (1993) 851.
[4] Lappa M., *Thermal Convection: Patterns, Evolution and Stability* (Wiley, New York) 2010.
[5] Weiss S., Seiden G. and Bodenschatz E., *New J. Phys.*, **14** (2012) 053010.
[6] Bodenschatz E., Zimmermann W. and Kramer L., *J. Phys. (Paris)*, **49** (1988) 1875.
[7] Kramer L. and Pesch W., *Annu. Rev. Fluid Mech.*, **27** (1995) 515.
[8] Kapral R. and Showalter K. (Editors), *Chemical Waves and Patterns* (Springer, The Netherlands) 1995.
[9] Mikhailov A. S. and Showalter K., *Phys. Rep.*, **425** (2006) 79.
[10] Ben-Jacob E., Shochet O., Tenenbaum A., Cohen I., Czirok A. and Vicsek T., *Nature*, **368** (1994) 46.
[11] Kondo S. and Miura T., *Science*, **329** (2010) 1616.
[12] Loose M., Fischer-Friedrich E., Ries J., Kruse K. and Schwille P., *Science*, **320** (2008) 789.
[13] Meron E., *Nonlinear Physics of Ecosystems* (CRC Press, Boca Raton) 2015.
[14] Kramer L. and Hohenberg P. C., *Physica D*, **13** (1984) 357.
[15] Greenside H. and Coughran W. M., *Phys. Rev. A*, **30** (1984) 398.
[16] Kramer L., Hohenberg P. C. and Riecke H., *Physica D*, **15** (1985) 402.
[17] Cross M. C., *Phys. Fluids*, **25** (1982) 936.
[18] Bajaj K. M., Mukolobwiez N., Currier N. and Ahlers G., *Phys. Rev. Lett.*, **83** (1999) 5282.
[19] Chiam K.-H., Paul M. R., Cross M. C. and Greenside H., *Phys. Rev. E*, **67** (2003) 056206.
[20] Cross M. C., Daniels P. G., Hohenberg P. C. and Siggia E. D., *J. Fluid Mech.*, **127** (1983) 155.
[21] Cross M. C., *Phys. Rev. Lett.*, **57** (1986) 2935.
[22] Cross M. C., *Phys. Rev. A*, **38** (1988) 3593.
[23] Moses E., Fineberg J. and Steinberg V., *Phys. Rev. A*, **35** (1987) 2757.
[24] Kolodner P. and Surko C. M., *Phys. Rev. Lett.*, **61** (1988) 842; Kolodner P., *Phys. Rev. A*, **44** (1991) 6448.
[25] Garnier N., Chiffaudel A. and Daviaud F., *Physica D*, **174** (2003) 30.
[26] Kramer L., Ben-Jacob E., Brand H. and Cross M. C., *Phys. Rev. Lett.*, **49** (1982) 1891.
[27] Cross M. C., *Phys. Rev. A*, **29** (1984) 391.
[28] Riecke H., *Europhys. Lett.*, **2** (1986) 1.
[29] Schweizer J., Loose M., Bonny M., Kruse K., Mönch I. and Schwille P., *Proc. Natl. Acad. Sci. U.S.A.*, **109** (2012) 15283.
[30] Munuzuri A. P., Dolnik M., Zhabotinsky A. M. and Epstein I. R., *J. Am. Chem. Soc.*, **121** (1999) 8065.
[31] Dolnik M., Berenstein I., Zhabotinsky A. M. and Epstein I. R., *Phys. Rev. Lett.*, **87** (2001) 238301.
[32] Prigogine I. and Lefever R., *J. Chem. Phys.*, **48** (1968) 1695.
[33] Nicolis G. and Prigogine I., *Self-Organization in Nonequilibrium Systems, from Dissipative Structures to Order through Fluctuations* (Wiley, New York) 1977.
[34] Walgraef D., *Spatio-Temporal Pattern Formation* (Springer, New York) 1997.
[35] Pena B. and Perez-Garcia C., *Phys. Rev. E*, **64** (2001) 056213.
[36] Newell A. C. and Whitehead J. A., *J. Fluid Mech.*, **38** (1969) 279.
[37] Coullet P., *Phys. Rev. Lett.*, **56** (1986) 724.
[38] Peter R. *et al.*, *Phys. Rev. E*, **71** (2005) 046212.
[39] Malomed B. A. and Nepomnyashchy A. A., *Europhys. Lett.*, **21** (1993) 195.
[40] Kopriva D. A., *Implementing Spectral Methods for Partial Differential Equations* (Springer, The Netherlands) 2009.
[41] Freund G., Pesch W. and Zimmermann W., *J. Fluid Mech.*, **673** (2011) 318.
[42] Steinbock O., Kettunen P. and Showalter K., *Science*, **269** (1995) 1857.
[43] Swift J. B. and Hohenberg P. C., *Phys. Rev. A*, **15** (1977) 319.
[44] Weith V., Krekhov A. and Zimmermann W., *J. Chem. Phys.*, **139** (2013) 054908.
[45] Lagny T. J. and Bassereau P., *Interface Focus*, **5** (2015) 20150038.
[46] Halatek J. and Frey E., *Cell Rep.*, **1** (2012) 741.
[47] Halatek J. and Frey E., *Proc. Natl. Acad. Sci. U.S.A.*, **111** (2014) E1817.
[48] Wu F., van Schie B. G. C., Keyner J. E. and Dekker C., *Nat. Nanotechnol.*, **10** (2015) 719.

Publication 3

Reflection of nonlinear wave patterns in finite domains without boundaries

F. Bergmann and W. Zimmermann

submitted to Physical Review E (06/2019)

Reflection of nonlinear-wave patterns in finite domains without boundaries

Fabian Bergmann and Walter Zimmermann
Theoretische Physik I, Universität Bayreuth, 95440 Bayreuth, Germany
(Dated: August 15, 2019)

We analyse nonlinear traveling wave patterns in the presence of control parameter variations at the ends of a finite domain. This is motivated by recent experiments, where the control parameter is supercritical inside a domain and subcritical outside. We find traveling wave reflection near rapid control-parameter variations at the domain ends even without boundary conditions for the wave fields. The resulting competition scenarios between the incoming and the reflected traveling waves depends strongly on the group velocity v_g of traveling waves. Traveling waves extend over the whole subdomain for small v_g. Raising v_g leads first to confined wave states, before blinking states occur. Finally we observe a coexistence between right (left) traveling waves localized near the right (left) end of the subdomain and left (right) traveling waves near left (right) subdomain end. We analyse these effects in terms of a generic complex Swift-Hohenberg model and universal amplitude equations for nonlinear wave patterns.

PACS numbers: 47.43.-3, 05.45.-a

I. INTRODUCTION

Self-organized patterns occur in many physical, chemical and living systems out of thermal equilibrium [51–58]. Very common examples are stripe and traveling (TW) patterns. In nature as well as in controlled experiments, they always occur in finite domains which include a finite number of wavelength of a pattern. Thereby the domain size often affects the properties of patterns. While detailed mechanisms leading for instance to stripe or traveling wave (TW) pattern are as different as the systems, a pattern often shows inherent system spanning properties in the bulk and with respect to effects of domain ends.

Boundary conditions at domain ends imposed on the fields that describe the patterns break symmetries and affect their nonlinear behavior. For instance, spatially periodic stripe patterns are in extended systems stable for different wave numbers in a so-called Eckhaus stable wavenumber band [59–66]. However, boundary conditions restrict the wavenumber range of stationary periodic patterns and also affect their orientation [53, 67–73]. Traveling waves may in addition be reflected at system boundaries and the interplay between incoming and reflected traveling waves leads to a number of fascinating dynamical scenarios [74–79]. Boundary effects usually increase for a decreasing system size. For instance, in a very small system size the boundary reflection of traveling waves may even outweigh bulk competition between counter propagating traveling waves and therefore may enforce a bifurcation from traveling to standing waves [80]. Breaking the translational symmetry in time by temporal modulations [81–83] or in space by spatial modulations [84, 85] can force nonlinear left and right moving traveling waves into standing waves.

A restriction of the pattern to a finite subdomain can also be achieved without boundary conditions for the involved fields. In this case the driving fluxes and forces, the so-called control parameters, become supercritical only within a subdomain of a system and become subcritical outside. Related to this system class are studies investigating effects of control parameter ramps on stationary, spatially periodic patterns in quasi one-dimensional systems [86], whereby slow (adiabatic) ramps may lead to wave number selection [86, 87]. Rapid parameter changes can produce pinning effects for spatially periodic patterns [88]. The effects of a supercritical control parameter restricted to two-dimensional subdomains has been investigated only recently [89] and revealed a surprising dependence of the orientation of stripe patterns on the steepness of control parameter drops. In experiments a restriction of the supercritical range of the control parameter in a pattern forming system to a subdomain is possible, for instance, in light sensitive chemical reactions by illuminating only a subdomain [90, 91]. Another recently studied example are experiments on traveling Min-protein patterns on extended membranes, which were only reactive in subdomains of the substrate [92, 93]. How control parameter variations affect traveling waves is not systematically investigated so far.

In this work we investigate generic effects of control parameter drops on the nonlinear properties of traveling wave pattern. The control parameter drops from supercritical to subcritical values at the two ends of a one-dimensional subdomain at whose ends no boundary conditions for the fields describing traveling wave are specified. We choose the complex Swift-Hohenberg (CSH) equation as a generic model for traveling waves to explore how the control parameter drop affects the nonlinear behavior of TWs [94–96]. These investigations are complemented by the analysis of coupled amplitude equations for counter propagating TWs. Both model approaches are introduced in Sec. II. For control parameter drop-widths on the scale of a wavelength of traveling waves we obtain three typical nonlinear wave patterns depending on the group velocity as described in III. Small values of the group velocity lead to extended or confined traveling wave states. For intermediate values breathing confined states occur. Finally one observes a coexistence between

localized left and right traveling waves near the opposite ends of the finite domain. The conclusions drawn from the analysis of these equations emphasize the universality of our results.

II. MODEL

A prototype model for supercritically bifurcating traveling waves (TW) is the complex Swift-Hohenberg equation (CSH) for the complex order parameter field $u(x,t)$ (see e.g. [94–96]):

$$\partial_t u = (\varepsilon(x) + ia)u - (1+ib)\left(q_0^2 + \partial_x^2\right)^2 u + if\partial_x^2 u - (1+ic)|u|^2 u\,. \quad (1)$$

This model shows traveling wave solutions of a preferred wavelength $\lambda_0 = 2\pi/q_0$ for positive values of the control parameter $\varepsilon > 0$. Time, space and the complex field, $u(x,t)$ are already scaled such that the four parameters a, b, f, c remain. If needed, the parameter a may be also removed via the transformation $u \to u \cdot \exp(iat)$. The complex field $u(x,t)$ can be interpreted as the envelope of an oscillating real field $w(x,t) \propto u(x,t)\exp(i\omega t) + u^*(x,t)\exp(-i\omega t)$. For $a = b = f = c = 0$ Eq. (1) reduces to the original Swift-Hohenberg equation for stationary periodic patterns [53, 97].

A. Control parameter drop

How does a spatially varying control parameter $\varepsilon(x,\delta)$

$$\varepsilon = -\beta + \frac{M}{2}\left(\tanh\left[\frac{x-x_l}{\delta}\right] - \tanh\left[\frac{x-x_r}{\delta}\right]\right) \quad (2)$$

affect the dynamics of traveling waves? With $L := x_r - x_l \gg \lambda_c = 2\pi/q_0$ and $-\beta + M > 0$ the control parameter ε is supercritical in the range $\bar{x}_l < x < \bar{x}_r$, whereby the boundary positions $\bar{x}_l$ and $\bar{x}_r$ are related to δ, M and β as follows:

$$\bar{x}_{l,r} = x_{l,r} \pm \frac{\delta}{2}\,\ln\left(\frac{\beta}{M-\beta}\right)\,. \quad (3)$$

M and β are chosen such that the maximal value of the control parameter $\varepsilon_m = -\beta + M > 0$ remains small. Around the center of the range $[\bar{x}_l, \bar{x}_r]$ the profile of $\varepsilon(x)$ is nearly flat and locally translational invariant. The steepest variations of $\varepsilon(x)$ take place at x_l and x_r. Outside the supercritical domain the control parameter $\varepsilon(x)$ drops to the subcritical value $-\beta$. The steepness of the control parameter drop around $x_{l,r}$ increases with decreasing values of the drop width δ.

For larger values of δ the control parameter $\varepsilon(x,\delta)$ varies slowly (adiabatically) on the length scale of the wavelength λ_c. In this case the effects of a spatially dependent $\varepsilon(x)$ can be described in the frame work of so-called amplitude equations [53], as described below.

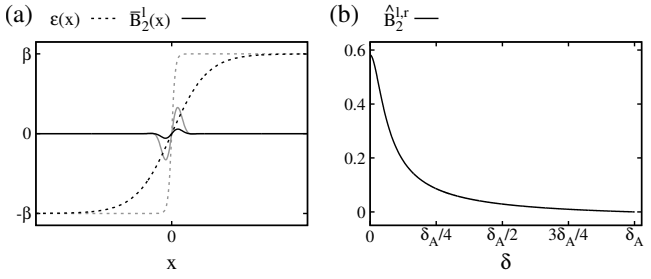

FIG. 1. (a) shows the contribution $\bar{B}_2^l(x) = \beta B_2^l(x)\sin(2q_c x)$ (solid lines) to the control parameter $\varepsilon(x)$ (dashed lines) in Eq. (5) for $\delta = 0.1\pi$ (grey) and $\delta = \pi$ (black). In (b) the peak value $\hat{B}_2^{l,r}$ of $B_2^{l,r}(x)$ in Eq. (6) is plotted as a function of the drop width δ. This peak value decreases with increasing δ

To cover also the effects of a rapidly (non-adiabatically) varying contribution to $\varepsilon(x)$, the related amplitude equations for traveling waves have to be complimented.

In order to separate the slowly from the rapidly varying contributions to $\varepsilon(x)$ we introduce the length scale $\delta_A = 2\xi_0/\sqrt{\varepsilon_m} > \delta$ and choose $M = 2\beta$ with a small value of β. In this case the boundaries of the supercritical region $\bar{x}_l, \bar{x}$ correspond to the position of the control parameter drop x_l, x_r. The slowly varying part of $\varepsilon(x)$ is expressed via Eq. (2) by choosing $\delta = \delta_A$:

$$B_0(x) = \varepsilon(x, \delta_A). \quad (4)$$

The difference between $\varepsilon(x,\delta)$ and $B_0(x)$ vanishes in the center of the range $[x_l, x_r]$ and takes its largest values around $x_{l,r}$. We expand the rapidly varying part of the difference $\varepsilon(x,\delta) - B_0(x)$ into a series as follows

$$\varepsilon(x,\delta) = B_0(x) + \frac{M}{2}\sum_m \Big\{B_m^l(x)\sin\left[mq_c(x-x_l)\right] - B_m^r(x)\sin\left[mq_c(x-x_r)\right]\Big\}, \quad (5)$$

where $m = n/N_L$, $n \in N$ and $N_L = L/\lambda_c$. The functions $B_m^{l,r}(x)$ are localized around $x_{l,r}$ and we choose a Gaussian for their representation:

$$B_m^{l,r}(x) = \hat{B}_m^{l,r}\,\exp\left[-\frac{(x-x_{l,r})^2}{\delta_{G,m}^2}\right]. \quad (6)$$

The Gaussian amplitudes $\hat{B}_m^{l,r}$ and their widths $\delta_{G,m}$ are determined via a correlation analysis as described in Ref. [89].

The two complementary contributions $\bar{B}_2^{l,r}(x) = M/2B_2^{l,r}(x)\sin(2q_c(x-x_{l,r}))$ to Eq. (5) will be crucial in reductions of the CSH model in Eq. (1) to equations for the amplitudes of TWs. The contribution $\bar{B}_2^l(x)$ is shown exemplarily in Fig. 1a) for two values of δ in comparison to the full control parameter variation $\varepsilon(x,\delta)$. $\bar{B}_2^l$ and $\bar{B}_2^r$ are localized around x_l and x_r and both tend to zero within a short distance $< \delta_A$ from x_l and x_r, respectively. The Gaussian amplitudes $\hat{B}_1^{l,r}$ and $\hat{B}_2^{l,r}$ decrease with increasing values of the drop width δ [see Fig. 1b)].

B. Non-adiabatic contributions to $\varepsilon(x,\delta)$ cause resonances

Left and right traveling waves, $u \propto A_{l,r}(x,t)e^{i(\pm q_0 x+\tilde{\omega}t)}$, with complex amplitudes $A_{l,r}(x,t)$ that vary slowly on the scale of the intrinsic wavelength $\lambda_0 = 2\pi/q_0$, are well known solutions of the CSH model in Eq. (1) for a constant control parameter ε. There is a well established mathematical technique for deriving in the range of small ε two coupled, nonlinear equations for the envelopes $A_l(x,t)$ and $A_r(x,t)$ [52, 53, 75, 98]. This technique can also be applied in the case of a slowly varying control parameter $\varepsilon(x,\delta_A) = B_0(x)$. However, $\varepsilon(x)$ in Eq. (5) may include also local and fast varying finite contributions $\propto \sin(2q_0(x-x_{l,r}))$ that affect the solutions considerably as indicated in Fig. 5.

The reduction of the CSH model to the equations for the envelopes requires a projection of the CSH model onto the traveling wave modes $e^{i(\pm q_0 x+\tilde{\omega}t)}$. This provides in the presence of contributions $B_m^{l,r}(x)$ from Eq. (5) also a local resonant coupling between right and left traveling waves in the amplitude equations via the product $A(x,t)\bar{B}_2^{l,r}(x)$. These spatially dependent coupling terms are located around $\bar{x}_{l,r}$ and are a conceptual parallel to temporal resonant forcing [81, 82] near a bifurcation to traveling waves.

Using

$$B_2(x) = \frac{M}{4i}[B_2^l(x)e^{-2iq_0x_l} - B_2^r(x)e^{-2iq_0x_r}] \qquad (7)$$

the two coupled equations for the amplitude of the left traveling wave, $A_l(x,t)$, and the right traveling wave, $A_r(x,t)$, take the following form:

$$(\partial_t + v_g\partial_x)A_r = B_0(x)A_r + \xi_0^2(1+i\tilde{b})\partial_x^2 A_r + B_2(x)A_l - (1+ic)(|A_r|^2 + 2|A_l^2|)A_r\,, \qquad (8a)$$

$$(\partial_t - v_g\partial_x)A_l = B_0(x)A_l + \xi_0^2(1+i\tilde{b})\partial_x^2 A_l + B_2^\star(x)A_r - (1+ic)(|A_l|^2 + 2|A_r^2|)A_l\,. \qquad (8b)$$

Deriving these two coupled equations from the CSHE (1) the coefficients are

$$\xi_0 = 2q_0\,, \qquad v_g = 2fq_0, \qquad \tilde{b} = b + \frac{f}{4q_0^2}\,. \qquad (9)$$

In the case of a slowly varying control parameter $\varepsilon(x,\delta)$, corresponding to larger values of δ, the linear coupling terms $\propto B_2(x)$ in Eqs. (8) become small.

In the limit $B_2 = 0$ the equations (8) have either a finite amplitude solution $A_l(x,t) \neq 0$ and $A_r(x,t) = 0$ or $A_l(x,t) = 0$ and $A_r(x,t) \neq 0$, i.e. the two possible counter propagating waves compete and only one of the two survives.

The localized coefficients $B_2(x)$ and $B_2^*(x)$ cause local coupling between $A_l(x,t)$ and $A_r(x,t)$ and have a similar effect as reflections at $\bar{x}_l$ and $\bar{x}_r$, respectively. In the case of steep control parameter drops and therefore sufficiently large magnitudes of B_2, this resonance induced coupling leads to the interesting spatio-temporal scenarios shown in this work.

III. NONLINEAR WAVE PATTERNS BETWEEN CONTROL PARAMETER DROPS

During the following exploration of the effects of control parameter drops on traveling waves we vary especially the drop width δ and the TW group velocity v_g via the parameter f. The other parameters are fixed: $b = 0$, $c = 0.5$, $q_0 = 2\pi/\lambda_0 = 1$, $\beta = 0.4$ and $M = 0.5$, i. e. $\varepsilon_m = 0.1$. The length of the subdomain with a supercritical control parameter is $L_s = \bar{x}_r - \bar{x}_l \approx 40\cdot 2\pi = 40\lambda_0$ and the length of the whole simulated system is $L_w = 120\lambda_0$. The initial condition in the following simulations is always a right moving wave $\propto \exp(q_0x - \tilde{\omega}t)$ with a small amplitude.

A. Traveling waves

For a width $\delta = \lambda_0$ of the control-parameter drop and rather small values of the group velocity $v_g = 2fq_0$ with $f = 0.2$ we find the scenario shown in Fig. 2 (a). Herein the right traveling wave nearly covers the whole subdomain $[\bar{x}_l, \bar{x}_r]$ forming a so-called filled state [75]. Increasing the group velocity to $f = 0.6$ leads to a shrinking of the TW domain. This so-called confined state is shown in Fig. 2(b).

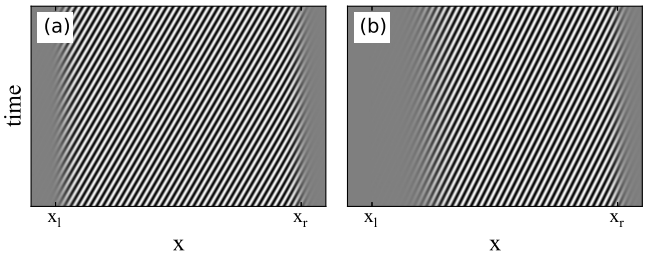

FIG. 2. The time evolution of the real part $\mathrm{Re}(u(x,t))$ of the traveling wave solution of Eq. (1) is shown for a drop width $\delta/\lambda_0 = 1$ and the parameter value $f = 0.2$ in (a) and $f = 0.6$ in (b). Obviously the beginning of the finite amplitude range of RTW shifts to the right when increasing the group velocity.

Even if the solutions shown in Fig. 2 resemble pure right traveling waves, they also include contributions of a left TW with a much smaller magnitude. To depict this, we separate the left and right moving contributions to the full solution $\mathrm{Re}(u(x,t))$. This gives access to the spatially varying envelopes

$$A_{r,l}^{CSH}(x) = e^{-i(\pm q_0 x+\omega t)}u(x,t)\,, \qquad (10)$$

which are the amplitudes of the right and left TW that constitute $\mathrm{Re}(u(x,t))$. Fig. 3 shows the modulus of these spatially varying envelopes for the two different values $f = 0.2$ and $f = 0.6$. Part (a) in Fig. 3 thereby confirms

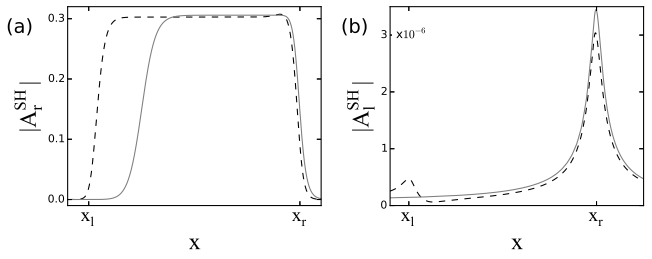

FIG. 3. Part (a) shows $|A_r^{SH}|$ the dominant RTW contribution to the whole solutions $\mathrm{Re}(u(x,t))$ in in Fig. 2 for the same values $f = 0.2$ (dashed line) and $f = 0.6$ (solid line). Part (b) shows $|A_l^{SH}|$ of reflected left traveling wave contribution for $f = 0.2$ (dashed line) and $f = 0.6$ (solid line), respectively.

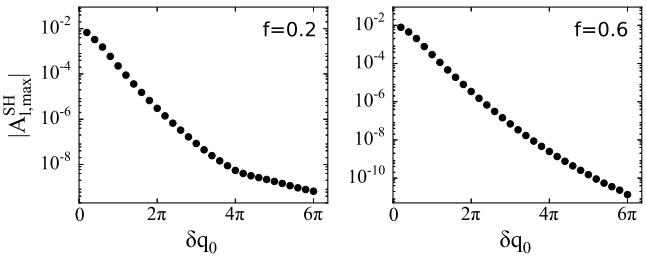

FIG. 4. The maximal value of the spatially varying modulus $|A_l^{SH}(x)|$ of the reflection induced left traveling wave decreases as function of the drop width δ as shown for $f = 0.2$ and $f = 0.6$.

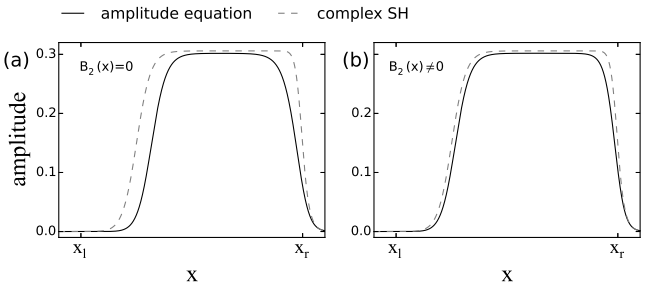

FIG. 5. The envelope $|A_r^{SH}|$ (dashed) of the RTW solution of CSH model (1) is compared with $|A_r|$ obtained by simulations of Eqs. (8) for $f = 0.6$ and $\delta/\lambda_0 = 1$. In (a) the nonadiabatic contribution $B_2(x)$ to Eqs. (8) was neglected, but taken into account in part (b). The inclusion of $B_2(x)$ leads to a much better agreement between the solution of CSH model and the coupled amplitude equations in Eq. (8). Most important, if $B_2(x)$ is neglected the reflection of A_r and the excitation of A_l vanishes, i.e. the two equations (8) decouple.

the expectations gained from looking at the space-time diagrams in Fig. 2: The amplitude of the right moving TW is dominant and their left flank shifts to the right with increasing group velocity. However, part (b) in Fig. 3 reveals that in both cases a left TW of a small magnitude occurs near the right control parameter drop at $x = x_r$. For $f = 0.2$ this is also the case at the left control parameter drop, while this is no longer true for $f = 0.6$.

The emergence of a finite amplitude left moving TW is at first glance rather surprising, since the starting condition is $A_r \neq 0$, $A_l = 0$, i.e. a right moving TW. This right moving TW - at least in extended systems - suppresses any left moving waves via nonlinear competition. Looking at the amplitude equations (8), the left TW is excited via the local contribution $B_2(x)A_r$ in the dynamical equation (8b). This implies that A_l only becomes finite where both A_r and $B_2(x)$ are finite. The coefficient $B_2(x)$ thereby is finite in the vicinity of $x = \bar{x}_l$ or $x = \bar{x}_r$ for a small width of control parameter drops $\delta = \lambda_0$.

For such δ and $f = 0.2$ also A_r is finite at both control parameter drops x_l and x_r. This means at both control parameter drops that the right moving wave induces a left moving one (see Fig. 3(b)). This is a difference to 'regular' reflection with the boundary condition $A_r, A_l = 0$ at $x_{l,r}$ in Ref. [75]. In the case of control parameter drops considered in this work, the right TW is already finite at x_l, cf. dashed line in Fig. 3(a). Therefore, the resonant contribution $B_2^*(x)A_r(x)$ in Eq. (8b) can already excite a left TW at x_l. For $f = 0.6$ the amplitude of A_r at $x = x_l$ and therefore also no left TW is exited via B_2^l. Fig. 4 shows the maximum amplitude of the resonance induced left moving wave at $x = x_r$ as a function of the steepness of the control parameter drop δ. Since the local resonance contribution B_2 decreases with increasing drop width δ, also the magnitude of the resonance induced left TW does. Thereby the group velocity only has a minor impact on the amplitude of the resonance induced left moving wave. Fig. 5 shows the relevance of $B_2(x)$ in the scope of a amplitude equation. This figure compares the solutions of the full system to the amplitude equation neglecting the contribution B_2 in part (a) and taking it into account in part (b). Taking $B_2(x)$ into account leads to a much better agreement between the CSH equation and its amplitude equation. This means that the local resonance contribution $B_2(x)$ is crucial for the resulting pattern.

The dependence of the wave pattern on the group velocity can be understood as follows: In the case of finite values of the group velocity and a supercritical control parameter, small local perturbations evolve into nonlinear wave patterns in a frame comoving with the pattern. In our case, the initial condition around x_l is a right TW. For small group velocity this wave pattern is only slightly transported and the local growth of the pattern can outweigh its transport away from x_l, i. e. the pattern fills the whole area in the case of a supercritical control parameter. Increasing the group velocity a perturbation around x_l is transported faster away to the right and than the pattern is growing locally, i.e. the pattern grows only in the comoving frame . This means a larger group velocity shifts the pattern to the right, leading to confined nonlinear states as indicated in Fig. 2.(b)

B. Patterns for large group velocities

In extended systems for the CSH model the convective instability occurs in the range $f \gtrsim 0.62$ for $\varepsilon = 0.1$. In this case and for smooth boundaries (or large values of δ) we observe no traveling waves anymore in the range $[x_l, x_r]$. Surprisingly crossing the boarder to convective instability does not cause the pattern to vanish in the presence of a rather steep control parameter drop. Instead it first leads to time-dependent amplitudes shown in Fig. 6. Even if A_r is dominant in that case we also see a non vanishing left TW. Moreover, the amplitudes now are time dependent. While A_l rises and decays completely, the tail of the right moving wave breathes back and forth. According to a similar phenomenon described in Ref. [75] we call this a blinking state. Raising f and

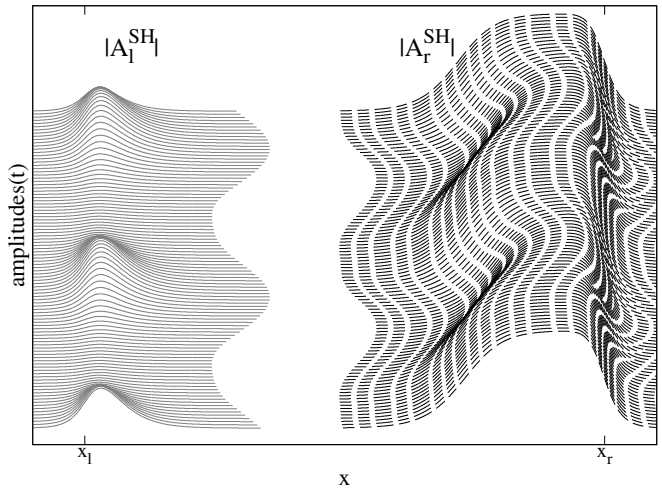

FIG. 6. A so-called blinking state with a time-dependent modulus $|A_r^{SH}(x,t)|$ of the right traveling and that of the left traveling wave $|A_l^{SH}(x,t)|$ is shown for $f = 0.7 > f_c$.

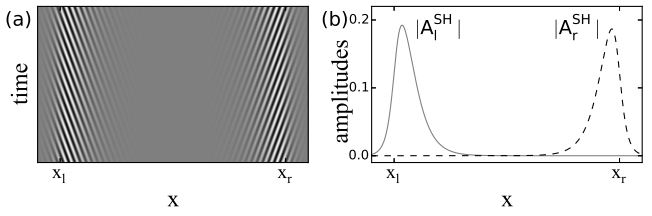

FIG. 7. Part (a) shows the real part of $\mathrm{Re}(u(x,t))$ for a rather large group velocity, i. e. $f = 0.8 > f_c$, with a localized RTW near x_r and a localized LTW near x_l. Part (b) shows the corresponding localized modulus $|A_r^{SH}|$ ($|A_l^{SH}|$) of the localized RTW (LTW).

therefore v_g even further, this leads to a return of stationary amplitudes, but now both left and right moving waves coexist as indicated in Fig. 7. The right moving wave is still located at the right part of the supercritical region whereby the left moving wave is on the left. We call this a counter-propagating wave state.

Note that the relative amplitudes of the two counter propagating waves do not have to be equal. They can be tuned by adjusting the group velocity from $|A_r| > |A_l|$ to the opposite case.
Both blinking and counter propagating wave states can be qualitatively understood by the interplay of convective instability and resonance induced reflection. In the range where these states appear, the group velocity is very high. This means initial right moving TW is shifted to the right half of the overcritical range $[x_l, x_r]$. At the right control parameter drop x_r this right moving wave induces a left moving wave via resonance effects (see previous section). This resonance induced left moving wave now is also transported with the group velocity. Thereby the left moving wave gets advected into the left half of the overcritical region. There the amplitude of the right moving wave is small, i.e. there is no competing right moving wave that suppresses the left moving one. In contrast to confined states the left moving wave can now freely grow in the neighborhood of the left control parameter drop. This results in a pattern with amplitudes of both left and right moving waves.

C. Phase diagram in the $\delta - v_g$ plane

The blinking and the counter propagating wave states appear via an interplay of the resonance induced reflection of an incoming wave at the control parameter drop on the one hand and the convective instability in a finite system on the other. Since the coefficient B_2, that captures the reflection effect in the scope of an amplitude equation, depends on the steepness of the control parameter drop, also the drop width δ is a crucial parameter for those states.

For a more quantitative view the different scenarios are depicted in a phase diagram in the $\delta - f$-plane Fig. 8.

This figure contains a border in the range $f \in [0.6; 0.65]$ and independent of δ. This range inclues the boarder separating absolute instability for smaller f and the convective instability for larger ones. This is still true for larger values of $\delta > \delta_c \approx 3.3\pi$, i.e. for adiabatically varying control parameters. But for smaller values of δ and accordingly sharper changes of the control parameter the resonance due to the non-adiabatic contributions to the control parameter drop come into play. In this case also time dependent blinking states and counter propagating waves occur. The parameter region where these new states exist clearly depends on δ. Decreasing the value of δ lead to a larger region of both blinking and counter propagating wave states. Raising δ seems first to let the blinking states vanish before at $\delta > \delta_c$ also the counter propagating wave states no longer occur.

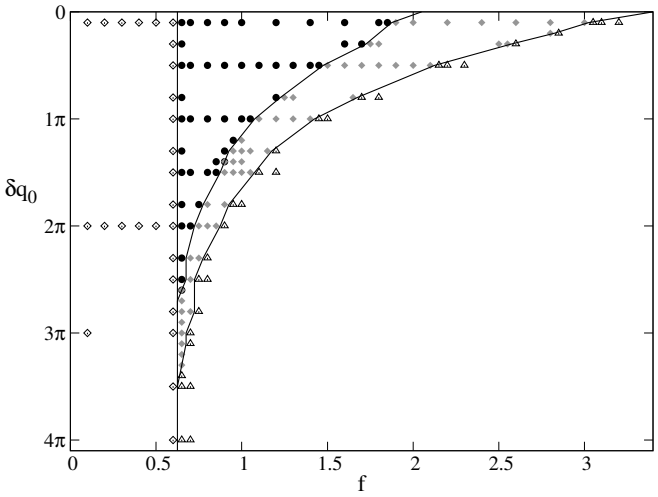

FIG. 8. The different nonlinear wave states shown in previous figures are found besides the basic state $u = 0$ (triangles) in the following ranges in the δ-f-plane: Filled or confined traveling wave states (non-filled diamonds), blinking states (filled circles) and counter propagating wave states (grey diamonds).

IV. DISCUSSION AND CONCLUSION

We investigated the behavior of traveling wave patterns within the complex Swift-Hohenberg (CSH) model and generic amplitude equations in one spatial dimension. We thereby regard a control parameter that is supercritical only in a finite subdomain. At the borders of the subdomain the control parameter drops from super- to subcritical values without imposing boundary conditions for the involved fields. We show, that traveling waves are 'reflected' at steep non-adiabatically varying control parameter drops due to local resonant couplings.

Depending on the value of the control parameter in the supercritical range and the system length, one finds the following scenario for a broad range of parameters. At a low group velocity v_g one finds at first traveling waves filling the whole finite subdomain. Raising the group velocity leads to a v_g-range with confined traveling wave states. Increasing v_g further, so-called blinking states occur. These are composed of left traveling waves localized in the left part and right traveling waves localized in the right part of the subdomain (or vice versa) whereby the width of both is breathing. At even larger values of v_g the interaction between the localized left and right traveling waves becomes weaker and one finds a coexistence between a left traveling wave localized near left end of the subdomain and a right traveling waves localized near the right end (or vice versa). A key to understand these phenomena is the resonant interaction of counter-propagating traveling waves that occurs for sufficiently steep control parameter variations near the ends the supercritical subdomain. A Fourier representation of sufficiently strong control parameter variation include local contributions with twice the wavenumber of the TW patterns. Such local 2:1 resonances induce a local coupling between left and right traveling waves near the domain ends that leads to reflection-like behavior of traveling waves. The resulting nonlinear wave scenarios behave similar as in the case of boundary conditions for the wave field as described in Refs. [74, 75]. However, here traveling wave 'reflection' decays and vanishes for a smooth and adiabatically varying (on the length scale of the wavelength of traveling waves) control parameter.

The results obtained for traveling waves within the CSH model and the generic coupled Ginzburg-Landau equations in the case of spatial variations of the control parameter are also expected for traveling waves in other systems such as for reaction-diffusion models, Min protein patterns [92] or chemical reactions [78, 89, 99, 100]. Even though traveling waves bifurcate in such systems from a more complex basic state, due to symmetry reasons ocalized 2 : 1 resonances between traveling waves and the local spatial control parameter variation will occur as well. Therefore reflection-like effects of traveling wave near control parameter drops as described in this work are also be expected in such systems. A specific example are experiments on Min-protein patterns on extended membranes, which were only reactive in subdomains of the substrate [92, 93]. In this way, the traveling waves are restricted to the range above the functionalized finite subdomain without any imposed lateral boundary conditions.

It is an interesting question whether in-vitro experiments with Min proteins allow for a 'tuning' of the group velocity such that one also observes confined or blinking states. If this is the case one can at this point only speculate for their biological function of such local traveling wave states.

Acknowledgments.- Support by the Elite Study Programm *Biological Physics* is gratefully acknowledged.

[1] P. Ball. *The Self-Made Tapestry: Pattern Formation in Nature*. Oxford Univ. Press, Oxford, 1998.

[2] M. C. Cross and H. Greenside. *Pattern Formation and Dynamics in Nonequilibrium Systems*. Cambridge Univ. Press, Cambridge, 2009.

[3] M. C. Cross and P. C. Hohenberg. Pattern formation outside of equilibrium. *Rev. Mod. Phys.*, 65:851, 1993.

[4] I. Aranson and L. Kramer. The world of the complex Ginzburg–Landau equation. *Rev. Mod. Phys.*, 74:99, 2002.

[5] L. M. Pismen. *Patterns and Interfaces in Dissipative Dynamics*. Springer, Berlin, 2006.

[6] E. Meron. *Nonlinear Physics of Ecosystems*. CRC Press, Boca Raton, Florida, 2015.

[7] S. Kondo and T. Miura. Reaction-diffusion model as a framework for unterstanding biological pattern formation. *Science*, 329:1616, 2010.

[8] D. Walgraef. *Spatio-Temporal Pattern Formation.* Springer, New York, 1997.

[9] V. Eckhaus. *Studies in Nonlinear Stability Theory.* Springer, Berlin, 1965.

[10] L. Kramer and W. Zimmermann. On the Eckhaus instability for spatially periodic patterns. *Physica D*, 16:221, 1985.

[11] M. Lowe and J. P. Gollub. Solitons and the commensurate-incommensurate transition in a convecting nematic fluid. *Phys. Rev. A*, 31:3893, 1985.

[12] W. Zimmermann and L. Kramer. Wavenumber restriction in the buckling instability of a rectangluar plate. *J. Phys. (Paris)*, 46:343, 1985.

[13] H. Riecke and H. G. Paap. Stability and wave-vector restriction of axisymmetric Taylor vortex flow. *Phys. Rev. A*, 33:547, 1986.

[14] M. A. Dominguez-Lerma, D. S. Cannell, and G. Ahlers. Eckhaus boundary and wave-number selection in rotating Couette-Taylor flow. *Phys. Rev. A*, 34:4956, 1986.

[15] B. Janiaud, A. Pumir, D. Bensimon, V. Croquette, H. Richter, and L. Kramer. The Eckhaus instability for traveling waves. *Physica D*, 55:269, 1992.

[16] P. Kolodner. Observations of the eckhaus instability in one-dimensional traveling-wave convection. *Phys. Rev. A*, 46:R1739, 1992.

[17] L. Kramer and P. C. Hohenberg. Effects of boundaries on periodic structures. *Physica D*, 13:352, 1984.

[18] H.S. Greenside and W. M. Coughran. Nonlinear pattern formation near the onset of Rayleigh-Bénard convection. *Phys. Rev. A*, 30:398, 1984.

[19] L. Kramer and H. Riecke. Wavelength selection in Rayleigh–Bénard convection. *Z. Physik B*, 59:245, 1985.

[20] M. C. Cross. Boundary conditions on the envelope function of convective rolls close to onset. *Phys. Fluids*, 25:936, 1982.

[21] K. M. Bajaj, N. Mukolobwiez, N. Currier, and G. Ahlers. Wave number selection and large-scale-flow effects due to a radial of the spacing in Rayleigh-Bnard convection. *Phys. Rev. Lett.*, 83:5282, 1999.

[22] K.-H. Chiam, M. R. Paul, M. C. Cross, and H.S. Greenside. Mean flow and spiral defect chaos in rayleigh-bénard convection. *Phys. Rev. E*, 67:056206, 2003.

[23] M. C. Cross, P. G. Daniels, P. C. Hohenberg, and E. D. Siggia. Phase-winding solutions in a finite container above the convective threshold. *J. Fluid Mech.*, 55:155, 1983.

[24] M. C. Cross. Traveling and standing waves in binary-fluid convection in finite geometries. *Phys. Rev. Lett.*, 57:2935, 1986.

[25] M. C. Cross. Structure of nonlinear traveling-wave states in finite geometries. *Phys. Rev. A*, 38:3593, 1988.

[26] E. Moses, J. Fineberg, and V. Steinberg. Multistability and confined traveling-wave patterns in a convecting binary mixture. *Phys. Rev. A*, 35:2757, 1987.

[27] P. Kolodner and C. M. Surko. Weakly nonlinear traveling-wave convection. *Phys. Rev. Lett.*, 61:842, 1988.

[28] A. B. Rovinsky, A. M. Zhabotinsky, and I. R. Epstein. Target patterns arising from short-wave instability in near-critical regimes of reaction-diffusion systems. *Phys. Rev. E*, 56:2412, 1997.

[29] N. Garnier, A. Chiffaudel, and F. Daviaud. Nonlinear dynamics of waves and modulated waves in 1d thermocapillary flows. II. convective/absolute transitions. *Physica D*, 174:30, 2003.

[30] F. Bergmann, L. Rapp, and W. Zimmermann. Size matters for nonlinear (protein) wave patterns. *New J. Phys.*, 20:072001, 2018.

[31] H. Riecke, J. D. Crawford, and E. Knobloch. Time modulated oscillatory convection. *Phys. Rev. Lett.*, 61:1942, 1988.

[32] D. Walgraef. External forcing of spatio-temporal patterns. *Europhys. Lett.*, 7:485, 1988.

[33] I. Rehberg, S. Rasenat, J. Fineberg, M. de la Torre Juárez, and V. Steinberg. Temporal modulation of traveling waves. *Phys. Rev. Lett.*, 61:2449, 1988.

[34] G. Dangelmayr, E. Knobloch, and M. Wegelin. Dynamics of Traveling Waves in Finite Containers. *Europhys. Lett.*, 16:723, 1991.

[35] G. Dangelmayr and E. Knobloch. Hopf-bifurcation with broken circular symmetry. *Nonlinearity*, 4:399, 1991.

[36] L. Kramer, E. Ben-Jacob, H. Brand, and M. C. Cross. Wavelength selection in systems far from equilibrium. *Phys. Rev. Lett.*, 49:1891, 1982.

[37] M. C. Cross. Wave-number selection by soft boundaries near threshold. *Phys. Rev. A*, 29:391, 1984.

[38] H. Riecke. Pattern Selection by Weakly Pinning Ramps. *Europhys. Lett.*, 2:1, 1986.

[39] L. Rapp, F. Bergmann, and W. Zimmermann. Pattern orientation in finite domains without boundaries. *EPL*, 113:28006, 2016.

[40] A .P. Munuzuri, M. Dolnik, A. M. Zhabotinsky, and I. R. Epstein. Control of the Chlorine Dioxide-Iodine-Malonic Acid Oscillating Reaction by Illumination. *J. Am. Chem. Soc.*, 121:8065, 1999.

[41] M. Dolnik, I. Berenstein, A. M. Zhabotinsky, and I. R. Epstein. Spatial periodic forcing of turing structures. *Phys. Rev. Lett.*, 87:238301, 2001.

[42] J. Schweizer, M. Loose, M. Bonny, K. Kruse, I. Mönch, and P. Schwille. Geometry sensing by self-organized protein patterns. *Proc. Natl. Acad. Sci. USA*, 109:15283, 2012.

[43] T. J. Lagny and P. Bassereau. Bioinspired membrane-based systems for a physical approach of cell organization and dynamics: usefulness and limitations. *Interface Focus*, 5:20150038, 2015.

[44] B. A. Malomed. Nonlinear waves in nonequlibrium systems of the oscillatory type, part I. *Z. Physik B*, 55:241, 1984.

[45] I. Aranson and L. Tsimring. Domain walls in wave patterns. *Phys. Rev. Lett.*, 75:3273, 1995.

[46] L. Gelens and E. Knobloch. Traveling waves and defects in the complex Swift-Hohenberg equation. *Phys. Rev. E*, 84:056203, 2011.

[47] J. B. Swift and P. C. Hohenberg. Hydrodynamic fluctuations at the convective instability. *Phys. Rev. A*, 15:319, 1977.

[48] A. C. Newell. Envelope equations. Lectures in Applied Mathematics, page 157, Providence, RI, 1974. American Math. Soc.

[49] A. M. Zhabotinsky, M. Dolnik, and I. R. Epstein. Pattern formation arising from wave instability in a simple reaction-diffusion systems. *J. Chem. Phys.*, 103:10306, 1995.

[50] M. Dolnik, A. M. Zhabotinsky, A. P. Rovinsky, and I. R.

Epstein. Spatio-temporal pattern in a reaction-diffusion system with wave instability. *Chem. Eng. Sci.*, 55:2023, 2000.

Publication 4

Active phase separation: A universal approach

F. Bergmann, L. Rapp, and W. Zimmermann

Phys. Rev. E **98**, 020603 (2018)
DOI: (10.1103/PhysRevE.98.020603)

Reprinted with permission from the American Physical Society
©2018 American Physical Society

Rapid Communications

Active phase separation: A universal approach

Fabian Bergmann, Lisa Rapp, and Walter Zimmermann*
Theoretische Physik I, Universität Bayreuth, 95440 Bayreuth, Germany

(Received 31 January 2018; revised manuscript received 18 April 2018; published 24 August 2018)

We identify active phase separation as a generic demixing phenomenon in nonequilibrium systems with conservation constraints. Examples range from cell polarization to cell populations communicating via chemotaxis, and from self-propelled particle communities to mussels in ecology. We show that system-spanning properties of active phase separation in nonequilibrium systems near onset are described by the classical Cahn-Hilliard (CH) model. This result is rather surprising since the CH equation is famous as a model for phase separation at thermal equilibrium. We introduce a general reduction scheme to establish a unique mathematical link between the generic CH equation and system-specific models for active phase separation. This approach is exemplarily applied to a model for polarization of cells and a model for chemotactic cell communities. For cell polarization, we also estimate the validity range of the CH model.

DOI: 10.1103/PhysRevE.98.020603

Demixing phenomena in active, nonequilibrium systems currently attract great attention. Examples include cell polarization [1–12], chemotactically communicating cells [13–17], self-propelled particles [18–21], active matter models [22], mixtures of particles with different mobilities [23–26], models of ion-channel densities [27], or mussels in ecology [28]. All of these examples have three properties in common: First, they resemble classic equilibrium phase separation. Second, in contrast to classic phase separation, these are nonequilibrium transitions. Third, they are all subject to conservation constraints. Since these demixing phenomena take place in nonequilibrium systems, we call them *active phase separation*. Their (local) driving mechanisms are as different as the systems themselves. But do these systems nevertheless share fundamental properties described by a generic model? Here we provide a universal framework for the cross-system characteristics of a class of active phase separation phenomena.

A conceptual parallel to this idea are self-organized patterns in nature. Stripe, hexagonal, or traveling wave patterns are driven by mechanisms that are also as diverse as the systems in which they form [29–34]. Nevertheless, periodic patterns in these different nonequilibrium systems share well-known generic properties [33,34]. They are covered by unconserved order-parameter fields that describe the slowly varying amplitude(s) [envelope(s)]. Even though stripe patterns occur in very different systems, the envelope obeys the same fundamental (nonlinear) Ginzburg-Landau equation [33,34]. It can be derived from basic equations and provides the key to understanding the generic properties of stripe patterns [30,34–36].

In this work, we formulate a similar approach for active phase separation in nonequilibrium systems. We present a reduction scheme generalized to conserved order parameters. At leading order, we thereby obtain the Cahn-Hilliard model [37,38] as the generic model for active phase separation in nonequilibrium systems. So far, it has typically been used to model liquid-liquid demixing in thermal equilibrium [37,38]. However, we show here that it also describes the system-spanning properties of phase separation in nonequilibrium. Thus, we manage to capture the essence of active phase separation in very different systems in one universal equation. At the same time we expose the underlying similarities between phase separation in and out of equilibrium. The reduction scheme we present here provides a direct mathematical link between the Cahn-Hilliard (CH) model and system-specific models. It also provides the criteria to identify candidates for this class of active phase separation. Our approach is explicitly demonstrated for two representative examples from living matter: a continuum model for cell polarization and a model for chemotactic cell communities.

Cell polarization is central to processes as diverse as cell motility, differentiation, and cell division [1–10]. The polarized cell has two distinct regions similar to the two phases of a separated liquid-liquid mixture. However, cell polarization in living systems is a nonequilibrium phenomenon driven by *dissipative* processes. The molecules that trigger cell polarization are conserved on the timescales of the self-organization. Models for cell polarization usually involve the nonlinear dynamics of several coupled concentration fields for regulating molecules (see, e.g., [4]). However, minimal models with only two concentration fields for the membrane-cytosol exchange already cover essential properties [5–10]. One concentration field $\tilde{u}(\mathbf{r}, t)$ thereby represents molecules bound to the membrane. The other concentration field $\tilde{v}(\mathbf{r}, t)$ describes molecules in the cytosol. Here, we use

$$\tilde{f}(\tilde{u}, \tilde{v}) = -b\tilde{u} + (\tilde{u} + \tilde{v})^2 - (\tilde{u} + \tilde{v})^3 \tag{1}$$

for the membrane to cytosol exchange in the one-dimensional equations for the fields $\tilde{u}$ and $\tilde{v}$:

$$\partial_t \tilde{u} = D_u \partial_x^2 \tilde{u} + \tilde{f}(\tilde{u}, \tilde{v}), \tag{2a}$$

$$\partial_t \tilde{v} = D_v \partial_x^2 \tilde{v} - \tilde{f}(\tilde{u}, \tilde{v}) \quad \text{(model } P\text{)}. \tag{2b}$$

*Corresponding author: walter.zimmermann@uni-bayreuth.de

 ©2018 American Physical Society

Both fields are coupled via the conservation condition

$$M = \frac{1}{L}\int_0^L [\tilde{u}(x) + \tilde{v}(x)]dx. \tag{3}$$

Another variant of a nonequilibrium phase separation process is clustering of chemotactically communicating cells. They play, for instance, a central role on the route to multicellular fruiting bodies [39]. Here the number of cells is conserved on the timescale of the clustering, but the chemical density field for the cell-cell communication is not [13–17]. We describe a system of chemotactically communicating cells by an extended Keller-Segel model [13–16] with cell density $\tilde{\rho}(\mathbf{r}, t)$ and signal molecule density $\tilde{c}(\mathbf{r}, t)$:

$$\partial_t \tilde{\rho} = \partial_x^2 \tilde{\rho} - s\partial_x\left(\frac{\tilde{\rho}}{1+\beta\tilde{\rho}}\partial_x\tilde{c}\right), \tag{4a}$$

$$\partial_t \tilde{c} = D_c\partial_x^2\tilde{c} + \tilde{\rho} - \tilde{c} \qquad \text{(model } C\text{)}. \tag{4b}$$

Model P in Eqs. (1) and model C in Eqs. (4) have spatially homogeneous solutions u_h, v_h or ρ_h, c_h, respectively. These become unstable beyond critical values of the respective control parameters D_v and s. Immediately above these thresholds, a generic equation can in both cases describe the resulting active phase separation. In the following steps we develop this equation for the conserved order-parameter field.

For both models, we separate the inhomogeneous parts from the basic state, writing $\tilde{u} = u_h + u(x, t)$, etc. We first consider the instability of the homogeneous states with respect to small perturbations. The linear equations in u, v are then solved by the ansatz $u, v = \bar{u}, \bar{v}\exp(\sigma t + iqx)$ (or for ρ and c, respectively). We consider the case when one of two eigenvalues $\sigma_{1,2}$ is always negative close to the onset of phase separation. The other eigenvalue, expanded with respect to powers of q^2, is of the form

$$\sigma = G_2 q^2 - G_4 q^4 + O(q^6) \tag{5}$$

with $G_4 > 0$. The leading order coefficients $G_2^{(P)}$ or $G_2^{(C)}$ include the control parameters D_v and s for models P and C, respectively. The homogeneous solutions become linearly unstable for $G_2 > 0$. $G_2 = 0$ thus defines the critical values of the control parameters:

$$D_v^c = D_u f_v/f_u, \qquad s_c = (\rho_0 h)^{-1}, \tag{6}$$

where $f_{u,v} = \partial_{u,v} f$ and $h = (1 + \beta\rho_0)^{-1}$. As a measure for the distance from the onset of phase separation, we choose the dimensionless control parameter ε, where

$$D_v = D_v^c(1 + \varepsilon), \qquad s = s_c(1 + \varepsilon). \tag{7}$$

Next, we consider the basic equations [cf. Eqs. (2) and (4)] in the range of small ε, i.e., $G_2 \propto \varepsilon$. With $G_4 = O(1)$ the growth rate σ becomes positive in a range of small $q^2 \propto \varepsilon$ and is of the order $\sigma \propto \varepsilon^2$. Therefore, we introduce the "slow" spatial scale $X = \sqrt{\varepsilon}x$ and the timescale $T = \varepsilon^2 t$, which is slower than for periodic patterns [34]. The nonlinear analysis demands the introduction of an additional slow timescale, $T_3 = \varepsilon^{3/2}t$ [40]. This leads to the operator replacements

$$\partial_x \to \sqrt{\varepsilon}\partial_X, \qquad \partial_t \to \varepsilon^{3/2}\partial_{T_3} + \varepsilon^2\partial_T. \tag{8}$$

In compact matrix form, Eqs. (2) and (4) are

$$\partial_t \mathbf{w} = \mathcal{L}\mathbf{w} + \mathbf{N}, \tag{9}$$

with the respective vectors $\mathbf{w} = (u, v)$ and $\mathbf{w} = (\rho, c)$. The right-hand side includes a linear part $\mathcal{L}\mathbf{w}$ and the nonlinear part $\mathbf{N}$. For both models we expand $\mathbf{w}$ in orders of $\varepsilon^{1/2}$:

$$\mathbf{w} = \varepsilon^{1/2}\mathbf{w}_1 + \varepsilon\mathbf{w}_2 + \varepsilon^{3/2}\mathbf{w}_3 + O(\varepsilon^2), \tag{10}$$

leading to

$$\mathcal{L} = \mathcal{L}_0 + (\varepsilon\mathcal{L}_1 + \varepsilon^2\mathcal{L}_2)\partial_X^2 + O(\varepsilon^3), \tag{11}$$

$$\mathbf{N} = \varepsilon\mathbf{N}_2 + \varepsilon^{3/2}\mathbf{N}_3 + \varepsilon^2\mathbf{N}_4 + \varepsilon^{5/2}\mathbf{N}_5 + O(\varepsilon^3). \tag{12}$$

Inserting the new scalings and expansions into Eq. (9) requires a sorting of the basic equations up to two orders higher in $\varepsilon^{1/2}$ than for common spatial patterns [34]:

$$\varepsilon^{1/2} : \mathcal{L}_0\mathbf{w}_1 = 0, \tag{13a}$$

$$\varepsilon : \mathcal{L}_0\mathbf{w}_2 = -\mathbf{N}_2, \tag{13b}$$

$$\varepsilon^{3/2} : \mathcal{L}_0\mathbf{w}_3 = -\mathcal{L}_1\partial_X^2\mathbf{w}_1 - \mathbf{N}_3, \tag{13c}$$

$$\varepsilon^2 : \mathcal{L}_0\mathbf{w}_4 = \partial_{T_3}\mathbf{w}_1 - \mathcal{L}_1\partial_X^2\mathbf{w}_2 - \mathbf{N}_4, \tag{13d}$$

$$\varepsilon^{5/2} : \mathcal{L}_0\mathbf{w}_5 = \partial_{T_3}\mathbf{w}_2 + \partial_T\mathbf{w}_1 - \mathcal{L}_1\partial_X^2\mathbf{w}_3 - \mathcal{L}_2\partial_X^2\mathbf{w}_1 - \mathbf{N}_5. \tag{13e}$$

For model P, we find at order $\varepsilon^{1/2}$ [41]

$$\mathbf{w_1} = \tilde{A}(X, T)\begin{pmatrix} f_v \\ -f_u \end{pmatrix}. \tag{14}$$

Note that in contrast to the Ginzburg-Landau equation for stripes, $\tilde{A}(X, T)$ in our case is not the envelope of an underyling small-scale structure. An iterative solution of the hierarchy, Eqs. (13), leads to a dynamical equation for $\tilde{A}$ via Fredholm alternatives at orders ε^2 and $\varepsilon^{5/2}$ [34]. After returning to the original coordinates x and t, and rescaling the amplitude $A = \sqrt{\varepsilon}\tilde{A}$, it takes the following form:

$$\partial_t A = -\partial_x^2\left[\alpha_1\varepsilon A + \alpha_2\partial_x^2 A - \alpha_3 A^2 - \alpha_4 A^3\right]. \tag{15}$$

This is the Cahn-Hilliard model in one dimension [37] with a quadratic nonlinearity $\propto A^2$ (where $\alpha_1, \alpha_2, \alpha_4 > 0$). It corresponds to nonsymmetric mixtures of two liquids at thermal equilibrium. Equation (15) covers the approximate dispersion relation of the full model in Eq. (5) and nonlinearities up to third order in A. The derivation of the CH equation via the introduced reduction scheme automatically provides a mathematical link to the model for cell polarization in Eqs. (2). That is, the coefficients α_i are expressed by the parameters of the full model:

$$\alpha_1 = D_u f_v/b, \qquad \alpha_2 = D_u^2 f_v/(b f_u), \tag{16a}$$

$$\alpha_3 = D_u b(3M - 1)/f_u, \qquad \alpha_4 = D_u b^2/f_u, \tag{16b}$$

with $f_u = -3M^2 + 2M - b$ and $f_v = -3M^2 + 2M$.

By application of the reduction scheme, the chemotaxis model C reduces to a similar equation for the density variation

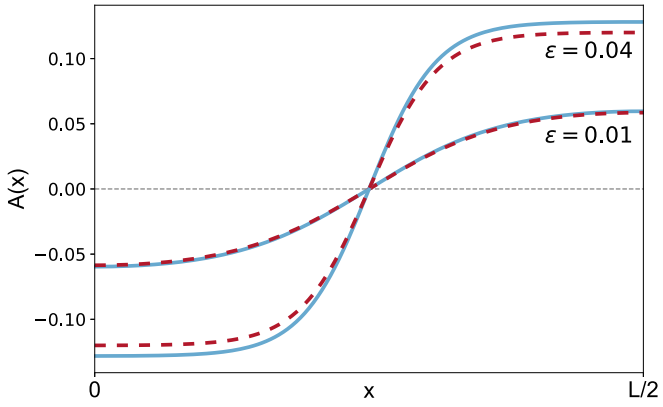

FIG. 1. Steady-state profiles $A(x)$ in the symmetric case ($M = 1/3$): Comparison of model P, Eqs. (2) (solid lines), to the corresponding solutions of the reduced CH model, Eq. (15) (dashed lines), for two values of the control parameter $\varepsilon = 0.01, 0.04$.

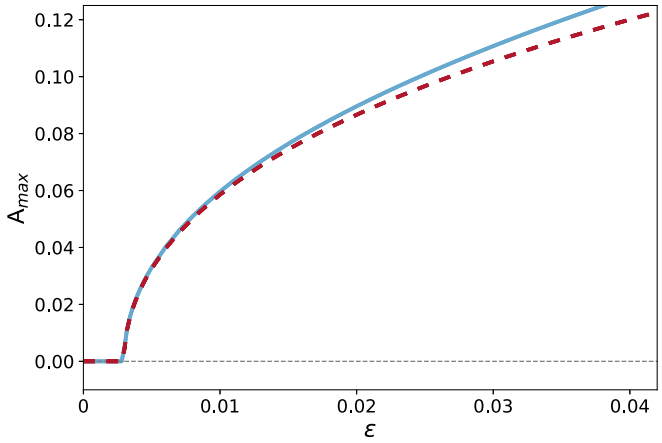

FIG. 2. Plateau values of the steady-state solutions in the symmetric case ($M = 1/3$): Comparison of model P, Eqs. (2) (solid line), to the corresponding values of the reduced CH model, Eq. (15) (dashed line), as a function of the control parameter ε.

ρ, but with different coefficients [41]:

$$\partial_t \rho = -\partial_x^2\left[\varepsilon\rho + D_c\partial_x^2\rho + \tfrac{1}{2}s_c h^2\rho^2 - \tfrac{1}{3}s_c\beta h^3\rho^3\right]. \quad (17)$$

Note that the chemical signal c follows the cell density adiabatically.

The reduced models, Eqs. (15) and (17), capture the dynamics of the respective slow mode of phase separation [34]. Both CH models follow potential dynamics [38] even though the full Eqs. (2) and (4) do not. These qualities are a direct parallel to stripe patterns and their representation via the universal Ginzburg-Landau equation [30,34–36]. Thus, similar to the amplitude equation for stripes, we expect the CH model to play a generic role for active phase separation. Note that the reduced CH models, Eqs. (15) and (17), describe the behavior of a *conserved order parameter*—a reflection of the conservation constraints placed upon the original models P and C. The reduced models certainly cover the behavior of the full system near the (supercritical or weakly subcritical) bifurcation point. But in which parameter range further from the onset of phase separation does this agreement prevail? We will explore this by comparison of stationary solutions for the cell polarization model [cf. Eqs. (2)] and its approximation by the CH model in Eq. (15). We first study the special case $M = 1/3$, i.e., $\alpha_3 = 0$ and $\pm$ symmetry of Eq. (15). This corresponds to the classic CH model [37]. For this case we compare in Fig. 1 steady-state solutions of the full model P to those of the related CH model for two different control parameter values ε (see Supplemental Material [41] for details on simulation methods). Due to the $\pm$ symmetry in Eq. (15), the maximum and minimum of these profiles have the same absolute value. According to the conservation condition, the two phases with increased or decreased concentration each occupy half the system. With respect to both properties, the CH model covers the behavior of the full model. With increasing ε, the plateau values of the steady-state profiles increase and the coherence length decreases. Consequently, the profiles in Fig. 1 evolve toward a more steplike form. Note that in Figs. 1–5, the amplitude for the full model is calculated from the field v. The amplitude for u resembles the amplitude A from Eq. (15) even more closely.

Figure 2 shows the plateau values of the steady-state solutions as a function of ε. It thereby illustrates the validity range of the CH model—including the perfect agreement at onset, and the expected increasing deviations with increasing ε. Figure 2 also illustrates that the transition to active phase separation in the symmetric case occurs in a supercritical bifurcation. Note that the finite system size shifts the onset of phase separation to a positive value $\varepsilon_c = \alpha_2\pi^2/(L^2\alpha_1)$ ($=0.00296$ for the chosen parameters).

For $M \neq 1/3$, the quadratic term in Eq. (15) is finite. This leads to asymmetric phase separation, where the concentration deviates asymmetrically from its mean value. An example of this scenario is shown in Fig. 3 for $M = 0.3$. This corresponds to a small asymmetry parameter $\alpha_3/\sqrt{\alpha_4} \simeq 0.055$. In this case, Eq. (15) captures the behavior of the full model very well. A comparison between the CH equation and the full model as a function of ε is presented in Fig. 4. In the presence of A^2, the bifurcation from the homogeneous state

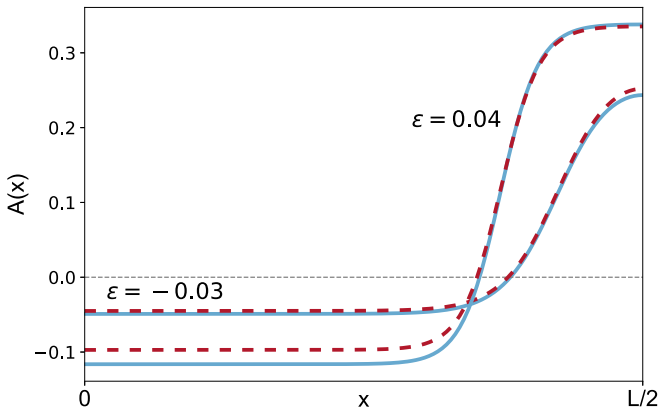

FIG. 3. Similar as in Fig. 1, but in the asymmetric case ($M = 0.3$), i.e., with the A^2 contribution in Eq. (15). Steady-state profiles of model P, Eqs. (2) (solid lines), compared to the corresponding solutions of the reduced CH model, Eq. (15) (dashed lines), for two values of the control parameter $\varepsilon = -0.03, 0.04$.

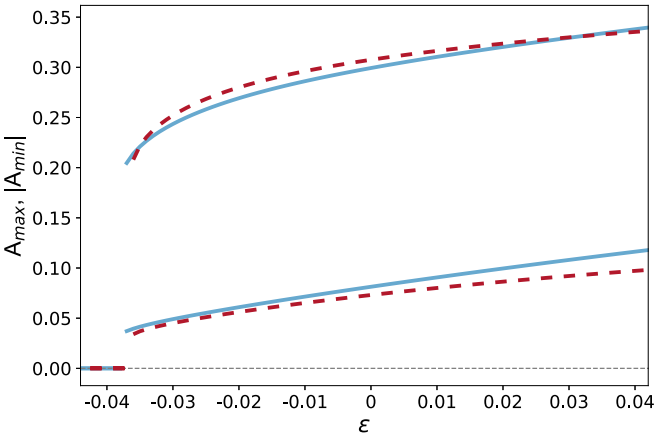

FIG. 4. Similar as in Fig. 2, but in the asymmetric case ($M = 0.3$). Upper and modulus of the lower plateau values of model P, Eqs. (2) (solid lines), compared to the corresponding values of the reduced CH model, Eq. (15) (dashed lines), as a function of the control parameter ε.

to phase separation is subcritical. That is, we find a jump from $A = 0$ to finite plateau values. Moreover, we observe the phase-separated state already for subcritical control parameter values. If the asymmetry parameter $\alpha_3/\sqrt{\alpha_4}$ is of $O(\sqrt{\varepsilon})$, both nonlinear terms in Eq. (15) are of the same order. As Fig. 5 shows, the reduced CH model is a good representation of the full model up to these moderate asymmetries. For stronger asymmetries, however, the full model may deviate strongly from its approximation [41]. That is, the full model may exhibit either for strong asymmetries or for large values of ε its own nongeneric "dialect" of active phase separation.

In this work, we identify a generic, system-spanning behavior for a number of very different demixing phenomena in active and living systems—a class of active phase separation. We have shown that this nonequilibrium transition is at leading order described by the CH equation [37,38]—the same equation that usually describes phase separation at thermal equilibrium. All models in this class have three central

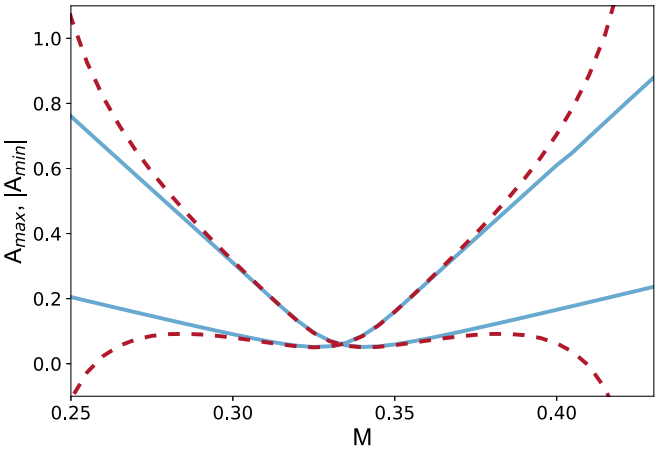

FIG. 5. Upper and modulus of the lower plateau values of the full (dashed lines) vs reduced model (solid lines) as a function of the asymmetry parameter M at a fixed control parameter value $\varepsilon = 0.01$.

properties in common: First, the slow mode growing out of a homogeneous basic state is conserved. Second, the slow mode follows the dispersion relation in Eq. (5). Third, nonlinearities up to third order in the order-parameter fields are sufficient near onset of active phase separation. These conditions ensure the correct signs of the coefficients α_i in the CH equation, Eq. (15). Furthermore, we introduced a perturbative reduction scheme that allows a direct derivation of the CH equation from system-specific nonequilibrium models. With this mathematical link, we can also determine the system-specific values of the coefficients in the CH model. This even allows for a quantitative comparison between the CH model and the original model equations. Note that the derived CH model follows potential dynamics [38], even though the system-specific equations—as the starting point of the reduction—are nonpotential systems.

We verified our generic approach by applying it explicitly to two active matter systems: a minimal model of cell polarization and a model for clustering in chemotactic cell communities. We found a convincing validity range of the generic CH equation as a representation of a cell polarization model near onset. Beyond the system-specific validity range of the CH model further interesting individual "dialects" of active phase separation may come into play. These include, for instance, the effects of higher-order nonlinearities covered by the full system-specific models. The so-called "active model B," for example, was recently introduced for modeling the nonequilibrium phenomenon "motility-induced phase separation' (MIPS) by a single mean field [42,43]. It includes the higher-order nonlinearity $\Delta[\nabla A(\mathbf{r})]^2 \propto \varepsilon^3$. This additional contribution renders the active model B nonintegrable [42] (see Supplemental Material [41] for a more detailed discussion of integrability with higher-order nonlinearities). However, this higher-order contribution becomes negligible near the onset of active phase separation, i.e., the validity range of the generic CH model. For some systems, fluctuations may also become relevant—especially for the coarsening dynamics in low spatial dimensions. This is similar to coarsening in equilibrium phase separation [38].

Our work also suggests the universality of phase separation processes—whether in or out of equilibrium. Their shared characteristics at leading order are reflected in the joint representation by the CH model. Our insights justify the recent usage of the CH equation as a phenomenological model for the clustering phenomenon observed for mussels [28] and further nonequilibrium demixing phenomena.

We expect our generic reduction to the CH model to work for further systems showing active phase separation. These include active colloids [18,21,43], active matter systems [22], or ion channels [27]. We anticipate these systems to also show the fingerprints of the class of active phase separation we introduced here for systems with a conserved order parameter. In this sense, our results are a conceptual parallel to the Ginzburg-Landau equation for an unconserved order parameter [30,34–36], which captures the essence of nonequilibrium stripe patterns near onset and also follows potential dynamics.

Our generic approach is a starting point for further investigations of nonequilibrium phenomena in systems with conserved quantities. Possible generalizations are order-parameter

models that also cover systems with more general dispersion relations than in Eq. (5) (see, e.g., Refs. [44,45]) or oscillatory phase separation phenomena.

Support by the Elite Study Program Biological Physics and inspiring exchanges with W. Pesch, I. Rehberg, and M. Weiss are gratefully acknowledged.

[1] D. S. Johnston and J. Ahringer, Cell **141**, 757 (2010).
[2] B. J. Thompson, Development **140**, 13 (2013).
[3] N. W. Goehring and S. W. Grill, Trends Cell Biol. **23**, 72 (2013).
[4] A. Jilkine, A. F. M. Marée, and L. Edelstein-Keshet, Bull. Math. Biol. **69**, 1943 (2007).
[5] M. Otsuji, S. Ishihara, C. Co, K. Kaibuchi, A. Mochizuki, and S. Kuroda, PLoS Comput. Biol. **3**, e108 (2007).
[6] Y. Mori, A. Jilkine, and L. Edelstein-Keshet, Biophys. J. **94**, 3684 (2008).
[7] A. B. Goryachev and A. V. Pokhilko, FEBS Lett. **582**, 1437 (2008).
[8] A. Jilkine and L. Edelstein-Keshet, PLoS Comput. Biol. **7**, e1001121 (2011).
[9] B. Rubinstein, B. D. Slaughter, and R. Li, Phys. Biol. **9**, 045006 (2012).
[10] P. K. Trong, E. M. Nicola, N. W. Goehring, K. V. Kumar, and S. W. Grill, New J. Phys. **16**, 065009 (2014).
[11] S. Alonso and M. Bär, Phys. Biol. **7**, 046012 (2010).
[12] N. W. Goehring, P. K. Trong, J. S. Bois, D. Chowdhury, E. M. Nicola, A. A. Hyman, and S. W. Grill, Science **334**, 1137 (2011).
[13] E. F. Keller and L. A. Segel, J. Theor. Biol. **26**, 399 (1970).
[14] E. F. Keller and L. A. Segel, J. Theor. Biol. **30**, 225 (1971).
[15] M. J. Tindall, P. K. Maini, S. L. Porter, and J. P. Armitage, Bull. Math. Biol. **70**, 1570 (2008).
[16] T. Hillen and K. J. Painter, J. Math. Biol. **58**, 183 (2009).
[17] M. Meyer, L. Schimansky-Geier, and P. Romanczuk, Phys. Rev. E **89**, 022711 (2014).
[18] J. Palacci, S. Sacanna, A. P. Steinberg, D. J. Pine, and P. M. Chaikin, Science **339**, 936 (2013).
[19] I. Buttinoni, J. Bialké, F. Kümmel, H. Löwen, C. Bechinger, and T. Speck, Phys. Rev. Lett. **110**, 238301 (2013).
[20] J. Stenhammar, A. Tiribocchi, R. J. Allen, D. Marenduzzo, and M. E. Cates, Phys. Rev. Lett. **111**, 145702 (2013).
[21] T. Speck, J. Bialké, A. M. Menzel, and H. Löwen, Phys. Rev. Lett. **112**, 218304 (2014).
[22] J. S. Bois, F. Jülicher, and S. W. Grill, Phys. Rev. Lett. **106**, 028103 (2011).
[23] A. Y. Grosberg and J. F. Joanny, Phys. Rev. E **92**, 032118 (2015).
[24] J. Stenhammar, R. Wittkowski, D. Marenduzzo, and M. E. Cates, Phys. Rev. Lett. **114**, 018301 (2015).
[25] S. N. Weber, C. A. Weber, and E. Frey, Phys. Rev. Lett. **116**, 058301 (2016).
[26] J. Smrek and K. Kremer, Phys. Rev. Lett. **118**, 098002 (2017).
[27] P. Fromherz and B. Kaiser, Europhys. Lett. **15**, 313 (1991).
[28] Q.-X. Liu, A. Doelman, V. Rottschäfer, M. de Jager, P. M. J. Herman, M. Rietkerk, and J. van de Koppel, Proc. Natl. Acad. Sci. USA **110**, 11905 (2013).
[29] P. Ball, *The Self-Made Tapestry: Pattern Formation in Nature* (Oxford University Press, Oxford, 1998).
[30] M. C. Cross and H. Greenside, *Pattern Formation and Dynamics in Nonequilibrium Systems* (Cambridge University Press, Cambridge, 2009).
[31] S. Kondo and T. Miura, Science **329**, 1616 (2010).
[32] E. Meron, *Nonlinear Physics of Ecosystems* (CRC Press, Boca Raton, FL, 2015).
[33] I. Aranson and L. Kramer, Rev. Mod. Phys. **74**, 99 (2002).
[34] M. C. Cross and P. C. Hohenberg, Rev. Mod. Phys. **65**, 851 (1993).
[35] A. C. Newell and J. A. Whitehead, J. Fluid Mech. **38**, 279 (1969).
[36] L. A. Segel, J. Fluid Mech. **38**, 203 (1969).
[37] J. W. Cahn and J. E. Hilliard, J. Chem. Phys. **28**, 258 (1958).
[38] A. J. Bray, Adv. Phys. **43**, 357 (1994).
[39] L. Wolpert, *Principles of Development* (Oxford University Press, Oxford, 2002).
[40] The introduction of two timescales is a mathematical necessity to solve the following hierarchy of Eqs. (13). There the solvability condition in the order ε^2 demands the introduction of an additional timescale T_3. In the final Eqs. (15) and (17), this timescale leads to the additional quadratic term compared to the classical Cahn-Hillard model.
[41] See Supplemental Material at http://link.aps.org/supplemental/10.1103/PhysRevE.98.020603 for more detailed calculations, simulation methods, and discussions about strong asymmetries and higher-order nonlinearities.
[42] R. Wittkowski, A. Tiribocchi, J. Stenhammar, R. J. Allen, D. Marenduzzo, and M. E. Cates, Nat. Commun. **5**, 4351 (2013).
[43] M. E. Cates and J. Tailleur, Annu. Rev. Condens. Matter Phys. **6**, 219 (2015).
[44] S. M. Murray and V. Sourjik, Nat. Phys. **13**, 1006 (2017).
[45] F. Meng, D. Matsunaga, and R. Golestanian, Phys. Rev. Lett. **120**, 188101 (2018).

Publication 5

On system-spanning demixing properties of cell polarization

F. Bergmann and W. Zimmermann

PLoS ONE 14(6): e0218328 (2019)
DOI: (10.1371/journal.pone.0218328)

Reprinted without changes under CC-BY 4.0

PLOS ONE

RESEARCH ARTICLE

On system-spanning demixing properties of cell polarization

Fabian Bergmann, Walter Zimmermann*

Theoretische Physik I, Universität Bayreuth, 95440 Bayreuth, Germany

* walter.zimmermann@uni-bayreuth.de

Abstract

A number of mathematical models have been suggested to describe cell polarization in eukaryotic cells. One class of models takes into account that certain proteins are conserved on the time scale of cell polarization and may switch between a fast and a slow diffusing state. We raise the question whether models sharing this design feature can be condensed into one system-spanning model. We show exemplarily for the mass-conserved reaction-diffusion model of Otsuji et al. (Otsuji M et al. (2007) PLoS Comput Biol 3(6):e108) that cell polarization can be classified as active phase separation. This includes a fundamental connection between a number of non-equilibrium demixing phenomena such as cell polarization to phase separation. As shown recently, generic properties of active phase separation close to its onset are described by the Cahn-Hilliard model. By a systematic perturbation analysis we directly map the basic cell polarization model to the universal Cahn-Hilliard model. Comparing the numerical solutions of the polarization model and the Cahn-Hilliard equation also provides the parameter range where the basic cell polarization model behaves like other systems showing active phase separation. Polarization models of the active phase separation type cover essential properties of cell polarization, e.g. the adaptability of cell polarity to the length of growing cells. Our approach highlights how basic principles of pattern formation theory allow the identification of common basic properties in different models for cell polarization.

Check for updates

OPEN ACCESS

Citation: Bergmann F, Zimmermann W (2019) On system-spanning demixing properties of cell polarization. PLoS ONE 14(6): e0218328. https://doi.org/10.1371/journal.pone.0218328

Editor: Jordi Garcia-Ojalvo, Universitat Pompeu Fabra, SPAIN

Received: January 16, 2019

Accepted: May 30, 2019

Published: June 21, 2019

Copyright: © 2019 Bergmann, Zimmermann. This is an open access article distributed under the terms of the Creative Commons Attribution License, which permits unrestricted use, distribution, and reproduction in any medium, provided the original author and source are credited.

Data Availability Statement: All relevant data are within the manuscript; Simulation data can be downloaded from the University of Bayreuth at https://doi.org/10.15495/do_ubt_2019935.

Funding: The authors received no specific funding for this work.

Competing interests: The authors have declared that no competing interests exist.

Introduction

Cell polarization is one of many fascinating self-organized patterns in living systems that has simultaneously an important functionality [1–8]. During the polarization of living cells certain proteins are enriched in the front and back half of the cell [9–22]. This breaks the symmetry of the cell and defines a unique axis. Polarization of cells is therefore crucial for cell locomotion, the orientation of cell divisions in tissues and the formation of organized multicellular structures [9]. But since cell polarization is this crucial for the reliability of biological processes, we address the question whether these different kinds of polarization follow a similar and robust syntax (at least in certain parameter ranges). All examples differ in the participating proteins, the type of interactions and their trigger mechanisms. However, they also have several features in common. Cell polarization occurs on time scales of minutes. On these time

scales degradation or de-novo production of proteins is negligible. Therefore the total amount of the respective proteins is conserved inside the cell [13–20, 22]. Simulations of numerous different mathematical models of such mass-conserved systems often provide similar results, e.g. showing a transition to a globally similar polarization state. Finally, cell polarization with mass-conserved reaction-diffusion models resembles very much a demixing process. However, all cell polarization processes involve the consumption of some kind of mostly chemical energy to perform directed movement, rendering them non-equilibrium phenomena. For this class of non-equilibrium transitions the notion active phase separation was coined recently [23]. This class unites non-equilibrium demixing phenomena that are induced by so-called type II instabilities [3] and fulfill a global (mass) conservation constraint. Apart from cell polarization, examples for active phase separation range from clustering of chemotactically communicating cells [24–28], to self-propelled particles [29–33], patterning in active matter models [34], mixtures of particles with different models of ion-channel densities [35] or mussels in ecology [36]. We showed in Ref. [23] that near onset of active phase separation the Cahn-Hilliard (CH) model [37, 38] is the universal order parameter equation. We demonstrated a related perturbative reduction scheme for two very elementary models. Here we show that mass-conserved reaction diffusion systems with two involved fields belong to the class of systems showing active phase separation. We thereby use the established model for cell polarization introduced by Otsuji et al. [14] as a seminal example. We derive the universal CH equation directly from the established cell polarization model by applying the perturbational expansion introduced in Ref. [23], while also showing their applicability of in the general case. Since the reduction method applies especially close to the onset of cell polarization, we compare the polarization model with the reduced model in this neighborhood. We thereby consider both stationary solutions as well as the dynamics of the cell polarization model and its reduction.

Considering cell polarization as a realization of a universal equation–at least close to its onset—opens a new route to explain why cell polarization is often very similar across many different systems. We thereby especially show and discuss how the dynamics of the Cahn-Hilliard equation offers an explanation for similarities in mass-conserved reaction-diffusion systems. Our results may therefore help to identify and understand collective and universal features such as spontaneous polarization, adaptability to the cell length and robustness of the polarization pattern.

Results and discussion

Cell polarization model

A class of models for cell polarization share the unifying feature of fast and slow diffusing forms of the same type of signal molecules [14–18, 39]. These are for instance different forms of GTPases: an active, membrane-bound and slowly diffusing form $\tilde{u}$, and an inactive and fast diffusing counterpart $\tilde{v}$. The overall number of signal molecules with two different states is conserved on the time scale of cell polarization. In this temporal regime the two states of signal molecules are described by two coupled reaction-diffusion equations for $\tilde{u}, \tilde{v}$ of the following form:

$$\partial_t \tilde{u} = D_u \nabla^2 \tilde{u} + f(\tilde{u}, \tilde{v}) , \tag{1}$$

$$\partial_t \tilde{v} = D_v \nabla^2 \tilde{v} - f(\tilde{u}, \tilde{v}) . \tag{2}$$

The symmetrical reaction term $f(\tilde{u}, \tilde{v})$ with two different signs in both equations reflects the overall conservation of the signal molecules.

Here we exemplarily analyze the model of Otsuji et al. [14, 19], with the reaction term

$$f(\tilde{u},\tilde{v}) = a_1\left(\tilde{v} - \frac{\tilde{u}+\tilde{v}}{(a_2(\tilde{u}+\tilde{v})+1)^2}\right). \tag{3}$$

Note we extend this analysis to arbitrary reaction terms $f(u, v)$ in S1 Appendix. For simplicity reasons we restrict ourselves to one spatial dimension for most parts of the work. In this case the global conservation condition reads

$$N = \frac{1}{L}\int_0^L [\tilde{u}(x)+\tilde{v}(x)]dx\,. \tag{4}$$

The coupled equations in Eqs (1) and (2) have the homogeneous basic solution

$$u_h = \frac{a_2N^2(a_2N+2)}{(a_2N+1)^2}\,, \tag{5}$$

$$v_h = \frac{N}{(a_2N+1)^2}\,. \tag{6}$$

Onset of cell polarization

We first separate the homogeneous parts u_h and v_h from the inhomogeneous parts u and v with

$$\tilde{u} = u_h + u\,, \tag{7}$$

$$\tilde{v} = v_h + v\,. \tag{8}$$

At first we assume small inhomogeneous perturbations $|u|, |v| \ll u_h, v_h$ with respect to the basic state. This allows for a linearization of the basic equations (Eqs (1) and (2)) with respect to small perturbations u, v leading to two coupled equations:

$$\partial_t u = D_u\partial_x^2 u + f_u u + f_v v\,, \tag{9}$$

$$\partial_t v = D_v\partial_x^2 v - f_u u - f_v v\,, \tag{10}$$

with

$$f_u = \partial_u f\Big|_{u=u_h,v=v_h} = \frac{a_1(a_2N-1)}{(a_2N+1)^3}\,, \tag{11}$$

$$f_v = \partial_v f\Big|_{u=u_h,v=v_h} = \frac{a_1a_2N(a_2^2N^2+3a_2N+4)}{(a_2N+1)^3}\,. \tag{12}$$

The two coupled equations in Eqs (9) and (10) are solved by

$$u, v = \bar{u}, \bar{v}\; e^{\sigma t+iqx}\,. \tag{13}$$

The two resulting linear equations for $\bar{u}$ and $\bar{v}$ have a solubility condition leading to a quadratic polynomial for the growth rate σ:

$$\begin{aligned}\sigma^2 \quad &+[(D_u + D_v)q^2 + f_v - f_u]\sigma \\ &+D_u D_v q^4 + (D_u f_v - D_v f_u)q^2 = 0\,.\end{aligned} \tag{14}$$

For positive values of the parameter a_1 in Eq (3) one has $f_v > f_u$. In this case an expansion of the root $\sigma_+(q)$ up to the order q^4 gives

$$\sigma_+ = G_2 q^2 - G_4 q^4 O(q^6)\,, \tag{15}$$

with

$$G_2 = \frac{D_v f_u - D_u f_v}{f_v - f_u}\,, \qquad G_4 = \frac{(D_u - D_v)^2 f_u f_v}{(f_v - f_u)^3}\,. \tag{16}$$

The growth rate $\sigma_+(q)$ becomes positive in a finite range of q, if $G_2 > 0$. Choosing D_v as the control parameter, the homogeneous state loses stability and G_2 becomes positive for

$$D_v > D_v^c = D_u \frac{f_v}{f_u}. \tag{17}$$

This critical value D_v^c marks the onset of cell polarization. We introduce a small quantity ε in order to parameterize the control parameter D_v near its critical value D_v^c:

$$D_v = D_v^c(1 + \varepsilon)\,. \tag{18}$$

At the critical point ($\varepsilon = \varepsilon_c = 0$) the maximum of the growth rate is at $q = 0$ (see Fig 1A). Raising the control parameter ε shifts this maximum to finite values of q. For $\varepsilon > 0$ there is a range $[0 < |q| < q_{\text{right}}]$ with a positive growth rate $\sigma > 0$ (see Fig 1B). In contrast to classical Turing patterns, this range of positive growth rate extends down to $q = 0$, which is a signature of the overall conservation of the two densities $\tilde{u}$ and $\tilde{v}$. Fig 1 additionally shows a comparison of the full dispersion relation (14) and its approximation up to order q^4 in Eq (15).

Derivation of the generic Cahn-Hilliard model

The two concentration fields $u(x, t)$ and $v(x, t)$ are coupled by the conservation law in Eq (4). We show that near the onset of cell polarization the dynamics of both fields can be described

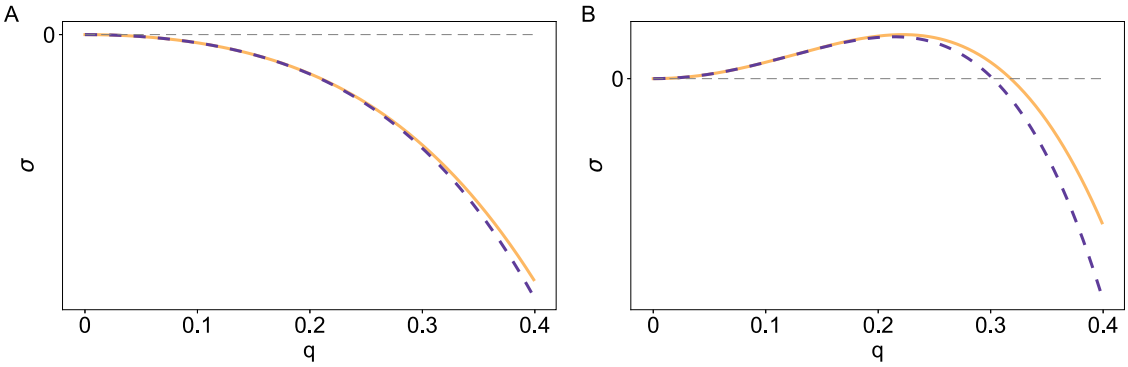

Fig 1. Growth rate σ_+ as a function of the wavenumber q. Comparison between the full solution in Eq (14) (solid line) and its Taylor expansion up to the order q^4 given by Eq (15) (dashed line) at the critical point $\varepsilon = 0$ (A) and slightly above $\varepsilon = 0.1$ (B) (for $a_2 = 2$).

https://doi.org/10.1371/journal.pone.0218328.g001

by only one order parameter field. The dynamical equation for this field is the famous Cahn-Hilliard (CH) model for demixing phenomena at and far from thermal equilibrium (see e.g. [23] and references therein), as we derive in the following. Note, that this is in contrast to a so-called Galerkin method made under the assumption of spatially periodic solutions of the model of Otsuji et al, cf. [19], which we do not find in a wide parameter range around the onset of cell polarization.

We introduce the vector fields $\mathbf{w} = (u, v)$ and $\mathbf{N} = (f(u, v), -f(u, v))$ and rewrite the two coupled Eqs (1) and (2) in terms of the two vector fields in a compact form:

$$\partial_t \mathbf{w} = \mathcal{L}\mathbf{w} + \mathbf{N}\,. \tag{19}$$

Considering again the growth rate in Eq (15), the upper limit of the q-range with positive σ is $q_{max} \propto \sqrt{\varepsilon}$. Therefore, the inhomogeneous parts $u(x, t)$ and $v(x, t)$, cf. Eqs (7) and (8), are slowly varying functions in space. This suggests the introduction of a new spatial scale with $X = \sqrt{\varepsilon}x$ and two slow time scales $T = \varepsilon^2 t$ and $T_3 = \varepsilon^{3/2} t$. These scales lead to the following replacements of the spatial and temporal derivatives:

$$\partial_x \to \sqrt{\varepsilon}\partial_X\,, \tag{20}$$

$$\partial_t \to \varepsilon^{3/2}\partial_{T_3} + \varepsilon^2\partial_T\,. \tag{21}$$

Note that the introduction of two different time scales is necessary to fulfill the solvability condition in the hierarchy of equations following below in Eqs (24), (25), (26), (27) and (28) (see also supplement S1 Appendix for additional information). Here we consider the basic equations (see Eqs (1) and (2)) in the range of small modulations $u, v \sim \sqrt{\varepsilon}$ of the average concentrations u_h and v_h. Accordingly we expand the field $\mathbf{w}$ with respect to the small parameter ε as follows:

$$\mathbf{w} = \varepsilon^{1/2}\mathbf{w_1} + \varepsilon\mathbf{w_2} + \varepsilon^{3/2}\mathbf{w_3} + \varepsilon^2\mathbf{w_4} + \varepsilon^{5/2}\mathbf{w_5} + \dots\,, \tag{22}$$

leading to

$$\mathbf{N} = \varepsilon\mathbf{N_2} + \varepsilon^{3/2}\mathbf{N_3} + \varepsilon^2\mathbf{N_4} + \varepsilon^{5/2}\mathbf{N_5} + \dots. \tag{23}$$

Inserting this expansion of the field $\mathbf{w}$ and the derivatives in Eqs (20) and (21) results in the following ε-hierarchy of equations:

$$\varepsilon^{1/2} : \mathcal{L}_0\mathbf{w}_1 = 0\,, \tag{24}$$

$$\varepsilon : \mathcal{L}_0\mathbf{w}_2 = -\mathbf{N}_2\,, \tag{25}$$

$$\varepsilon^{3/2} : \mathcal{L}_0\mathbf{w}_3 = -\mathcal{L}_1\partial_X^2\mathbf{w}_1 - \mathbf{N}_3\,, \tag{26}$$

$$\varepsilon^2 : \mathcal{L}_0\mathbf{w}_4 = \partial_{T_3}\mathbf{w}_1 - \mathcal{L}_1\partial_X^2\mathbf{w}_2 - \mathbf{N}_4\,, \tag{27}$$

$$\varepsilon^{5/2} : \mathcal{L}_0\mathbf{w}_5 = \partial_{T_3}\mathbf{w}_2 + \partial_T\mathbf{w}_1 - \mathcal{L}_1\partial_X^2\mathbf{w}_3 - \mathcal{L}_2\partial_X^2\mathbf{w}_1 - \mathbf{N}_5\,. \tag{28}$$

Solving the eigenvalue equation in $\mathcal{O}(\sqrt{\varepsilon})$ leads to

$$u_1(x, t) = f_v\tilde{A}(x, t)\,, \qquad v_1(x, t) = -f_u\tilde{A}(x, t)\,. \tag{29}$$

This means the two fields $u_1(x, t)$ and $v_1(x, t)$ are proportional to each other whereby the eigenvector $(f_v, -f_u)^T$ of $\mathcal{L}_0$ is the proportionality factor. With this starting point the hierarchy of Eqs (24), (25), (26), (27) and (28) is solved successively as described in more detail in the supplemental part S1 Appendix. The solubility conditions at the orders ε^2 and $\varepsilon^{5/2}$ provide expressions for $\partial_{T_3}\tilde{A}$ and $\partial_T\tilde{A}$. After reconstituting the original scalings x and t in Eqs (20) and (21) via $\partial_t\tilde{A} = \partial_{T_3}\tilde{A} + \partial_T\tilde{A}$ we obtain an equation for $A(x, t) = \sqrt{\varepsilon}\tilde{A}$. This equation has the form of the Cahn-Hilliard equation [37, 38, 40] with an additional quadratic term:

$$\partial_t A = -\partial_x^2[\gamma_1 \varepsilon A + \gamma_2 \partial_x^2 A - \gamma_3 A^2 - \gamma_4 A^3] \,. \tag{30}$$

The parameters γ_i are determined in terms of the parameters of the starting model in Eqs (1), (2) and (4) as follows:

$$\gamma_1 = \frac{D_u f_v}{a_1} = D_u \frac{a_2 N(a_2^2 N^2 + 3a_2 N + 4)}{(a_2 N + 1)^3} \,, \tag{31}$$

$$\gamma_2 = \frac{D_u^2 f_v}{a_1 f_u} = D_u^2 \frac{a_2 N(a_2^2 N^2 + 3a_2 N + 4)}{a_1(a_2 N - 1)} \,, \tag{32}$$

$$\gamma_3 = \frac{D_u}{f_u}\frac{a_1^2 a_2(a_2 N - 2)}{(a_2 N + 1)^4} = D_u \frac{a_1 a_2(a_2 N - 2)}{1 - a_2^2 N^2} \,, \tag{33}$$

$$\gamma_4 = \frac{D_u}{f_u}\frac{a_2^2 a_1^3(3 - a_2 N)}{(a_2 N + 1)^5} = \frac{D_u a_1^2 a_2^2(3 - a_2 N)}{(a_2 N + 1)(a_2^2 N^2 - 1)} \,. \tag{34}$$

Among the coefficients, γ_1 is always positive. To make the linear part of Eq (30) (considered in Fourier space) capture the approximate dispersion relation given by Eq (15) γ_2 has to be positive, i.e. $a_2 N > 1$. The nonlinear coefficient γ_4 is positive in the range $1 < a_2 N < 3$. In this range the CH model has a cubic limitation term. If γ_4 is negative there is no limiting nonlinearity, i.e. the reduction is no longer valid and would require going to higher orders of ε [23]. In this work we focus on the range of $\gamma_4 > 0$ where cell polarization close to its onset belongs to the universal class of active phase separation [23]. Within this range the coefficient γ_3 changes its sign at $a_2 N = 2$. For $\gamma_3 = 0$ cell polarization is symmetric close to its onset because the CH model in Eq (30) has a $\pm A$-symmetry in this case. In this instance the transition to cell polarization takes place continuously or supercritically in the language of pattern formation [2]. The reduction of the basic model in Eqs (1) and (2) to the CH model thereby allows the important distinction between the parameter ranges where cell polarization takes place continuously or discontinuously. Eq (30) can also be represented by a variational derivative of a related functional

$$\partial_t A = \frac{\partial^2}{\partial x^2}\frac{\delta \mathcal{F}}{\delta A} \,, \tag{35}$$

with

$$\mathcal{F} = \int dx \left(-\frac{\gamma_1 \varepsilon}{2} A^2 + \frac{\gamma_2}{2}(\partial_x A)^2 + \frac{\gamma_3}{3} A^3 + \frac{\gamma_4}{4} A^4 \right) . \tag{36}$$

It is a surprising result that the order parameter field $A(x, t)$ follows the potential dynamics according to Eq (35), because the basic model in Eqs (1) and (2) cannot be derived from a functional even in the range of small ε for which the CH model was derived. However, this

phenomenon is not exclusive to cell polarization. The same relaxation dynamics are also found in other demixing systems showing active phase separation [23]. Moreover, the envelope of spatially periodic patterns in non-equilibrium systems, including spatially periodic Turing patterns, also follow potential dynamics while the dissipative starting equations do not (see e.g. [2, 3] and references therein).

These relaxational dynamics of the solution A of Eq (30) are helpful for further analysis. For instance, Eq (36) allows to estimate the magnitude of piecewise constant solutions with $A \neq 0$. These correspond to the minimum of the functional in Eq (36) with respect to A. For further details of related analytical considerations we refer to part S2 Appendix of the supplementary information. The constant plateau values of opposite signs are

$$A_{\pm} = \frac{-\gamma_3 \pm \sqrt{3\gamma_3^2 + 9\varepsilon\gamma_1\gamma_4}}{3\gamma_4}\,. \tag{37}$$

In the symmetric case, $\gamma_3 = 0$, the Cahn-Hilliard model in Eq (30) has a well known domain wall solution in long systems [38, 40]:

$$A(x) = F\tanh\left(\frac{x}{\xi_0}\right), \tag{38}$$

$$\text{with} \quad \xi_0 = \sqrt{\frac{2\gamma_2}{\gamma_1\varepsilon}} = \sqrt{\frac{2D_u}{\varepsilon f_u}}, \qquad F = \pm\sqrt{\frac{\gamma_1\varepsilon}{\gamma_4}}. \tag{39}$$

The coherence length ξ_0 is a measure for the width of the domain wall, the transition range between the positive and negative plateau values of the hyperbolic tangent. The expression for ξ_0 shows that in the context of cell polarization the width of the transition range depends directly on the diffusion constant of membrane-bound state u and the distance from the onset of cell polarization. This is an important insight found via the reduction to the CH model in Eq (38).

Comparison of solutions of the basic and the Cahn-Hilliard model

In this section we determine numerically the steady state solutions of the basic equations for cell polarization in Eqs (1) and (2) and the CH model in Eq (30) in a finite one-dimensional domain of length L. Additional informations about the simulations can be found in the materials and methods section. By comparing the steady state solutions of both equations we determine in which parameter range the solutions agree qualitatively or even quantitatively. We focus our simulations on the parameter range with a positive coefficient $\gamma_4 > 0$, where cell polarization is limited by a cubic nonlinearity. In the following analysis we therefore keep the parameters $D_u = 0.1$, $a_1 = 3$ and $N = 1$ fixed, while D_v and a_2 will be varied.

Comparison of steady state solutions in the symmetric case $\gamma_3 = 0$. For $\gamma_3 = 0$ the reduced CH model is $\pm A$-symmetric. This is illustrated by the numerical solutions $A(x)$ of the CH model, in Fig 2A (solid lines) for the two control parameter values $\varepsilon = 0.001, 0.01$. Due to the $\pm$-symmetry the solutions of the CH model above the onset of cell polarization show a plateau with increased and a plateau with decreased concentration, each covering exactly half of the system. Increasing the control parameter ε leads to increased plateau values as well as more step-like profiles. This trend is also indicated by the coherence length ξ_0 in Eq (39), which decreases with increasing ε. For $\varepsilon = 0.001$, the cell polarization in the full model is also perfectly symmetric (see Fig 2A, dashed orange line). Additionally the approximation via the CH model matches the results of the full model almost perfectly. Increasing ε to $\varepsilon = 0.01$ leads

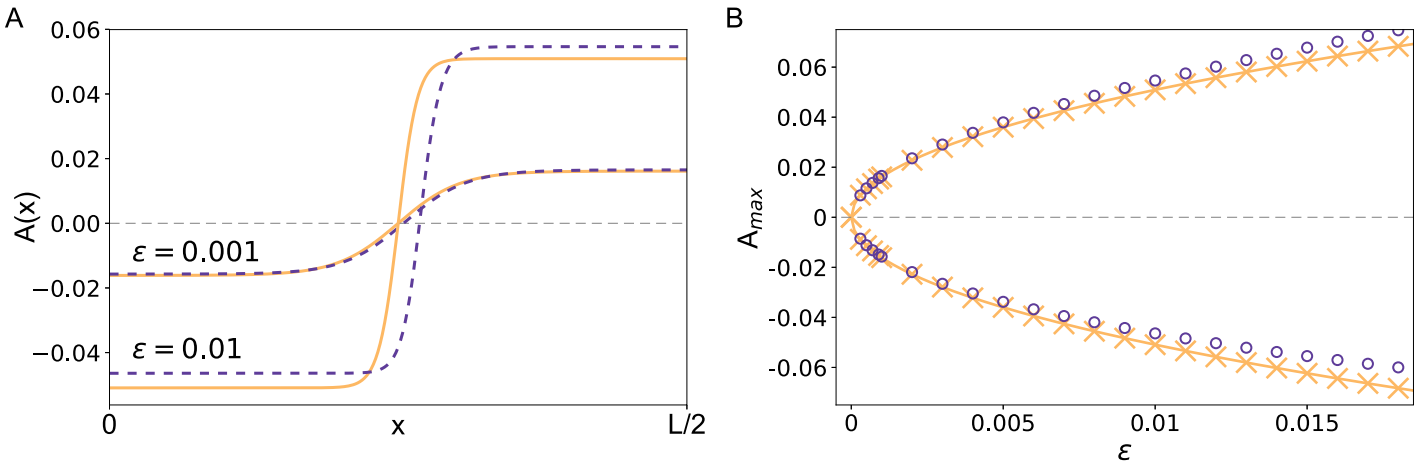

Fig 2. Comparison of steady state solutions of the polarization model and its corresponding CH model in the symmetric case. (A) Steady state profiles for $a_2 = 2$ and two values of $\varepsilon = 0.001$ and $\varepsilon = 0.01$ for the polarization model in Eqs (1) and (2) with $A(x) = (v_h - \tilde{v}(x))/f_u$ (dashed lines) and for the solution $A(x)$ of the CH model in Eq (30) (solid lines). (B) Plateau values of the steady state profiles shown in (A) as function of ε for the basic polarization model (circles) and the CH model (crosses). The solid line shows an analytical approximation for the plateau values in the CH model given by Eq (37).

https://doi.org/10.1371/journal.pone.0218328.g002

to slightly asymmetric polarization in the full model, which can be identified by the off-center shift of the zero-crossing as well as the different magnitude of the plateau values. Since the CH model (for $a_2 = 2$) is ±-symmetric irrespective of ε, the asymmetry in the full model leads to slight deviations between the two.

This means, in the basic model the ±-symmetry is broken with an increasing distance ε from the onset of cell polarization. For the derivation of the CH model only contributions up to cubic order in u and v were taken into account. However, an expansion of the denominator of the function $f(u, v)$ includes also higher terms, such as u^4, v^4, which break the ±-symmetry with increasing ε.

To quantify this symmetry-breaking effect and estimate a validity range of our reduction for $\gamma_3 = 0$, we also compare the plateau values as a function of ε in Fig 2B. Additionally, we approximate the plateau values analytically from the CH model assuming a two plateau solution as in Eq (37). For small values of ε, the simulation results of the polarization and the reduced model as well as the analytical solution match almost perfectly. For larger control parameter values, the system-specific 'dialects' like the increasing asymmetry begin to play a role which leads to deviations between the full model and the CH equation. Moreover, Fig 2 shows that the transition from the homogenous state to the phase-separated state is smooth, i.e. it occurs in a supercritical bifurcation in the parameter range predicted by our perturbation expansion.

Comparison of steady state solutions in the asymmetric case $\gamma_3 \neq 0$. For $\gamma_3 \neq 0$ the ±-symmetry is already broken immediately at onset. Fig 3A therefore shows that the phase with increased concentration takes a smaller fraction of the system than the phase with decreased concentration or vice versa. For small control parameter values the full polarization model and its corresponding CH equation are in good agreement. For larger values of ε the approximation still provides the correct trends but with less predictive power. Comparing the plateau values in Fig 3B and 3D quantifies this validity range. The deviations in the analytical solution compared to the simulations in the range $\varepsilon < 0$ are due to the neglection of the interface energy term in the functional that covers the spatial variations between the plateau values. These become more and more relevant if the control parameter is decreased.

Fig 3D also reveals that the broken symmetry at threshold already changes the character of the onset of cell polarization, i.e. for $a_2 \neq 2$ the bifurcation is no longer smooth. Instead the

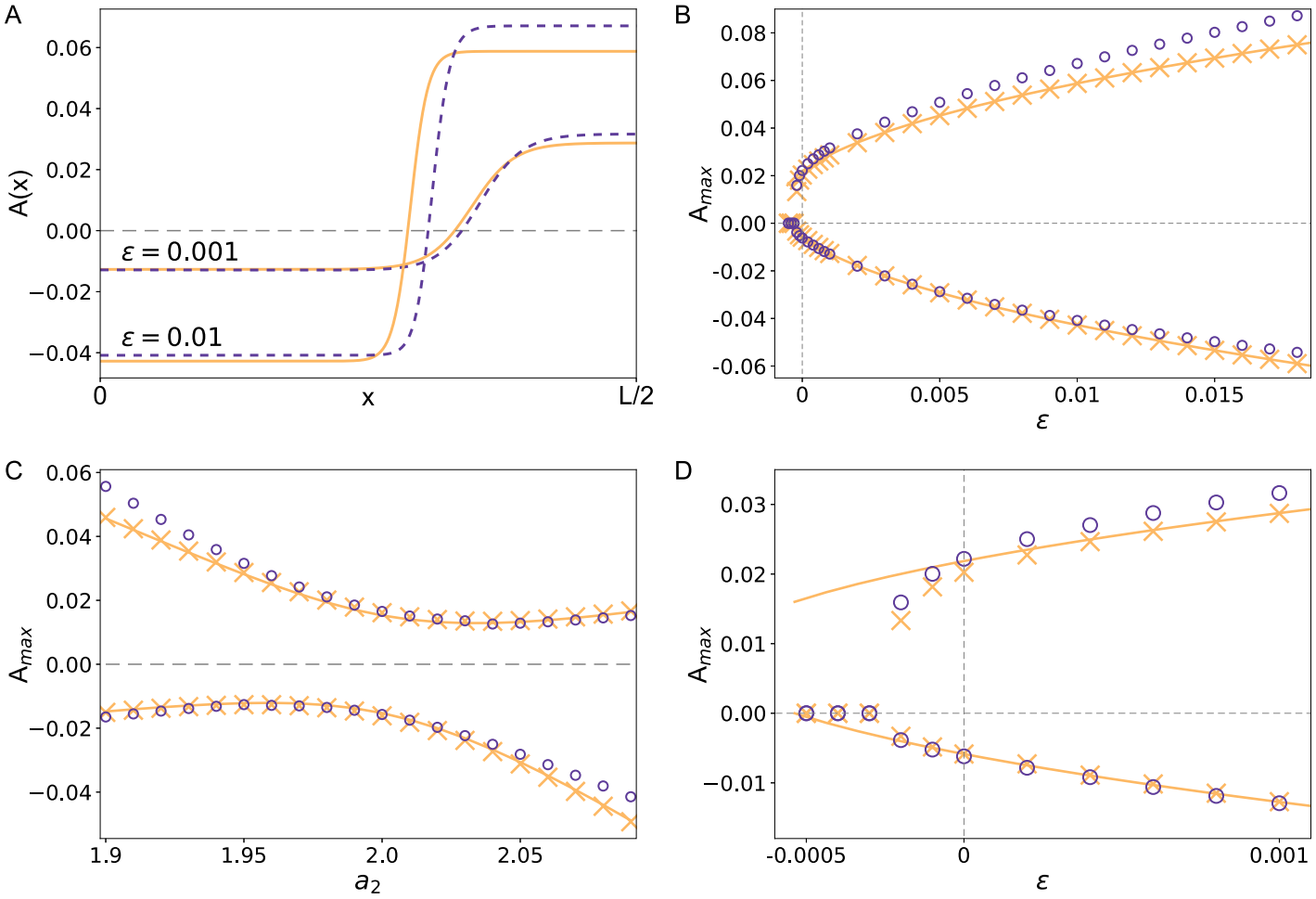

Fig 3. Comparison of steady state solutions of the polarization model and its corresponding CH model in the asymmetric case. (A) Steady state profiles for a_2 $N = 1.95$ and two values of $\varepsilon = 0.001$ and $\varepsilon = 0.01$ for both the basic polarization model in Eqs (1) and (2) with $A(x) = (v_h - \tilde{v}(x))/f_u$ (dashed lines) and the solution $A(x)$ of the CH model in Eq (30) (solid lines). (B), (D) Plateau values of the steady state profiles shown in (A) from simulations of the basic polarization model (purple circles) and the reduced CH model (yellow crosses) as a function of ε. The yellow solid line is an analytical approximation for the plateau values of the CH model given by Eq (37). (D) is a close-up around $\varepsilon = 0$ that shows the subcriticality of the bifurcation. (C) Plateau values of the steady state profiles for simulations of the polarization model (purple circles) and the reduced CH model (yellow crosses) as a function of the asymmetry parameter a_2. The yellow line depicts again an approximation via Eq (37).

https://doi.org/10.1371/journal.pone.0218328.g003

transition of the homogenous basic states to polarization is subcritical (discontinuous). In this case we observe a bistable region where both the polarized and the homogenous state are stable. This also implies a hysteretic behavior if we increase and decrease the control parameter: Starting with a negative ε, the basic state $A = 0$ stays stable until $\varepsilon = 0$. For larger control parameter values we end up in a polarized state. But starting in the polarized state and decreasing the control parameter, the polarized state remains even in a range of negative values of ε.

Fig 3C shows a comparison of the polarization model and the corresponding CH equation as a function of the asymmetry parameter a_2 for fixed control parameter $\varepsilon = 0.001$. While for small asymmetry the agreement is almost perfect, in case of more asymmetric polarization the system specific 'dialects' come into play.

Comparison of dynamics. Apart from the stationary profiles considered in the previews section, we also consider the temporal evolution of the polarization model and its corresponding CH equation. Thereby we distinguish between two different scenarios depending on the

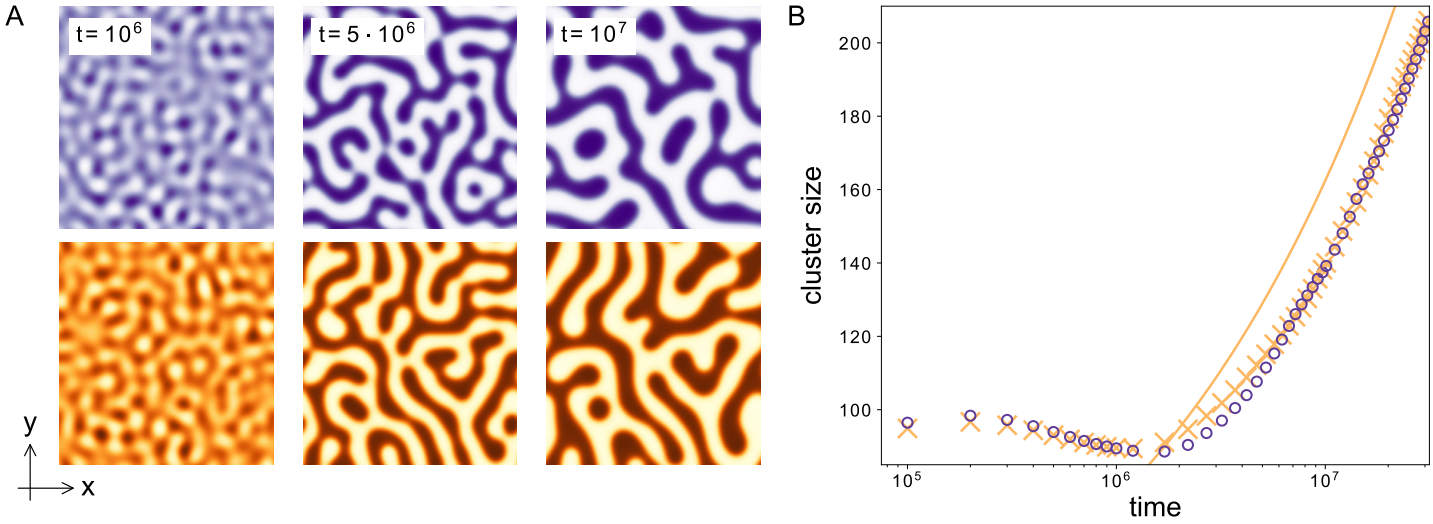

Fig 4. Comparison of the dynamics of the polarization model and its corresponding CH model. (A) 2D snapshots of the full model (upper row, purple) and the corresponding CH model (bottom row, orange) for different times. The Cahn-Hilliard model captures the coarsening dynamics of the full model. (B) Cluster size as a function of time for the polarization model (purple circles) and the corresponding CH model (orange crosses). The solid orange line shows the power law that is expected as a long-term behavior. Parameters: $a_2 = 2$, $\varepsilon = 0.01$.

https://doi.org/10.1371/journal.pone.0218328.g004

system size. To measure the system size we express the wavenumber q_{max} of the fastest growing mode also in terms of the coherence length ξ_0 (see Eq (39))

$$q_{max}^2 = \frac{1}{\xi_0^2} \,. \tag{40}$$

Note that the length scale ξ_0 of the domain wall between the two polar states also determines the preferred mode during onset of cell polarization. In the case of large system sizes $L \gg 2\pi/|q_{max}|$ we compare in Fig 4A the qualitative dynamics of both the polarization model and its corresponding CH model for a fixed set of parameters in 2D. For a control parameter value above the threshold of pattern formation, the homogenous basic state is unstable. This leads to an initial patterned state whose wavelength is dominated by the fastest growing mode q_{max}. But this patterned state is unstable towards perturbations with a larger wavelength, i.e. the system undergoes a coarsening process. Fig 4A shows 2D snapshots of this coarsening process for different times in a quadratic system of length $L = 800$. At every time step the snapshots of the polarization and the CH model show striking similarities. The figure also depicts the visual similarity between the polarization process modeled here and phase separation of e.g. a liquid-liquid mixture [38]. For a quantitative comparison of the full model and the CH model we compare the dominating wavelength over time. We determine the dominating wavelength (or the cluster size in 2D) using the pair correlation function (see also Methods) on simulation results in 2D. We consider 2D simulations instead of 1D as in the previous section due to the scaling expected from the CH equation. The cluster size in this equation scales logarithmically in 1D, i.e. a comparison is computationally very expensive. In 2D, the cluster size is expected to scale with a power law, which is much more convenient. Fig 4B shows a comparison of the dynamics of the polarization model and its corresponding CH model for the symmetric case and $\varepsilon = 0.01$. The CH model captures the dynamics of the full model very well with deviations under 5%. For small times the systems show an interplay between growth of the pattern and the coarsening process which leads to a rather constant cluster size. When the growth process of the amplitudes stops, the dynamics is dominated by coarsening. In this regime the dynamics

of both the polarization and the CH model follow the power law $\propto t^{\frac{1}{3}}$. In the language of the original work of Otsuji et al. [14] this coarsening dynamic in 2D corresponds to the observed instability of multi-peak solutions towards a single peak in 1D. The parameters in the original work correspond to a large value of $\varepsilon \approx 1.8$ and a strongly asymmetric cell polarization leading to a more peak-like profile compared to the step-like profiles shown here (see Figs 2A and 3A). Even if a quantitative comparison between the polarization model and the CH equation is no longer valid in this parameter regime similarities in the qualitative dynamical behavior still prevail: Initially a multi-peak solution develops with a wavenumber q_{max}. However this pattern is unstable and evolves or coarsens into a single peak solution. Our analysis shows that this behavior is no surprise for mass-conserved reaction-diffusion systems but instead generic in systems that can be reduced to the CH equation. Nevertheless for biological cell polarization reaching a polar state trough a coarsening process might be too slow. To therefore avoid a coarsening dynamics nature has to tune the system parameters appropriately. If the system length $L \sim O(2\pi/|q_m|)$, the short system length suppresses any coarsening. This means if the system parameters are such that the width of the transition ξ_0 is of the order of the system length L, like the extension of a cell, we expect a direct transition to a polar state without a complex intermediate temporal behavior like coarsening regimes. Our analysis allows the identification of the parameters D_u, f_u and ε where to expect this direct transition to the polar state from an unstable homogenous basic state:

$$L \approx 2\pi\sqrt{\frac{2D_u}{\varepsilon f_u}}. \tag{41}$$

For the chosen parameters, this is the case for $L \approx 84$. We verify this claim in simulations with a system length $L = 80$ shown in Fig 5. As expected, the average cluster size (see Fig 5B) almost immediately approaches the system size and stays constant from there on. The final state is a fully polar system with one region with increased and one with decreased concentration (see 2D snapshots in Fig 5A). This state corresponds to what is called a single-peak solution in 1D in Ref. [14]. Note, however, that suppressing the coarsening dynamics does not require the system length to fit the condition in Eq (41) perfectly. Since the initially growing wavelength is unstable towards larger wavelengths, the system tends to settle into the largest wavelength, which has also been verified numerically.

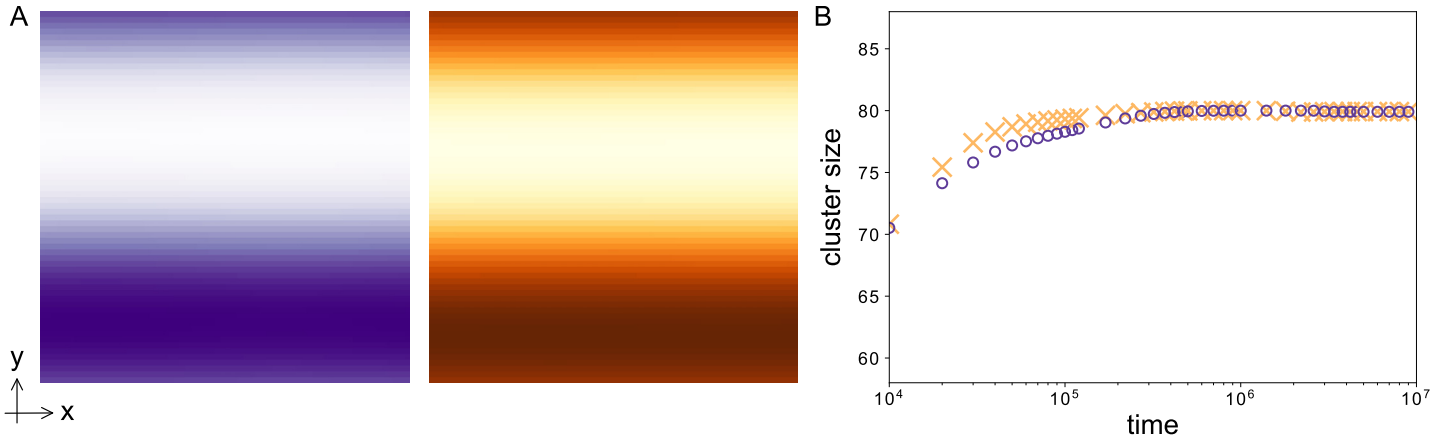

Fig 5. Coarsening is suppressed in small systems. (A) 2D snapshots of the full model (left, purple) and the corresponding CH model (right, orange) for $t = 5 \cdot 10^6$ in a small system ($L = 80$). Both simulations show a fully phase separated (one peak) system. (B) Cluster size as a function of time for the polarization model (purple circles) and the corresponding CH model (orange crosses). The cluster size almost immediately goes to the system size $L = 80$. Parameters: $a_2 = 2, \varepsilon = 0.01$.

https://doi.org/10.1371/journal.pone.0218328.g005

Conclusion

In this work we analyzed the well-known mass-conserved reaction-diffusion model for cell polarization of Otsuji et al. [14] as a representative of a model class from the perspective of pattern formation theory. The model belongs to a class that describes the dynamics of protein molecules that change from a slow diffusing membrane-bound state to a fast diffusing state in the cytosol and vice versa. We showed for this representative how such mass-conserved models comprising several equations can be mapped by a recently introduced method [41] to the single universal Cahn-Hilliard (CH) equation. Additionally, we present an extension to a general mass-conserved reaction- diffusion system of a similar form in S1 Appendix. Our perturbative reduction technique directly connects the parameters of the original cell polarization model to those of the CH equation. Because of this system-specific link between the polarization model and the CH equation, the analytical solution of the latter also become solutions of the original model.

Comparing numerical stationary solutions of the basic model, the CH model and analytical solutions of the CH model reveals a convincing agreement between all three approaches. In a comparison of the dynamics we also found coarsening behavior in large 2D systems. Near onset of cell polarization we find an almost perfect quantitative agreement between the polarization model and the CH equation while the solutions of the CH model still provide predictions on a qualitative level in even larger parameter ranges. The CH equation is the universal order parameter equation for mass-conserved reaction-diffusion systems near instabilities like that of the model of Otsuji et al., near so-called type II stabilities, cf. Ref. [3]. This also explains their different behavior compared to classical reaction-diffusion models leading to Turing patterns via a finite wavelength instability. While Turing models can often be reduced to the Ginzburg-Landau equation as a universal order parameter equation [3], the CH equation takes that role for mass-conserved reaction-diffusion models. A common underlying order parameter equation for different models of cell polarization explains why they often behave in a similar way in large parameter ranges. Hence, studying mass conserved models of cell polarization via a reduction to the CH model can help to identify and explain the universal and generic features cell polarization.

One of them is the instability of multi-peak solutions that (almost) always leads to a fully polar system. The inherent coarsening behaviour of the CH equation with typical scaling laws [38] ensures exactly this behavior. The initially growing pattern is unstable towards one with a larger wavelength. Thereby the system settles in the largest possible wavelength—which is the system length, corresponding to a single-peak solutions observed in 1D. However, a long lasting coarsening process from a solution with a large number of peaks might be not the desired way for a cell to reach a polar, i.e. single-peak state. In this case our analysis also allows the identification of the parameter region where a direct transition from the homogenous state to the polar state takes place without undergoing a complex coarsening process. On the other hand the instability of i.e. a double-peak solution towards a single peak enables the cell to always adapt their polarization pattern to the cell length using the generic feature of coarsening to its advantage. This adaptability of the polar zone to the cell length is crucial for biological tasks such as cell division or the transition to a moving cell.

Spontaneous polarization without an external gradient is another feature observed in several models for cell polarization [42]. In the CH model this would correspond to the onset of polarization with a positive control parameter. In this case the CH model develops into a polarized state for both the symmetric and the asymmetric case. Another important task in many cell polarization systems is the sustainability of the polar or single-peak state, i.e. the pattern has to persist even if the external stimulus is no longer present [18, 34]. In the CH model this would correspond to the bistability between the homogeneous and the polarized state in the asymmetric case. In this bistable range a temporal increase of the control parameter (above

$\varepsilon = 0$) could push the system into the polarized state. If the control parameter then decreases again to subcritical values, the polarized state remains due to the hysteretic behavior in the bistable region. However, in this model this is only possible for asymmetric polarization ($\gamma_3 \neq 0$). To extend the sustainability also to symmetric polarization, a (intrinsic) subcritical bifurcation in the original model is necessary. In the picture of the Cahn-Hilliard equation this would lead to a change in the sign of the cubic nonlinearity γ_4. To stabilize the system in this case, higher order nonlinearities have to be taken into account. The Cahn-Hilliard equation has to be extended up to (at least) quintic order which will provide further generic aspects of cell polarization in upcoming works.

Materials and methods

Simulation methods

We solve the cell polarization model in Eqs (1), (2) and (3) numerically by using a pseudo-spectral method. We calculate all spatial derivatives by transformation to a suitable function space depending on the boundary conditions. For periodic boundaries used here i.e. $u|_{x=0} = u|_{x=L}$, $v|_{x=0} = v|_{x=L}$, where L is the system length, we use a Fourier representation of the fields. For Figs 2 and 3 in the main text, we use a system length $L = 800$ and $N = 512$ modes in Fourier space. The initial condition is a step-like function of the form

$$u(x) = A\left[\tanh\left(\frac{x - x_l}{\delta}\right) - \tanh\left(\frac{x - x_r}{\delta}\right)\right] - C, \tag{42}$$

where we choose C such that $\int_0^L u(x)dx = 0$ to fulfill the conservation law. We let this initial condition relax to a steady state. These steady state solutions are shown in Fig 2A and 2B and are also used to calculate the plateau values for different ε and a_2 values in Figs 2B and 3B, 3C and 3D respectively (all references refer to the main text). Figs 2A and 3A show only one half of the system. The second half is axially symmetric and thus does not contain additional information. Note that due to this inherent symmetry of the profiles, the result for periodic boundary conditions with a system size L are equivalent to those with no-flux boundaries and the system size $L/2$.

For the simulations in 2D in Fig 4 we use $L_x = L_y = 800$ and $N_x = N_y = 512$, starting from random initial conditions.

Calculation of the coarsening dynamics

The domain size $L(t)$ in Fig 4B is determined via

$$L(t) = 2\pi \frac{\sum S(k_i, t)dk}{\sum S(k_i, t)k_i dk}, \tag{43}$$

where $S(k_i, t)$ is the spherically averaged structure factor

$$S(k_i, t) = \langle |a_{\mathbf{k}_i}|^2 \rangle_{\mathbf{k}_i}. \tag{44}$$

$a_{\mathbf{k}_i}$ are the coefficients of the two dimensional Fourier transform whereby $\langle\rangle_{\mathbf{k}_i}$ denotes the radial average over all $\mathbf{k}_i$ with $k_i = |\mathbf{k}_i|$.

Supporting information

S1 Appendix. Derivation of CH equation from a cell polarization model.
(PDF)

S2 Appendix. Analytical calculation of plateau values.
(PDF)

Acknowledgments

Fruitful discussions with L. Rapp and support by the Elite Study Program Biological Physics is gratefully acknowledged.

Author Contributions

Conceptualization: Walter Zimmermann.

Funding acquisition: Walter Zimmermann.

Methodology: Fabian Bergmann.

Software: Fabian Bergmann.

Supervision: Walter Zimmermann.

Validation: Fabian Bergmann.

Visualization: Fabian Bergmann.

Writing – original draft: Fabian Bergmann, Walter Zimmermann.

Writing – review & editing: Fabian Bergmann, Walter Zimmermann.

References

1. Ball P. The Self-Made Tapestry: Pattern Formation in Nature. Oxford: Oxford Univ. Press; 1998.
2. Cross MC, Greenside H. Pattern Formation and Dynamics in Nonequilibrium Systems. Cambridge: Cambridge Univ. Press; 2009.
3. Cross MC, Hohenberg PC. Pattern formation outside of equilibrium. Rev Mod Phys. 1993; 65:851. https://doi.org/10.1103/RevModPhys.65.851
4. Aranson I, Kramer L. The world of the complex Ginzburg–Landau equation. Rev Mod Phys. 2002; 74:99. https://doi.org/10.1103/RevModPhys.74.99
5. Meron E. Nonlinear Physics of Ecosystems. Boca Raton, Florida: CRC Press; 2015.
6. Pismen LM. Patterns and Interfaces in Dissipative Dynamics. Berlin: Springer; 2006.
7. Koch AJ, Meinhardt H. Biological pattern formation: from basic mechanisms to complex structures. Rev Mod Phys. 1994; 66:1481. https://doi.org/10.1103/RevModPhys.66.1481
8. Kondo S, Miura T. Reaction-Diffusion Model as a Framework for Unterstanding Biological Pattern Formation. Science. 2010; 329:1616. https://doi.org/10.1126/science.1179047 PMID: 20929839
9. Alberts B, Johnson A, Lewis J, Raff M, Roberts K, Walter P. Molecular Biology of the Cell. New York: Garland Publishing; 2001.
10. Johnston DS, Ahringer J. Cell polarity in eggs and epithelia:parallels and diversity. Cell. 2010; 141:757. https://doi.org/10.1016/j.cell.2010.05.011
11. Thompson BJ. Cell polarity:models and mechanisms from yeast, worms and flies. Development. 2013; 140:13. https://doi.org/10.1242/dev.083634 PMID: 23222437
12. Goehring NW, Grill SW. Cell polarity: mechanochemical patterning. Trends Cell Biol. 2013; 23:72. https://doi.org/10.1016/j.tcb.2012.10.009 PMID: 23182746
13. Jilkine A and Marée A F M and Edelstein-Keshet L. Mathematical Model for Spatial Segregation of the Rho-Family GTPases Based on Inhibitory Crosstalk. Bull Math Biol. 2007; 69:1943. https://doi.org/10.1007/s11538-007-9200-6 PMID: 17457653
14. Otsuji M, Ishihara S, Co C, Kaibuchi K, Mochizuki A, Kuroda S. A Mass Conserved Reaction-Diffusion System Captures Properties of Cell Polarity. PLoS Comp Biol. 2007; 3:e108. https://doi.org/10.1371/journal.pcbi.0030108
15. Mori Y, Jilkine A, Edelstein-Keshet L. Wave-Pinning and Cell Polarity from a Bistable Reaction-Diffusion System. Biophys J. 2008; 94:3684. https://doi.org/10.1529/biophysj.107.120824 PMID: 18212014

16. Goryachev AB, Pokhilko AV. Flows Driven by Flagella of Multicellular Organisms Enhance Long-Range Molecular Transport. FEBS Lett. 2008; 582:1437.
17. Trong PK, Nicola EM, Goehring NW, Kumar KV, Grill SW. Parameter-space topology of models for cell polarity. New J Phys. 2014; 16:065009. https://doi.org/10.1088/1367-2630/16/6/065009
18. Jilkine A, Edelstein-Keshet L. A Comparison of Mathematical Models for Polarization of Single Eukaryotic Cells in Response to Guided Cues. PLoS Comput Biol. 2011; 7:e1001121. https://doi.org/10.1371/journal.pcbi.1001121 PMID: 21552548
19. Rubinstein B, Slaughter BD, Li R. Weakly nonlinear analysis of symmetry breaking in cell polarity models. Phys Biol. 2012; 9:045006. https://doi.org/10.1088/1478-3975/9/4/045006 PMID: 22871896
20. Alonso S, Bär M. Separation and bistability in a three-dimensional model for protein domain formation at biomembranes. Phys Biol. 2010; 7:046012. https://doi.org/10.1088/1478-3975/7/4/046012 PMID: 21149929
21. Iden S, Collard JG. Crosstalk between small GTPases and polarity proteins in cell polarization. Nature Rev Mol Cell Biol. 2008; 9:847. https://doi.org/10.1038/nrm2521
22. Goehring NW, Trong PK, Bois JS, Chowdury D, Nicola EM, Hyman AA, et al. Polarization of PAR proteins by advective triggering of a pattern-forming system. Science. 2011; 334:1137. https://doi.org/10.1126/science.1208619 PMID: 22021673
23. Bergmann F, Rapp L, Zimmermann W. Active phase separation: A universal approach. Phys Rev E. 2018; 98:020603(R). https://doi.org/10.1103/PhysRevE.98.020603
24. Keller EF, Segel LA. Initiation of slime mold aggregation viewed as an instability. J Theor Biol. 1970; 26:399. https://doi.org/10.1016/0022-5193(70)90092-5 PMID: 5462335
25. Keller EF, Segel LA. Model for chemotaxis. J Theor Biol. 1971; 30:225. https://doi.org/10.1016/0022-5193(71)90050-6 PMID: 4926701
26. Tindall MJ, Maini PK, Porter SL, Armitage JP. Overview of Mathematical Approaches Used to Model Bacterial Chemotaxis II: Bacterial Populations. Bull Math Biol. 2008; 70:1570. https://doi.org/10.1007/s11538-008-9322-5 PMID: 18642047
27. Hillen T, Painter KJ. A user's guide to PDE models for chemotaxis. J Math Biol. 2009; 58:183. https://doi.org/10.1007/s00285-008-0201-3 PMID: 18626644
28. Meyer M, Schimansky-Geier L, Romanczuk P. Active Brownian agents with concentration-dependent chemotactic sensitivity. Phys Rev E. 2014; 89:022711. https://doi.org/10.1103/PhysRevE.89.022711
29. Theurkauff I, Cottin-Bizonne C, Palacci J, Ybert C, Bocquet L. Dynamic Clustering in Active Colloidal Suspensions with Chemical Signaling. Phys Rev Lett. 2012; 108:26803. https://doi.org/10.1103/PhysRevLett.108.268303
30. Palacci J, Sacanna S, Steinberg AP, Pine DJ, Chaikin PM. Living crystals of light-activated colloidal surfers. Science. 2013; 339:936. https://doi.org/10.1126/science.1230020 PMID: 23371555
31. Bialké J, Löwen H, Speck T. Microscopic theory for phase separation of self-propelled repulsive disks. EPL. 2013; 103:30008. https://doi.org/10.1209/0295-5075/103/30008
32. Stenhammer J, Tiribocchi A, Allen RJ, Marenduzzo D, Cates ME. Continuum Theory of Phase Separation Kinetics for Active Brownian Particles. Phys Rev Lett. 2013; 111:145702. https://doi.org/10.1103/PhysRevLett.111.145702
33. Speck T, Bialké J, Menzel AM, Löwen H. Cahn-Hilliard Equation for the Phase Separation of Active Brownian Particles. Phys Rev Lett. 2014; 112:218304. https://doi.org/10.1103/PhysRevLett.112.218304
34. Bois JS, Jülicher F, Grill SW. Pattern Formation in Active Fluids. Phys Rev Lett. 2011; 106:028103. https://doi.org/10.1103/PhysRevLett.106.028103 PMID: 21405254
35. Fromherz P, Kaiser B. Stationary Patterns in Membranes by Nonlinear Diffusion of Ion Channels. Europhys Lett. 1991; 15:313. https://doi.org/10.1209/0295-5075/15/3/014
36. Liu QX, Doelman A, Rottschäfer V, de Jager M, Herman PM, van de Koppel MRJ. Phase separation explains a new class of self organized spatial patterns in ecological systems. Proc Natl Acad Sci USA. 2013; 110:11905. https://doi.org/10.1073/pnas.1222339110 PMID: 23818579
37. Cahn JW. On spinodal decomposition. Acta Metallurgica. 1961; 9:795. https://doi.org/10.1016/0001-6160(61)90182-1
38. Bray AJ. Theory of phase-ordering kinetics. Adv Phys. 1994; 43:357. https://doi.org/10.1080/00018739400101505
39. Holmes W, Lin B, Levchenko A, Edelstein-Keshet L. Modeling cell polarization driven by synthetic spatially graded Rac activation. PLoS Comput Biol. 2012; 8:e1002366. https://doi.org/10.1371/journal.pcbi.1002366 PMID: 22737059

40. Desai RC, Kapral R. Dynamics of Self-Organized and Self-Assembled Structures. Cambridge: Cambridge Univ. Press; 2009.

41. Bergmann F, Rapp L, Zimmermann W. Size matters for nonlinear (protein) wave patterns. New J Phys. 2018; 20:072001. https://doi.org/10.1088/1367-2630/aad457

42. Wedlich-Soldner R, Li R. Spontaneous cell polarization: undermining determinism. Nature Cell Biology. 2003; 5:267. https://doi.org/10.1038/ncb0403-267 PMID: 12669070

Publication 6

Systematic extension of the Cahn-Hilliard model for motility-induced phase separation

L. Rapp, F. Bergmann, and W. Zimmermann

Eur. Phys. J. E (2019) **42**: 57
DOI: (10.1140/epje/i2019-11825-8)

Reprinted with kind permission of The European Physical Society (EPJ)
©EDP Sciences / Società Italiana di Fisica /
Springer-Verlag GmbH Germany, part of Springer Nature,2019

Eur. Phys. J. E (2019) **42**: 57
DOI 10.1140/epje/i2019-11825-8

THE EUROPEAN PHYSICAL JOURNAL E

Regular Article

Systematic extension of the Cahn-Hilliard model for motility-induced phase separation

Lisa Rapp, Fabian Bergmann, and Walter Zimmermann[a]

Theoretische Physik I, Universität Bayreuth, 95440 Bayreuth, Germany

Received 10 January 2019 and Received in final form 9 April 2019
Published online: 16 May 2019
© EDP Sciences / Società Italiana di Fisica / Springer-Verlag GmbH Germany, part of Springer Nature, 2019

Abstract. We consider a continuum model for motility-induced phase separation (MIPS) of active Brownian particles (ABP) (J. Chem. Phys. **142**, 224149 (2015)). Using a recently introduced perturbative analysis (Phys. Rev. E **98**, 020604(R) (2018)), we show that this continuum model reduces to the classic Cahn-Hilliard (CH) model near the onset of MIPS. This makes MIPS another example of the so-called active phase separation. We further introduce a generalization of the perturbative analysis to the next higher order. This results in a generic higher-order extension of the CH model for active phase separation. Our analysis establishes the mathematical link between the basic mean-field ABP model on the one hand, and the leading order and extended CH models on the other hand. Comparing numerical simulations of the three models, we find that the leading-order CH model agrees nearly perfectly with the full continuum model near the onset of MIPS. We also give estimates of the control parameter beyond which the higher-order corrections become relevant and compare the extended CH model to recent phenomenological models.

1 Introduction

Active matter systems are non-equilibrium systems which consume fuel and disspative energy locally. These systems are full of fascinating phenomena and have recently attracted increasing attention in the scientific community [1–8]. Examples range from active molecular processes which are driven by chemical free energy provided by metabolic processes [9] up to flocks of birds and schools of fish [1, 2]. Various active matter systems also show collective non-equilibrium transitions. On the time scale of these transitions, the number of involved entities such as proteins, cells or even birds is conserved. Examples include cell polarization [10–16], chemotactically communicating cells [17–20], self-propelled colloidal particles [21–27], as well as mussels in ecology [28].

Self-propelling colloidal particles undergo a non-equilibrium phase transition into two distinct phases —a denser liquid-like phase and a dilute gas-like phase [21–23]— if their swimming speed decreases with increasing local density. This is known as motility-induced phase separation (MIPS) [4, 24, 26]. It strikingly resembles well-known phase separation processes at thermal equilibrium such as the demixing of a binary fluid. We recently introduced a class of such non-equilibrium demixing phenomena we call active phase separation [16]. Among the phenomena identified as members of this class are cell polarization or chemotactically communicating cells. For this class we have shown that the similarities between equilibrium and non-equilibrium demixing phenomena are in fact not coincidental. We have generalized a classical weakly nonlinear analysis near a supercritical bifurcation with unconserved order parameter fields [29] to the case of active phase separation with a conserved order parameter field [16]. The generic equation describing active phase separation systems turned out to be the classic Cahn-Hilliard (CH) model —the same generic model that also describes equilibrium phase separation. The class of active phase separation thus defines non-equilibrium demixing phenomena whose conserved order parameter is close to onset described by the Cahn-Hilliard model.

In this work, we raise the question whether the recently introduced nonlinear perturbation approach in ref. [16] is also directly applicable to MIPS. We employ this reduction approach to a mean-field description of active Brownian particles (ABP) showing MIPS provided by Speck *et al.* [27, 30] and show how the ABP model reduces to the CH model at leading order.

Recently, several phenomenological extensions of the CH model have also been considered as continuum models of MIPS [31,32]. These are extensions of the CH model to the next higher order of nonlinear contributions. In this

[a] e-mail: walter.zimmermann@uni-bayreuth.de

work, we therefore also introduce an extension of our perturbative scheme that allows us to systematically derive higher-order nonlinearities directly from the continuum model for MIPS. Due to our systematic approach, the extended CH model we derive is not a phenomenological model. Instead, we directly map the continuum model for ABP to the extended CH model. Note that we concentrate on the example of MIPS in this work. However, the extension introduced here can be applied to any system in the class of active phase separation. We thus show in general how both the leading-order CH model and its extension describe active phase separation as a non-equilibrium phenomenon.

This work is organized as follows: We first present the mean-field ABP model and calculate the onset of phase separation in the system. We then introduce the perturbative scheme we use to reduce the ABP model to the classic CH equation near the onset of phase separation. In the next step, we extend the previous approach to include nonlinearities at the next higher order. Section 5 is an in-depth discussion of the derived leading-order and extended CH models including their connection to the mean-field ABP model and other phenomenological descriptions of MIPS. Finally, in sect. 6, we present numerical simulations comparing leading-order and extended CH to the full mean-field ABP model to assess validity and accuracy of the reduced models.

2 Model

On a mean-field level, phase separation of active Brownian particles (ABP) can be described by two coupled equations for the particle density $\tilde{\rho}(\mathbf{r},t)$ and a polarization $\mathbf{p}(\mathbf{r},t)$ [23,30]. The evolution of the particle density $\tilde{\rho}$ is determined by

$$\partial_t \tilde{\rho} = -\nabla \cdot \left[v(\tilde{\rho})\mathbf{p} - D_e \nabla \tilde{\rho} \right], \tag{1}$$

where D_e is the effective diffusion coefficient of the active Brownian particles. $v(\tilde{\rho})$ is the density-dependent particle speed given by

$$v(\tilde{\rho}) = v_0 - \tilde{\rho}\zeta + \lambda^2 \nabla^2 \tilde{\rho}; \tag{2}$$

v_0 is the speed of a single self-propelled particle. With increasing particle density, the velocity is reduced by $\zeta\tilde{\rho}$ due to interactions with other particles. ζ is related to the pair distribution function of the individual particles and assumed to be spatially homogeneous [23]. The nonlocal contribution in eq. (2) was earlier introduced in refs. [25,33] and later incorporated into the model by Speck *et al.* [30]. It incorporates the effect that active Brownian particles sample the neighboring particle density on a length scale λ larger than the particle spacing. Equation (2) is coupled to a dynamical equation for the polarization [23,30],

$$\partial_t \mathbf{p} = -\nabla P(\tilde{\rho}) + D_e \nabla^2 \mathbf{p} - \mathbf{p}, \tag{3}$$

with the "pressure"

$$P(\tilde{\rho}) = \frac{1}{2} v(\tilde{\rho}) \tilde{\rho}. \tag{4}$$

3 Onset of phase separation

A stationary solution of eq. (1) and eq. (3) is any constant density $\bar{\rho}$ and $\mathbf{p} = 0$. Therefore, we decompose the particle density into its homogeneous part $\bar{\rho}$ and the inhomogeneous density variation ρ:

$$\tilde{\rho} = \bar{\rho} + \rho. \tag{5}$$

Accordingly, we investigate the following dynamical equations for ρ and p in one spatial dimension:

$$\partial_t \rho = -\partial_x \left[\alpha - \zeta\rho + \lambda^2 \partial_x^2 \rho \right] p + D_e \partial_x^2 \rho, \tag{6a}$$

$$\partial_t p = -\partial_x \left[\beta\rho - \frac{1}{2}\zeta\rho^2 + \frac{\lambda^2}{2}\left(\bar{\rho}+\rho\right)\partial_x^2 \rho \right] + D_e \partial_x^2 p - p, \tag{6b}$$

where

$$\alpha = v_0 - R, \qquad \beta = \frac{1}{2}(v_0 - 2R), \tag{7}$$

with the density parameter

$$R = \zeta\bar{\rho}. \tag{8}$$

We assume ζ and D_e to be constant [30].

The homogeneous basic solution $\rho = 0$, $p = 0$ is unstable if the perturbations $\rho, p = \hat{\rho}, \hat{p}\exp(\sigma t + iqx)$ grow, *i.e.* if the growth rate σ is positive. Solving the linear parts of eqs. (6) with this perturbation ansatz, the largest eigenvalue gives us the dispersion relation

$$\begin{aligned}\sigma(q) &= -\frac{1}{2} - D_e q^2 + \frac{1}{2}\sqrt{1 - 4\alpha\beta q^2 + 2\lambda^2 \alpha\bar{\rho} q^4}, \\ &= D_2 q^2 - D_4 q^4 + \mathcal{O}(q^6),\end{aligned} \tag{9}$$

where

$$D_2 = -(D_e + \alpha\beta), \tag{10}$$

$$D_4 = \left(\alpha^2\beta^2 - \frac{\lambda^2}{2}\frac{R}{\zeta}\alpha \right). \tag{11}$$

D_2 changes its sign as a function of v_0. Assuming $D_4 > 0$, the growth rate σ becomes positive in a finite range of $q = [0, q_{max}]$, when $D_2 > 0$. Note that the range of wavenumbers q with positive growth rate extends down to $q = 0$. The related instability condition

$$D_e + \alpha\beta = 0 \tag{12}$$

provides a quadratic polynomial for the critical mean density $\bar{\rho}$ (represented by the density parameter R) and the respective particle speed $v_0(R)$:

$$\frac{1}{2}v_0^2 - \frac{3}{2}Rv_0 + D_e + R^2 = 0. \tag{13}$$

For particle speeds $v_0 > v_*$, where

$$v_* = 4\sqrt{D_e}, \tag{14}$$

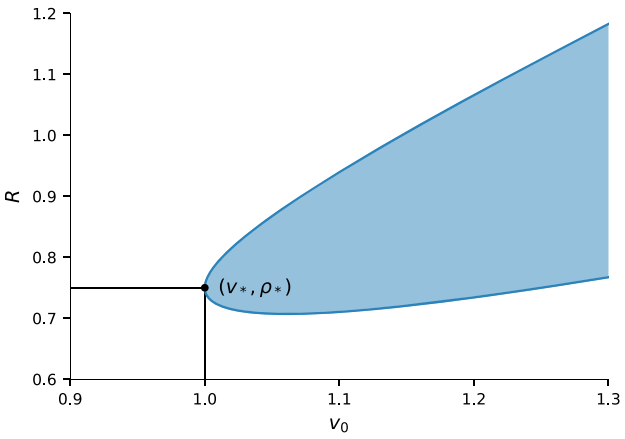

Fig. 1. Instability curve $R_\pm(v_0)$ as given by eq. (15). The minimum of the parabolic function is at $(v_*, R_*) = (1.0, 0.75)$, assuming $\zeta = 1$, $D_e = 1/16$. For $v_0 > v_*$, the homogeneous solution is unstable for mean densities within the shaded region.

this polynomial has two real solutions

$$R_\pm = \frac{1}{4}\left[3v_0 \pm \sqrt{v_0^2 - 16D_e}\right]. \tag{15}$$

This corresponds to a critical value R_* of the density parameter:

$$R_* = R(v_*) = \frac{3}{4}v_*. \tag{16}$$

Note that the assumption $D_4 > 0$ is fulfilled if $\lambda^2 < 2\zeta\alpha\beta^2/R$, *i.e.* for sufficiently small λ. At the critical point, $v_0 = v_*$ and $R = R_*$, this condition simplifies to

$$\lambda^2 < \zeta v_*^2/24. \tag{17}$$

For particle velocities below v_*, the homogeneous solution is stable for any value of the density parameter $R = \zeta\bar{\rho}$. For $v > v_*$ and $R_- < R < R_+$ (shaded region in fig. 1) the homogeneous particle density becomes unstable with respect to perturbations.

4 Derivation of Cahn-Hilliard models

In this section, we will apply the systematic pertubative scheme introduced recently in ref. [16] to the mean-field model, eqs. (6), and reduce them near onset to the well-known Cahn-Hilliard (CH) model. In a second step, we will then expand the pertubative scheme to include higher-order contributions.

The transition from the homogenous state of eqs. (1) and (3) to MIPS is either supercritical or slightly subcritical. In both cases, cubic nonlinearities limit the growth of density modulations —as we also confirm in this work *a posteriori*. Therefore, the amplitudes of the density modulations near MIPS are small and we write

$$\rho = \sqrt{\varepsilon}\rho_1 \tag{18}$$

with a small parameter ε and $\rho_1 \sim O(1)$. Thereby ε measures the distance from the critical velocity v_*:

$$v_0 = v_*(1 + \varepsilon). \tag{19}$$

This also allows an expansion of $R_\pm(v_0)$ in eq. (15) near R_*. At leading order, we find $R_\pm \simeq R_*(1 \pm \eta\sqrt{\varepsilon})$ with $\eta = \sqrt{2}/3$. This suggests the following parameterization of R in the ranges $v_0 > v_*$ and $R_- < R < R_+$ near R^*:

$$R = R_*(1 + r_1), \quad \text{with } r_1 = \sqrt{\varepsilon}\tilde{r}_1. \tag{20}$$

According to the dispersion relation in eq. (9), the fastest growing mode is given by $q_e^2 = D_2/(2D_4)$. The largest growing wavenumber q_{max} (calculated from $\sigma = 0$) is $q_{max}^2 = D_2/D_4$. Thus, both q_e^2 and q_{max}^2 scale with the factor D_2/D_4. Using the previously introduced definitions and expanding for small values of the control parameter ε, we find $D_2/D_4 \propto \varepsilon$ at leading order. Thus, both q_e and q_{max} are of the order $\sqrt{\varepsilon}$, *i.e.* perturbations of the homogeneous basic state vary on a large length scale. Accordingly, we introduce the new scaling $\tilde{x} = \sqrt{\varepsilon}x$, resulting in the following replacement of the differential operator:

$$\partial_x \to \sqrt{\varepsilon}\tilde{\partial}_x. \tag{21}$$

From q^2 of order $\mathcal{O}(\varepsilon)$ and $D_2 \propto \varepsilon$ follows that $\sigma \propto \varepsilon^2$ according to eq. (9). Thus, the growth of these long wavelength perturbations is very slow. Accordingly, we introduce the slow time scale $T_1 = \varepsilon^2 t$. In order to capture the dynamics at the next higher order of $\varepsilon^{1/2}$, we also introduce a second slow time scale $T_2 = \varepsilon^{5/2}t$. This suggests the following replacement of the time derivatives:

$$\partial_t \to \varepsilon^2\partial_{T_1} + \varepsilon^{5/2}\partial_{T_2}. \tag{22}$$

Since we expressed the density ρ as a multiple of $\sqrt{\varepsilon}$, see eq. (18), we also expand the polarization field p in orders of $\sqrt{\varepsilon}$:

$$p = \sqrt{\varepsilon}p_0 + \varepsilon p_1 + \varepsilon^{3/2}p_2 + \varepsilon^2 p_3 + \varepsilon^{5/2}p_4 + \dots. \tag{23}$$

We insert these scalings into the dynamic equations (6) and collect terms of the same order $\sqrt{\varepsilon}^n$. The polarization follows the density field adiabatically. Thus, the contributions to the polarization in increasing orders up to $\varepsilon^{5/2}$ are

$$p_0 = 0, \tag{24}$$

$$p_1 = -\beta_*\tilde{\partial}_x\rho_1, \tag{25}$$

$$p_2 = R_*\tilde{r}_1\tilde{\partial}_x\rho_1 + \frac{\zeta}{2}\tilde{\partial}_x(\rho_1^2), \tag{26}$$

$$p_3 = -\frac{v_*}{2}\tilde{\partial}_x\rho_1 - \left(D_e\beta_* + \frac{\lambda^2}{2}\frac{R_*}{\zeta}\right)\tilde{\partial}_x^3\rho_1, \tag{27}$$

$$p_4 = D_e\tilde{\partial}_x^3\left(\tilde{r}_1R_*\rho_1 + \frac{\zeta}{2}\rho_1^2\right) - \frac{\lambda^2}{2}\tilde{\partial}_x\left(\tilde{r}_1\rho_* + \rho_1\right)\tilde{\partial}_x^2\rho_1. \tag{28}$$

With these solutions, we can systematically solve the equations for the density ρ_1 in the successive orders of $\sqrt{\varepsilon}$. In the lowest order $\mathcal{O}(\varepsilon^{3/2})$, we find

$$0 = (\alpha_*\beta_* + D_e)\,\tilde{\partial}_x^2\rho_1. \tag{29}$$

This equation, however, is trivially satisfied due to the instability condition $\alpha_*\beta_* + D_e = 0$.

At order $\mathcal{O}(\varepsilon^2)$, we get

$$0 = -(\alpha_* + \beta_*)\left[R_*\tilde{r}_1\tilde{\partial}_x^2\rho_1 + \zeta\tilde{\partial}_x\left(\rho_1\tilde{\partial}_x\rho_1\right)\right]. \tag{30}$$

With the definition of R_* in eq. (16) it follows that $\alpha_* + \beta_* = 0$. Thus, eq. (30) is again trivially fulfilled.

At order $\mathcal{O}(\varepsilon^{5/2})$, we finally get a dynamic equation for ρ_1:

$$\begin{aligned}\partial_{T_1}\rho_1 = -\tilde{\partial}_x^2\Bigg[&\left(\frac{1}{8}v_*^2 - \frac{9}{16}v_*^2\tilde{r}_1^2\right)\rho_1 \\ &+ \left(\frac{1}{256}v_*^4 - \frac{3}{32\zeta}\lambda^2 v_*^2\right)\tilde{\partial}_x^2\rho_1 \\ &- \frac{3}{4}\zeta v_*\tilde{r}_1\,\rho_1^2 - \frac{1}{3}\zeta^2\,\rho_1^3\Bigg].\end{aligned} \tag{31}$$

Note that we used the expressions in eq. (14) and eq. (16) to eliminate R_* and D_e. Equation (31) has the form of the well-known Cahn-Hilliard (CH) equation [34, 35]. This shows that MIPS is a further example of the non-equilibrium demixing phenomenon which shares the universal CH model with classic phase separation. Recently, the notion *active phase separation* was coined for these types of non-equilibrium phenomena [16]. Other recently discussed examples of active phase separation are cell polarization or chemotactically communicating cell colonies [16]. All of these very different systems can be reduced to the same universal equation near the onset of phase separation. They thus share generic features as expressed in their common representation via the CH equation.

In the next step, we extend the reduction scheme introduced in ref. [16] to include higher-order nonlinearities. Continuing the expansion above to the next order $\mathcal{O}(\varepsilon^3)$, we obtain:

$$\begin{aligned}\partial_{T_2}\rho_1 = -\tilde{\partial}_x^2\Bigg[&\frac{9}{8}v_*^2\tilde{r}_1\rho_1 + \frac{3}{16\zeta}\lambda^2 v_*^2\tilde{r}_1\left(\tilde{\partial}_x^2\rho_1\right) + \frac{3}{4}\zeta v_*\rho_1^2 \\ &+ \left(\frac{3}{128}\zeta v_*^3 - \frac{5}{16}\lambda^2 v_*\right)\left(\tilde{\partial}_x\rho_1\right)^2 \\ &+ \frac{\lambda^2}{8}v_*\tilde{\partial}_x^2\rho_1^2\Bigg].\end{aligned} \tag{32}$$

We will discuss these new contributions in detail in sect. 5.2 below.

Equations (31) and (32) can be combined into a single equation by reconstituting the original time scale via $\partial_t\rho_1 = \varepsilon^2\partial_{T_1}\rho_1 + \varepsilon^{5/2}\partial_{T_2}\rho_1$. In addition, we go back to the original spatial scaling by setting $\tilde{\partial}_x = \partial_x/\sqrt{\varepsilon}$, to the original density ρ via eq. (18), and r_1 as defined in eq. (20). The complete extended amplitude equation for the density variations ρ then reads:

$$\begin{aligned}\partial_t\rho = -\partial_x^2\Big[&(\alpha_1 + \beta_1)\,\rho + (\alpha_2 + \beta_2)\,\partial_x^2\rho \\ &+ (\alpha_3 + \beta_3)\,\rho^2 - \alpha_4\rho^3 \\ &+ \beta_5\,(\partial_x\rho)^2 + \beta_6\partial_x^2\rho^2\Big].\end{aligned} \tag{33}$$

In this equation, contributions with the coefficients α_i originate from the leading order and are given by

$$\alpha_1 = \frac{1}{8}v_*^2\varepsilon - \frac{9}{16}v_*^2 r_1^2, \tag{34a}$$

$$\alpha_2 = \frac{1}{256}v_*^4 - \frac{3}{32\zeta}\lambda^2 v_*^2, \tag{34b}$$

$$\alpha_3 = -\frac{3}{4}\zeta v_* r_1, \tag{34c}$$

$$\alpha_4 = \frac{1}{3}\zeta^2. \tag{34d}$$

In other words, eq. (33) with $\beta_i = 0$ is the rescaled version of eq. (31). The coefficients β_i signal the new contributions from the next higher order. They are given by

$$\beta_1 = \frac{9}{8}v_*^2 r_1\varepsilon, \tag{35a}$$

$$\beta_2 = \frac{3}{16\zeta}\lambda^2 v_*^2 r_1, \tag{35b}$$

$$\beta_3 = \frac{3}{4}\zeta v_*\varepsilon, \tag{35c}$$

$$\beta_5 = \frac{3}{128}\zeta v_*^3 - \frac{5}{16}\lambda^2 v_*, \tag{35d}$$

$$\beta_6 = \frac{\lambda^2}{8}v_*. \tag{35e}$$

5 Discussion of the derived Cahn-Hilliard models

In this section, we will discuss the results obtained in the previous sect. 4. At first we consider the classic CH equation that resulted at leading order of our perturbative analysis. We then take a closer look at the higher-order corrections $\propto \beta_i$ in eq. (33). We also focus on the relation of the higher-order coefficients β_i to the parameters of recently introduced phenomenological extensions of the CH model for MIPS [31, 32, 36].

5.1 Classic CH equation at leading order

For $\beta_i = 0$, the leading order of eq. (33),

$$\partial_t\rho = -\partial_x^2\left[\alpha_1\rho + \alpha_2\partial_x^2\rho + \alpha_3\rho^2 - \alpha_4\rho^3\right], \tag{36}$$

corresponds to the asymmetric version of the Cahn-Hilliard (CH) equation, see *e.g.* refs. [34, 35], The coefficients α_i are given in eqs. (34). Note that the quadratic

nonlinearity implies a broken $\pm\rho$-symmetry. This is usually not included in the classic representation of the CH equation since it can be removed by adding a constant to the density: $\rho \to \rho + \rho_h$. In any case, the quadratic nonlinearity vanishes for $\alpha_3 = 0$. For the ABP model, this is fulfilled for $r_1 = 0$, or $\bar{\rho} = \rho_*$ accordingly. This special case has also been considered in [30] where they found a CH equation with coefficients consistent with α_i above.

Equation (36) can be derived from the energy functional

$$F = \int \left[-\frac{\alpha_1}{2} + \frac{\alpha_2}{2}(\partial_x \rho)^2 - \frac{\alpha_3}{3}\rho^3 + \frac{\alpha_4}{4}\rho^4 \right] \mathrm{d}x \qquad (37)$$

via

$$\partial_t \rho = \partial_x^2 \frac{\delta F}{\delta \rho} \,. \qquad (38)$$

At first glance this is a surprising result since the two initial dynamical equations for the density, eq. (1), and the polarization, eq. (3), do not follow potential dynamics and therefore cannot be derived from a functional. Nevertheless, this specific property has been seen for other non-equilibrium systems: The evolution equation for the envelope of spatially periodic patterns also follows potential dynamics while the dissipative starting equations do not [29,37].

5.2 Extended CH model

We now take a closer look at the CH model extended to the next higher order, eq. (33) with coefficients β_i given in eqs. (35). The contributions β_1, β_2 and β_3 are corrections to the coefficients α_1, α_2 and α_3 of the leading-order CH equation. Note, however, that according to eqs. (35a) and (35c), β_1 and β_3 are functions of ε and thus both increase with the distance ε from phase separation onset. Notably, β_3 —the correction to the quadratic nonlinearity— is not a function of the relative deviation r_1 from the critical density parameter R_*. Thus, while for $r_1 = 0$ the CH model at leading order is $\pm\rho$-symmetric, the symmetry is always broken at higher order.

The coefficients β_5 and β_6 are the prefactors of higher-order nonlinearities. These new contributions $\propto \partial_x^2(\partial_x\rho)^2$ and $\propto \partial_x^4\rho^2$ are structurally different compared to the terms in the leading-order CH model. In general, an additional nonlinearity $\propto \partial_x^2\rho^4$ is of the same order as these two contributions. However, in the exemplary case of ABP we analyze here this term does not appear. Note, however, that the higher-order extension of the CH model presented here can also be applied to other active phase separation systems. We expect the additional nonlinearity of the form $\propto \partial_x^2\rho^4$ to be relevant in other examples such as cell polarization or chemotaxis.

In the context of MIPS, a contribution $\propto \partial_x^2(\partial_x\rho)^2$ has been introduced via a phenomenological approach in ref. [31]. The CH model extended by this term has been called *Active Model B*. It was considered as a non-equilibrium extension of the CH model and minimal model for MIPS. We would like to reiterate that the CH model as given by eq. (36) (without any additional nonlinear terms) is the leading-order description of the *non-equilibrium* phenomenon of active phase seperation [16]. As we have shown here, this also includes MIPS. All higher-order nonlinearities vanish for $\varepsilon \to 0$ (see also the discussion in sect. 5.4). In that respect *Active Model B* is a nonlinear extension of the CH model —not an extension of the CH model to non-equilibrium systems. Our systematic approach reveals the existence of the additional higher nonlinearity $\propto \partial_x^4\rho^2 = 2\partial_x^2[(\partial_x\rho)^2 + \rho\partial_x^2\rho]$. It includes the nonlinear correction to the CH model, $\propto \partial_x^2(\partial_x\rho)^2$, that leads to the *Active Model B* [4,31]. The second part of the new nonlinear correction term, $\propto \partial_x^2(\rho\partial_x^2\rho)$, has recently been included in a further CH extension for MIPS called *Active Model B+* [32,36]. Note that the contribution $\propto \beta_6$ in eq. (33) vanishes for $\lambda = 0$. *Active Model B* and *Active Model B+* also do not include the quadratic nonlinearity $\propto \beta_3\rho^2$. Our analysis shows, however, that the coefficients β_i in general are not independent of each other and β_2 in fact always appears simultaneously with the nonlinearity $\propto \beta_5$. The broken $\pm$-symmetry and the resulting asymmetric phase separation profiles depend on the distance ε from threshold (see β_3 in eq. (35c)). It is an important qualitative feature of the system behavior above threshold.

As discussed in sect. 5.1, the leading-order CH model can be derived from an energy potential. For the extended CH model, eq. (33), the existence of an energy functional depends on the coefficients of the additional higher-order contributions: for arbitrary values of β_5 and β_6, the extended CH model is non-potential. In the special case $\beta_6 = -\beta_5$, however, eq. (33) can be derived from the energy functional

$$F = \int \left[\frac{-\alpha_1 + \beta_1}{2}\rho^2 + \frac{\alpha_2 + \beta_2}{2}(\partial_x\rho)^2 - \frac{\alpha_3 + \beta_3}{3}\rho^3 - \frac{\alpha_4}{4}\rho^4 + \frac{\beta_5}{2}\rho^2\partial_x^2\rho \right] \mathrm{d}x. \qquad (39)$$

For the ABP model, eqs. (6), this condition is fulfilled for

$$\lambda^2 = \frac{\zeta {v_*}^2}{8} \,. \qquad (40)$$

Note, however, that the linear stability analysis in sect. 3 introduced a condition for λ: $\lambda^2 < \zeta v_*^2/24$ in eq. (17). This condition and eq. (40) cannot be fulfilled simultaneously. Thus, whether the extended CH model can be derived from an energy functional depends on the exact parameter choices. For the ABP continuum model we investigate here, there do not seem to be suitable parameter choices. But note again that our approach can be applied to other systems showing active phase separation. For these other models, the coefficients of the extended CH model could allow for the existence of a suitable potential.

5.3 Comparison of linear stability

As a first step to assess the quality of our derived reduced equation, eq. (33), we analyze the linear stability of the

homogeneous basic state $\rho = 0$, and compare to the stability of the full ABP model. As discussed in sect. 3, the instability condition for the full ABP system is given by eq. (12). Using $v_0 = v_*(1+\varepsilon)$, $R = R_*(1+r_1)$ and the definitions of D_e and R_* as given by eqs. (14) and (16), we find

$$\begin{aligned}\varepsilon_c &= \frac{1}{8}(1+9r_1) - \frac{1}{8}\sqrt{1+18r_1+9r_1^2} \\ &\approx \frac{9}{2}r_1^2 - \frac{81}{2}r_1^3 + \frac{891}{2}r_1^4 + \mathcal{O}(r_1^5) \end{aligned} \tag{41}$$

for the onset of phase separation. Thus, in the symmetric case $r_1 = 0$ the threshold is $\varepsilon_c = 0$. For $r_1 \neq 0$ the onset of phase separation is shifted to larger values of ε. Larger particle velocities v_0 are thus required to trigger the demixing process.

Similarly, we can analyze the linear stability of both the leading-order CH equation, eq. (36), and its higher-order extension, eq. (33). The threshold calculated from the linear parts of eq. (36) is given by

$$\varepsilon_{c,\mathrm{lead}} = \frac{9}{2}r_1^2. \tag{42}$$

Comparing this to ε_c in eq. (41), we find that the shifting of the threshold due to finite r_1 is represented up to leading order of r_1. Assuming $r_1 > 0$, $\varepsilon_{c,\mathrm{lead}}$ significantly overestimates the real threshold ε_c. For the extended CH equation, eq. (33), we find the threshold

$$\begin{aligned}\varepsilon_{c,\mathrm{ext}} &= \frac{9r_1^2}{2(1+9r_1^2)} \\ &\approx \frac{9}{2}r_1^2 - \frac{81}{2}r_1^3 + \frac{729}{2}r_1^4 + \mathcal{O}(r_1^5). \end{aligned} \tag{43}$$

This is in agreement with the threshold for the full model, eq. (41), up to the order $\mathcal{O}(r_1^3)$. The threshold is therefore only slightly underestimated compared to the full model. Keeping these different threshold values in mind is particularly important for the numerical comparison of the ABP model, eqs. (1) and (3), to its two reductions, eqs. (36) and (33) in sect. 6. All three equations only provide the exact same threshold, namely $\varepsilon_c = 0$, in the special case $r_1 = 0$.

The linear stability analysis also provides the dispersion relation for the perturbation growth rate σ. For the full model, it is given by eq. (9). Expanding for small perturbation wavenumbers q, the general form of the growth rate is

$$\sigma = D_2 q^2 - D_4 q^4 + \mathcal{O}(q^6). \tag{44}$$

The coefficients D_2 and D_4 are given in eqs. (10) and (11), respectively. Using the definitions introduced in the course of the perturbative expansion, D_2 can be rewritten to

$$D_2 = \frac{1}{8}v_*^2\varepsilon - \frac{9}{16}v_*^2 r_1^2 + \frac{9}{8}v_*^2 r_1\varepsilon - \frac{1}{2}v_*^2\varepsilon^2. \tag{45}$$

Good agreement between the full ABP model and its reduction to eq. (33) can only be expected if the reduced equations are able to reproduce the basic form of this growth rate. The linear part of eq. (33) leads to a growth rate of the form

$$\sigma(q) = G_2 q^2 - G_4 q^4, \tag{46}$$

where

$$G_2 = \frac{1}{8}v_*^2\varepsilon - \frac{9}{16}v_*^2 r_1^2 + \frac{9}{8}v_*^2 r_1\varepsilon, \tag{47}$$

$$G_4 = \frac{1}{256}v_*^4 - \frac{3}{32\zeta}\lambda^2 v_*^2 + \frac{3}{16\zeta}\lambda^2 v_*^2 r_1. \tag{48}$$

G_2 is in agreement with D_2 of the full model equations up to linear order in ε. D_2 only includes an additional term of order $\mathcal{O}(\varepsilon^2)$: $D_2 = G_2 - v_*^2\varepsilon^2/2$. G_4 exactly reduces to D_4 in the case $\varepsilon = r_1 = 0$. In the limit $\varepsilon \to 0$ but $r_1 \neq 0$, the two terms agree up to linear order in r_1. As discussed in sect. 3, the coefficient D_4 has to be positive for the instability condition to hold and to ensure damping of short wavelength perturbations. The same applies to the coefficient G_4. The condition $G_4 > 0$ is fulfilled if

$$\lambda^2 < \frac{1}{24}v_*^2\zeta\frac{1}{1-2r_1}. \tag{49}$$

Note the similarity to the previously derived condition in eq. (17).

5.4 Significance of nonlinear corrections

In this section, we discuss the importance of the higher-order nonlinearities compared to the leading-order terms of the classic Cahn-Hilliard model in eq. (36). For this comparison we focus on the case with ±-symmetry at leading order, *i.e.* $r_1 = 0$. We rescale time, space and amplitude in eq. (33) via $t' = \tau_0\varepsilon^2 t$, $x' = \xi_0\sqrt{\varepsilon}x$ and $\rho' = \rho_0\rho/\sqrt{\varepsilon}$, respectively, where

$$\tau_0 = \frac{4\zeta v_*^2}{v_*^2\zeta - 24\lambda^2}, \tag{50a}$$

$$\xi_0^2 = \frac{32\zeta}{v_*^2\zeta - 24\lambda^2}, \tag{50b}$$

$$\rho_0 = \frac{2\sqrt{6}}{3}\frac{\zeta}{v_*}. \tag{50c}$$

This allows us to rewrite eq. (33) in the following form:

$$\begin{aligned}\partial_{t'}\rho' = &-\partial_{x'}^2\left[\rho' + \partial_{x'}^2\rho' - \rho'^3\right] \\ &-\sqrt{\varepsilon}\partial_{x'}^2\left[\gamma_1\rho'^2 + \gamma_2\partial_{x'}^2\rho'^2 + \gamma_3\left(\partial_{x'}\rho'\right)^2\right], \end{aligned} \tag{51}$$

where

$$\gamma_1 = \frac{3\sqrt{6}}{2}, \tag{52a}$$

$$\gamma_2 = \frac{8\sqrt{6}\lambda^2}{v_*^2\zeta - 24\lambda^2}, \tag{52b}$$

$$\gamma_3 = \frac{\sqrt{6}(3v_*^2\zeta - 40\lambda^2)}{2(v_*^2\zeta - 24\lambda^2)}. \tag{52c}$$

The first line in eq. (51) is the parameter-free, $\pm\rho$-symmetric version of the Cahn-Hilliard model as described, *e.g.*, in refs. [34, 35]. The additional three contributions are the first higher-order corrections as gained above via a systematic reduction of the continuum model for MIPS. These three corrections are proportional to $\sqrt{\varepsilon}$ and thus vanish when approaching the onset of active phase separation ($\varepsilon \to 0$). In the limit $\varepsilon \to 0$ the classic CH model thus fully describes the non-equilibrium mean-field dynamics of MIPS. With increasing ε, the higher-order contributions become more and more important.

Note that eq. (51) was derived under the assumption $r_1 = 0$. As discussed in sect. 5.1, the CH model at leading order is $\pm\rho$-symmetric in this case. The three higher-order contributions in eq. (51), however, break the $\pm\rho$-symmetry with increasing ε. Moreover, in the case of the ABP model we analyze here, the coefficient γ_1 does not depend on any of the system parameters at all. Thus, there is in fact no special case in which this contribution can be neglected.

The coefficients of the other two higher-order nonlinearities, γ_2 and γ_3, are functions of the system parameters, especially of λ. Typical parameter choices for the continuum model in eq. (6) are such that v_* and ζ are of order $\mathcal{O}(1)$. Accordingly, λ has to be small to fulfill the condition in eq. (17). Therefore, an expansion of γ_2 and γ_3 in terms of small λ is appropriate:

$$\gamma_2 = \frac{8\sqrt{6}}{v_*^2\zeta}\lambda^2 + \mathcal{O}(\lambda^4), \tag{53}$$

$$\gamma_3 = \gamma_1 + 2\gamma_2 + \mathcal{O}(\lambda^4). \tag{54}$$

In the limit $\lambda = 0$ the coefficient γ_2 vanishes, *i.e.* $\gamma_2 = 0$, and γ_3 simplifies to $\gamma_3 = \gamma_1$. For finite λ, γ_2 also becomes finite. But since according to eq. (53) γ_2 is proportional to λ^2, it will be much smaller than γ_3 for small λ. For MIPS as described by the mean-field model in eqs. (6), the impact of the nonlinearity $\propto \partial_x^2(\partial_x\rho)^2$ thus seems to overshadow the term $\propto \partial_x^4\rho^2$. This predominance of γ_3, however, is specific to MIPS as described by the ABP model. For other examples of active phase separation such as cell polarization or chemotactically communicating cells, we expect that the nonlinearities described by γ_1 or γ_2 can be of similar order as γ_3. As mentioned earlier, for both examples of active phase separation we also expect an additional higher-order correction $\propto \partial_x^2\rho^4$ which is completely absent in the ABP model.

6 Numerical comparison

In this section, we compare numerical simulations of the full ABP model, eqs. (6), to both the leading-order CH equation, eq. (36), as well as the extended version including higher nonlinearities, eq. (33). On the one hand, this allows us to assess the quality and validity range of our reduction scheme in general. On the other hand, comparing the leading-order and the extended CH model also gives us information about the importance of higher-order nonlinearities in MIPS.

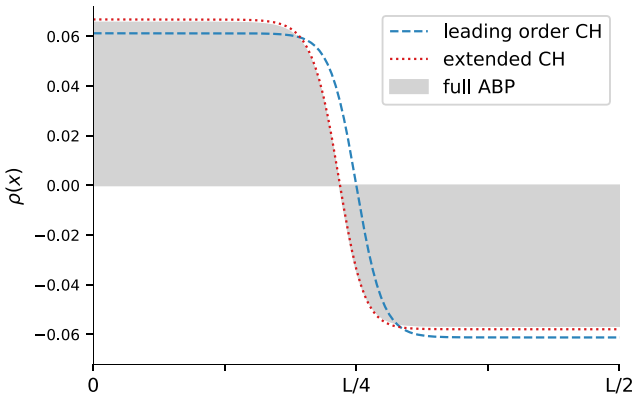

Fig. 2. Comparison of the steady-state profiles in the "symmetric" case ($\bar{\rho} = \rho_*$) at $\varepsilon = 0.01$: full ABP model (shaded grey) *vs.* leading-order CH equation (dashed line) *vs.* extended CH equation (dotted line). Other parameters: $\zeta = v_* = 1$.

All simulations were performed using a spectral method with a semi-implicit Euler time step. The system size was $L = 100$ with periodic boundary conditions and $N = 256$ Fourier modes were used.

We first analyze the special case $r_1 = 0$, *i.e.* $\bar{\rho} = \rho_*$. This is the case in which the $\pm$-symmetry-breaking quadratic nonlinearity vanishes at leading order. We choose $v_* = 1$ and $\zeta = 1$ throughout all of the following simulation results. As discussed in sect. 5.4, λ has to be small and is thus not expected to significantly influence the results. We thus set $\lambda = 0$.

Figure 2 shows the steady-state profiles for the three models (full ABP model, leading-order CH and extended CH) at $\varepsilon = 0.01$. The profiles are typical for phase separation solutions: We find two distinct regions where the mean density is either increased ($\rho > 0$) or decreased ($\rho < 0$). In each of the regions ρ is essentially spatially constant, creating two distinct density plateaus $\rho_{\min}$ and $\rho_{\max}$. The two plateaus are smoothly connected at their boundary, resembling a hyperbolic tangent function. Note that the mean density in the system is conserved. Thus, the areas under the positive and negative parts of $\rho(x)$ are equal.

The solution for the full system is represented as the outline of the grey shaded area. We first compare this to the leading-order CH equation (dashed line). As predicted, the leading-order CH equation results in a symmetric phase separation profile, *i.e.* the two plateaus have the same absolute value: $\rho_{\max} = |\rho_{\min}|$. This does not accurately represent the solution for the full system, which is already slightly asymmetric. However, the leading-order CH equation gives a good approximation of the plateau values with a deviation of less than 7% from the real value. Extending the CH equation to the next higher order (dotted line in fig. 2), we can almost perfectly reproduce the profile for the full ABP model. It accurately represents the asymmetry of the phase separation profile. The deviation in the plateau values shrinks to less than 2%.

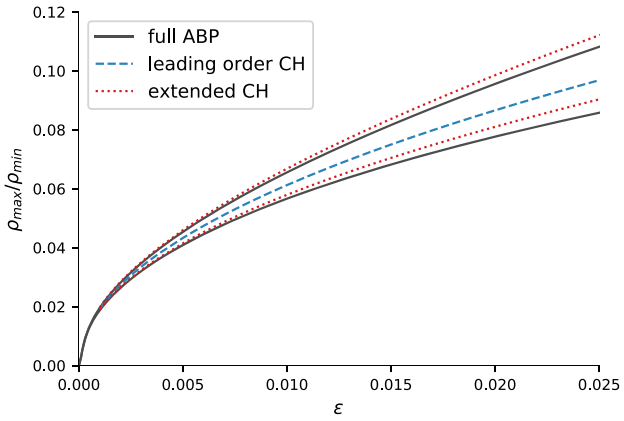

Fig. 3. Comparison of plateau values $|\rho_{\min}|$ and $\rho_{\max}$ as a function of the control parameter ε for $\bar{\rho} = \rho_*$ (*i.e.*, $r_1 = 0$): full ABP model (solid line) *vs.* leading-order CH equation (dashed line) *vs.* extended CH equation (dotted line).

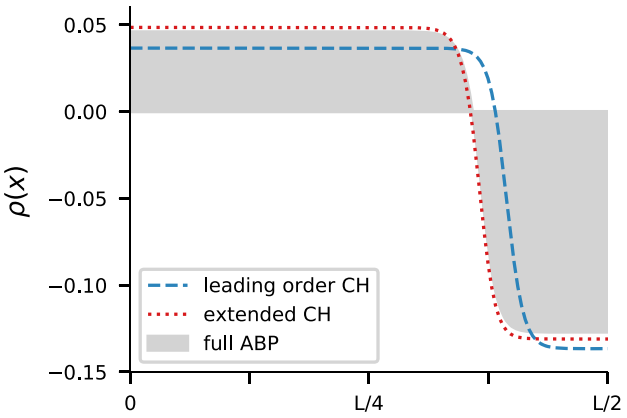

Fig. 4. Comparison of the steady-state profiles for $\bar{\rho} = 0.8$ at $\varepsilon = 0.02$: full ABP model (shaded grey) *vs.* leading-order CH equation (dashed line) *vs.* extended CH equation (dotted line).

Figure 3 shows the absolute plateau values $|\rho_{\min}|$ and $\rho_{\max}$ as a function of ε —the distance from the phase separation onset. The bifurcation to active phase separation is supercritical in this case: starting at $\varepsilon_c = 0$, the plateau values increase monotonically. Considering only the leading-order approximation (dashed line), we again find the system to be symmetric for all values of ε. In reality, the full system (solid lines) becomes more and more asymmetric for increasing ε. This is very accurately represented by the higher-order approximation (dotted lines). It only starts to deviate from the full model further from threshold. Importantly though, close to the onset of mobility-induced phase separation, as ε becomes smaller, the full model becomes more and more symmetric. All three models then are in increasingly good agreement. This again underlines the fact that the classic CH model is the simplest generic model for active phase separation. All active phase separation phenomena of this type can be reduced to the CH model close to onset. Higher-order nonlinearities only come into play further from threshold.

If we allow $r_1 \neq 0$, phase separation is asymmetric even at leading order. This can be seen in fig. 4 which shows the steady-state profiles for the full ABP model, leading-order CH and extended CH at $\varepsilon = 0.02$. Here, the leading-order CH equation (dashed line) results in an asymmetric solution. However, the predicted plateau values deviate about 20% from the full system (outlines of shaded grey region). The extended CH model, meanwhile, is still able to accurately predict the full system solution with a deviation of less than 6%.

Looking at the plateau values as a function of ε (see fig. 5) solidifies this impression: the leading-order CH model gives a good qualitative representation of the full system. Going to the extended CH model provides very good quantitative agreement with the full model even for larger values of ε. As discussed earlier in sect. 5.3, the onset of phase separation (*i.e.* the ε-value at which the homogeneous solution $|\rho_{\min}| = \rho_{\max} = 0$ becomes unstable) is shifted to finite values of ε in the case $r_1 \neq 0$.

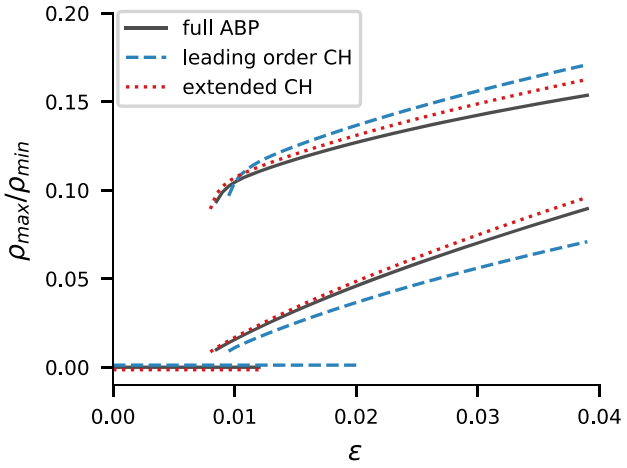

Fig. 5. Comparison of plateau values $|\rho_{\min}|$ and $\rho_{\max}$ as a function of the control parameter ε for $\bar{\rho} = 0.8$ (or $r_1 = 1/15$): full ABP model (solid line) *vs.* leading-order CH equation (dashed line) *vs.* extended CH equation (dotted line).

For the given system parameters, the threshold for the full system is shifted to $\varepsilon_c \approx 0.013$. The leading-order CH model significantly overestimates this threshold, shifting to $\varepsilon_c \approx 0.02$. The extended CH model only very slightly underestimates the real threshold. Note that above this threshold, the plateau values immediately jump to finite values. Thus, the transition from the homogeneous to the phase-separated state is no longer smooth. On the other hand, fig. 5 also shows that the branches of finite density plateau values extend below the thresholds noted above. This creates a range of bistability —a range of control parameter values in which both the homogeneous and the phase-separated state are stable simultaneously. All of these characteristics indicate that bifurcation from the homogeneous state to active phase separation is now subcritical.

7 Conclusion

Starting from the mean-field model for active Brownian particles in refs. [23, 30], we applied a perturbative approach introduced in ref. [16]. We showed that the non-equilibrium phenomenon motility-induced phase separation (MIPS) is described near its onset at leading order by the Cahn-Hilliard (CH) model [34,35,38,39]. This is in agreement with a recent observation that the CH model describes the system-spanning behavior of a number of very different demixing phenomena in active and living systems far from thermal equilibrium [16]. The results in this work show that MIPS also belongs to this class of active phase separation. Thus, even though the CH model was originally introduced to describe phase separation of binary mixtures in thermal equilibrium, our analysis shows that it is also the generic leading-order description of active phase separation —a non-equilibrium phenomenon.

We also extended the perturbative scheme introduced in ref. [16] beyond the CH model to next higher-order nonlinearities. In this work, we used the continuum ABP model as a framework to establish this concept. The extension of our nonlinear expansion, however, can also be applied to other systems showing active phase separation (with a conserved order parameter field) such as cell polarization and clustering of chemotactically communicating cells. Having a $\pm$-symmetric CH model at the onset of active phase separation, we find that in general four nonlinear terms come into play at the next higher order. Two of them have the same form as contributions suggested in previous phenomenological extensions of the CH model for MIPS [4,31,32,36]. These phenomenological models are thus related to the extended CH model that our perturbative scheme provides. Our approach, however, is non-phenomenological: it establishes a direct mathematical link between the coefficents of the extended CH model and the full mean-field description of ABPs (or any other basic model of active phase separation in general). It shows in addition, that the coefficients of the additional contributions in the extended CH model are in general not independent of each other, as often assumed in phenomenological approaches. Furthermore, these coefficents are system-specific and cannot be removed by rescaling as in the case of the leading-order CH model. It is also important to reiterate that these nonlinear extensions become negligible when approaching the onset of MIPS or other examples of active phase separation. Therefore, the leading-order CH model already covers the universal behavior of MIPS (as a non-equilibrium phenomenon) near its onset. Higher-order nonlinearities mainly improve accuracy and become relevant further from threshold. They should thus not be seen as the key to expand the CH model to non-equilibrium systems.

Within the systematics of the pattern formation theory, the work we introduced in ref. [16] and extended here is a weakly nonlinear analysis and reduction method for active phase separation described by conserved order parameter fields. It can be seen as a yet unexplored counterpart to the weakly nonlinear analysis of (non-oscillatory) spatially periodic patterns with unconserved order parameter fields and its numerous applications [29, 37, 40–42].

Our generic approach for active phase separation opens up several pathways for further system-spanning investigations. Coarsening dynamics in large systems, and especially the role of higher nonlinearities in this context, have already been of particular interest to the scientific community (see, *e.g.*, ref. [32] for MIPS). Other active phase separation phenomena such as cell polarization, on the other hand, take place in very small systems where coarsening plays a less important role [43]. For these systems, spatial constraints may significantly influence the behavior instead. Studies on spatially periodic patterns have already shown that confinement may trigger various interesting generic effects (see *e.g.* [44]) and even induce patterns in small systems which are unstable in larger systems (see [45] and references therein). On the basis of our results, it will be interesting to investigate finite size effects on non-equilibrium phase transitions with conservation constraints.

Support by the Elite Study Program Biological Physics is gratefully acknowledged.

Author contribution statement

All authors contributed to the design of the research, to calculations, the interpretation of results and the writing of the manuscript. LR performed numerical simulations.

Availability of data and materials

The simulation datasets used in this article are available from the corresponding author on request.

Publisher's Note The EPJ Publishers remain neutral with regard to jurisdictional claims in published maps and institutional affiliations.

References

1. T. Vicsek, A. Zafeiris, Phys. Rep. **517**, 71 (2012).
2. A. Cavagna, I. Giardina, Annu. Rev. Condens. Matter Phys. **5**, 183 (2014).
3. A.A. Hyman, C.A. Weber, F. Jülicher, Annu. Rev. Cell Dev. Biol. **30**, 39 (2014).
4. M.E. Cates, J. Tailleur, Annu. Rev. Condens. Matter Phys. **6**, 219 (2015).
5. S. Zhou, A. Sokolov, O.D. Lavrentovich, I.S. Aranson, Proc. Natl. Acad. Sci. U.S.A. **111**, 1265 (2014).
6. C. Bechinger, R. Di Leonardo, H. Löwen, C. Reichardt, G. Volpe, G. Volpe, Rev. Mod. Phys. **88**, 045006 (2016).
7. Y. Shin, C.P. Brangwynne, Science **357**, 4382 (2017).
8. F. Jülicher, S.W. Grill, G. Salbreux, Rep. Prog. Phys. **81**, 076601 (2018).

9. B. Alberts, A. Johnson, J. Lewis, M. Raff, K. Roberts, P. Walter, *Molecular Biology of the Cell* (Garland Science, New York, 2002).
10. A. Jilkine, A.F. Marée, L. Edelstein-Keshet, Bull. Math. Biol. **69**, 1943 (2007).
11. M. Otsuji, S. Ishihara, C. Co, K. Kaibuchi, A. Mochizuki, S. Kuroda, PLoS Comput. Biol. **3**, e108 (2007).
12. N.W. Goehring, S.W. Grill, Trends Cell Biol. **23**, 72 (2013).
13. P.K. Trong, E.M. Nicola, N.W. Goehring, K.V. Kumar, S.W. Grill, New J. Phys. **16**, 065009 (2014).
14. S. Alonso, M. Bär, Phys. Biol. **7**, 046012 (2010).
15. N.W. Goehring, P.K. Trong, J.S. Bois, D. Chowdhury, E.M. Nicola, A.A. Hyman, S.W. Grill, Science **334**, 1137 (2011).
16. F. Bergmann, L. Rapp, W. Zimmermann, Phys. Rev. E **98**, 020603(R) (2018).
17. M.J. Tindall, P.K. Maini, S.L. Porter, J.P. Armitage, Bull. Math. Biol. **70**, 1570 (2008).
18. T. Hillen, K.J. Painter, J. Math. Biol. **58**, 183 (2009).
19. M. Meyer, L. Schimansky-Geier, P. Romanczuk, Phys. Rev. E **89**, 022711 (2014).
20. B. Liebchen, D. Marenduzzo, I. Pagonabarraga, M.E. Cates, Phys. Rev. Lett. **115**, 258301 (2015).
21. I. Theurkauff, C. Cottin-Bizonne, J. Palacci, C. Ybert, L. Bocquet, Phys. Rev. Lett. **108**, 268303 (2012).
22. J. Palacci, S. Sacanna, A.P. Steinberg, D.J. Pine, P.M. Chaikin, Science **339**, 936 (2013).
23. I. Buttinoni, J. Bialké, F. Kümmel, H. Löwen, C. Bechinger, T. Speck, Phys. Rev. Lett. **110**, 238301 (2013).
24. Y. Fily, M.C. Marchetti, Phys. Rev. Lett. **108**, 235702 (2012).
25. J. Stenhammer, A. Tiribocchi, R.J. Allen, D. Marenduzzo, M.E. Cates, Phys. Rev. Lett. **111**, 145702 (2013).
26. G.S. Redner, M.F. Hagan, A. Baskaran, Phys. Rev. Lett. **110**, 055701 (2013).
27. T. Speck, J. Bialké, A.M. Menzel, H. Löwen, Phys. Rev. Lett. **112**, 218304 (2014).
28. Q.-X. Liu, A. Doelman, V. Rottschäfer, M. de Jager, P.M. Herman, M. Rietkerk, J. van de Koppel, Proc. Natl. Acad. Sci. U.S.A. **110**, 11905 (2013).
29. M.C. Cross, P.C. Hohenberg, Rev. Mod. Phys. **65**, 851 (1993).
30. T. Speck, A.M. Menzel, J. Bialke, H. Löwen, J. Chem. Phys. **142**, 224109 (2015).
31. R. Wittkowski, A. Tiribocchi, J. Stenhammar, R.J. Allen, D. Marenduzzo, M.E. Cates, Nat. Commun. **5**, 4351 (2014).
32. E. Tjhung, C. Nardini, M.E. Cates, Phys. Rev. X **8**, 031080 (2018).
33. J. Tailleur, M.E. Cates, Phys. Rev. Lett. **100**, 218103 (2008).
34. A.J. Bray, Adv. Phys. **43**, 357 (1994).
35. R.C. Desai, R. Kapral, *Dynamics of Self-Organized and Self-Assembled Structures* (Cambridge University Press, Cambridge, 2009).
36. A.P. Solon, J. Stenhammar, M.E. Cates, Y. Kafri, J. Tailleur, Phys. Rev. E **97**, 020602(R) (2018).
37. M.C. Cross, H. Greenside, *Pattern Formation and Dynamics in Nonequilibrium Systems* (Cambridge University Press, Cambridge, 2009).
38. J.W. Cahn, J.E. Hilliard, J. Chem. Phys. **28**, 258 (1958).
39. J.W. Cahn, Acta Metall. **9**, 795 (1961).
40. L.M. Pismen, *Patterns and Interfaces in Dissipative Dynamics* (Springer, Berlin, 2006).
41. E. Meron, *Nonlinear Physics of Ecosystems* (CRC Press, Boca Raton, Florida, 2015).
42. C. Misbah, *Complex Dynamics and Morphogenesis* (Springer, Berlin, Germany, 2016).
43. L. Edelstein-Keshet, W.R. Holmes, M. Zajac, M. Dutot, Philos. Trans. R. Soc. B **368**, 20130003 (2013).
44. L. Rapp, F. Bergmann, W. Zimmermann, EPL **113**, 28006 (2016).
45. F. Bergmann, L. Rapp, W. Zimmermann, New J. Phys. **20**, 072001 (2018).

Acknowledgements

Last but not least i want to thank several people that accompanied me during the time of my thesis:

- My supervisor Walter Zimmermann. For helpful discussions in an open and constructive atmosphere, for the possibility to present my work at several conferences and opportunity to contribute to the scientific world.
- My friend, colleague and bureau partner Lisa Rapp. For passionate discussions not only about physics, for delicious cakes and for encouraging each other after disappointing referee reports.
- The whole group of Theoretical Physics I. For creating a very pleasant and fun work environment and the readiness for a spontaneous after-work beer. Special thanks applys to Markus Hilt for his technical support and discussions about everyone and his dog.
- My future wife Lisa Gebhardt. For so much that i could write a second thesis about.
- My family and friends. For the confidence, fun and being there all the time.

Eidesstattliche Versicherung

Hiermit versichere ich an Eides statt, dass ich die vorliegende Arbeit selbstständig verfasst und keine anderen als die von mir angegebenen Quellen und Hilfsmittel verwendet habe.

Weiterhin erkläre ich, dass ich die Hilfe von gewerblichen Promotionsberatern bzw. -vermittlern oder ähnlichen Dienstleistern weder bisher in Anspruch genommen habe, noch künftig in Anspruch nehmen werde.

Zusätzlich erkläre ich hiermit, dass ich keinerlei frühere Promotionsversuche unternommen habe.

Bayreuth, den

Unterschrift